UNIWERSYTET KAZIMIERZA WIELKIEGO

WYDZIAŁ NAUK BIOLOGICZNYCH

KATEDRA BIOCHEMII I BIOLOGII KOMÓRKI

Doctoral Thesis

Functional consequences of disease-causing mutations in tropomyosin gene

Recep KÜÇÜKDOĞRU

Supervisor:

Prof. Joanna Moraczewska, Ph.D., D.Sc.

Bydgoszcz, 2026

Preface

This doctoral dissertation was completed within the Doctoral School in Biochemistry and Cell Biology at the Department of Biological Sciences, Kazimierz Wielki University in Bydgoszcz.

The research presented in this dissertation was conducted as part of projects funded by the National Science Centre (Narodowe Centrum Nauki, Poland):

- NZ5, “Preludium-22” (grant no.UMO-2023/49/N/NZ5/02175)

Additional support was provided through the Regional Initiative of Excellence (RID) project (No. 008/RID/2018/19,) at the Department of Biological Sciences, Kazimierz Wielki University in Bydgoszcz.

The doctoral candidate carried out this research at the Department of Biological Sciences, Kazimierz Wielki University in Bydgoszcz as a project researcher and scholarship recipient.

Declaration on the use of generative AI: During thesis preparation, I used ChatGPT (OpenAI) solely to improve language and readability. I reviewed all AI-assisted text and take full responsibility for the content of the thesis. These tools were not used to generate, analyze, manipulate, or interpret experimental data.

First and foremost, I would like to express my deepest gratitude to my supervisor, ***Prof. Joanna Moraczewska****, for her guidance, patience, encouragement, and continuous support throughout this work. I am especially grateful for her valuable scientific advice, critical discussions, and confidence in me during all stages of my doctoral studies and thesis preparation.*

I would also like to sincerely thank ***Dr Katarzyna Robaszkiewicz*** *and* ***Dr Małgorzata Siatkowska*** *for their support, scientific discussions, advice, and help during the experimental work. Their knowledge and willingness to share their experience greatly contributed to this thesis.*

I am grateful to our technicians, ***Marta Kaczmarek*** *and* ***Magdalena Fojutowska****, for their valuable assistance with protein preparation and other laboratory work.*

I would like to thank all my teachers and mentors who have contributed to my education and development as a scientist. Their guidance, knowledge, and encouragement have shaped the person and researcher I am today.

My sincere thanks go to my ***family*** *for their understanding, patience, and unwavering support throughout this long and demanding journey. Their belief in me gave me strength during challenging moments.*

Finally, I would like to thank my ***girlfriend*** *for her unwavering support, patience, and encouragement throughout the preparation of this thesis.*

Contents

Abstract

Tropomyosin (Tpm) is an actin-binding protein that plays central role in the regulation of the thin filament. Tpm extends along the filament and binds seven consecutive actin subunits through periodic repeats P1-P7. Together with the troponin (Tn) complex, Tpm controls actin-myosin interactions in the Ca^{2+}-dependent manner. In addition, Tpm influences thin filament stability and turnover, processes regulated by actin-binding proteins, including cofilin (Cof), which promotes actin-filament severing and depolymerization, and tropomodulin (Tmod), which caps the filament's pointed end and limits actin subunit exchange. Missense mutations in Tpm genes are associated with several congenital myopathies and distal arthrogryposes. The molecular mechanisms linking local structural changes in Tpm to altered thin filament regulation and disease phenotypes remain incompletely understood.

The aim of this thesis was to determine how two actin-binding periodic repeats of Tpm2.2, P1 and P5, which participate in interactions with actin and Tn and contribute to the regulation of myosin binding, affect functional communication among actin, myosin, Tn, Cof, and Tmod. To achieve this goal, four disease-associated pathogenic mutations in the *TPM2* gene, encoding the skeletal muscle Tpm isoform Tpm2.2 were selected: substitutions D20H and E181K, associated with hypercontractile phenotypes and located in the N-terminal halves of P1 and P5, and E41K and N202K, associated with hypocontractile phenotypes and located in the C-terminal halves of these periods. Thin filaments reconstituted from recombinant and muscle-isolated proteins were used in *in vitro* assays to examine the roles of the P1 and P5 regions in protein–protein interactions, actin polymerization, filament length and stability, and Cof2-dependent severing and depolymerization.

None of the pathogenic variants substantially altered the affinity of Tpm2.2 neither for F-actin alone nor with Tn, excluding loss of stable filament association as the disease mechanism. However, the hypercontractile variants changed orientation of Tpm2.2 on the filaments, which released inhibition of the actomyosin ATPase. In contrast, the hypocontractile variants orientation on the filament was not changed, so that they inhibited ATPase activity to the same extent as the wild type. The mutation-dependent phenotypes were also evident in the presence of Tn complex ($\pm Ca^{2+}$). The hypocontractile variants failed to fully activate ATPase activity while retaining their inhibitory capacity, whereas the hypercontractile Tpm2.2 variants produced excessive activation but exhibited reduced inhibition of actomyosin ATPase activity. Single-turnover experiments revealed no significant effects of mutations on ATP binding or

actomyosin dissociation and reassociation. However, opposite effects on product release were observed. Hypercontractile variants accelerated ADP release, whereas hypocontractile variants slowed it, providing a direct kinetic basis for the altered motor performance. In the *in vitro* motility assay, the hypercontractile variants increased myosin-driven actin translocation, whereas the hypocontractile variants reduced it, consistent with the hyper- and hypocontractile clinical phenotypes. These phenotypic differences were also reflected in Ca^{2+} sensitivity, which was increased by the hypercontractile variants and decreased by the hypocontractile variants. Independently of the phenotype, mutations in P1 enhanced the direct interaction between Tpm2.2 and Tn in the absence of actin, whereas mutations in P5 had no effect, indicating that changes in the affinity of Tn for Tpm2.2 did not determine the phenotypic differences between Tpm2.2 variants.

The mutations did not affect actin polymerization kinetics and the filament length at the steady-state. Analysis of filament length under mechanical load generated by ATP-driven actomyosin interactions showed that the mutations affected filament stability in a context-dependent manner. The presence of Tn strongly protected the filaments against Cof2-induced severing and depolymerization; however, the effects of the mutations again depended on their location within Tpm2.2 and on the presence of Tmod1. Because the mutations did not alter the affinity of either Cof2 or Tmod1 for actin, the observed effects on filament length and stability are likely to result from the interplay between multiple factors.

In conclusion, the primary function of actin-binding periodic repeats P1 and P5 is to regulate contraction by controlling actin–myosin interactions. The effects of pathogenic mutations within these repeats closely correlate with the hyper- and hypocontractile phenotypes observed in patients. These mutations also destabilize the filaments and alter their length, which may contribute to filament disarray and the formation of abnormal structures observed in patients' muscle cells.

Streszczenie

Tropomiozyna (Tpm) jest białkiem wiążącym aktynę, które odgrywa kluczową rolę w regulacji cienkiego filamentu. Tpm układa się wzdłuż filamentu i wiąże siedem kolejnych podjednostek aktyny za pośrednictwem powtarzalnych regionów P1–P7. Wraz z kompleksem troponiny (Tn) Tpm kontroluje, w sposób zależny od Ca^{2+}, interakcje aktyna–miozyna. Ponadto Tpm wpływa na stabilność i obrót cienkich filamentów, które są regulowane przez białka wiążące aktynę, w tym kofilinę (Cof), promującą przecinanie i depolimeryzację filamentów aktynowych, oraz tropomodulinę (Tmod), która czapeczkuje koniec zaostrzony filamentu i ogranicza wymianę podjednostek aktyny. Mutacje zmiany sensu w genach kodujących Tpm są związane z wrodzonymi chorobami mięśni–miopatiami oraz dystalnymi artrogrypozami. Molekularne mechanizmy łączące lokalne zmiany strukturalne w Tpm z zaburzoną regulacją cienkiego filamentu i fenotypami chorobowymi nie są w pełni poznane.

Celem niniejszej rozprawy było określenie, w jaki sposób dwa powtarzalne regiony P1 i P5 w Tpm2.2, które uczestniczą w oddziaływaniach z aktyną i Tn oraz biorą udział w regulacji wiązania miozyny, wpływają na funkcjonalną komunikację między aktyną, miozyną, Tn, Cof i Tmod. Aby osiągnąć ten cel, do badań wybrano cztery związane z chorobami mutacje w *TPM2*, genie kodującym izoformę Tpm2.2 charakterystyczną dla mięśni szkieletowych: podstawienia D20H i E181K, związane z fenotypami hiperkurczliwymi i zlokalizowane odpowiednio w N-końcowych rejonach P1 i P5, oraz E41K i N202K, związane z fenotypami hipokurczliwymi i zlokalizowane w C-końcowych rejonach tych powtórzeń. Cienkie filamenty rekonstytuowane z białek rekombinowanych oraz białek izolowanych z mięśni wykorzystano w badaniach *in vitro* do określenia roli regionów P1 i P5 w interakcjach białko–białko, polimeryzacji aktyny, długości i stabilności filamentów oraz w zależnym od Cof2 przecinaniu i depolimeryzacji filamentów.

Żaden z badanych wariantów nie zmieniał istotnie powinowactwa Tpm2.2 ani do F-aktyny, ani do Tn, co wyklucza utratę stabilnego związania z filamentem jako główny mechanizm chorobowy. Jednak warianty hiperkurczliwe zmieniały orientację Tpm2.2 na filamentach aktynowych, co osłabiało hamowanie aktywności ATPazowej aktomiozyny. Natomiast orientacja wariantów hipokurczliwych na filamentach nie ulegała zmianie, a ich wpływ hamujący na aktywność ATPazową był porównywalny z Tpm2.2 typu dzikiego. Fenotypy zależne od mutacji były również widoczne w obecności kompleksu Tn ($\pm Ca^{2+}$). Warianty hipokurczliwe nie były zdolne do pełnej aktywacji aktywności ATPazowej, zachowując jednocześnie zdolność do jej hamowania, podczas gdy hiperkurczliwe warianty

Tpm2.2 powodowały nadmierną aktywację, ale wykazywały zmniejszone hamowanie aktywności ATPazowej aktomiozyny. Eksperymenty w warunkach pojedynczego obrotu enzymatycznego nie wykazały istotnego wpływu mutacji na wiązanie ATP ani na dysocjację i reasocjację aktomiozyny, natomiast ujawniły przeciwstawne efekty dotyczące uwalniania produktów reakcji. Warianty hiperkurczliwe przyspieszały uwalnianie ADP, podczas gdy warianty hipokurczliwe spowalniały ten etap, dostarczając bezpośredniego kinetycznego wyjaśnienia zmienionej aktywności motorycznej miozyny. W teście ruchliwości *in vitro* warianty hiperkurczliwe zwiększały przemieszczanie filamentów aktynowych napędzane przez miozynę, natomiast warianty hipokurczliwe je zmniejszały, zgodnie z klinicznymi fenotypami hiper- i hipokurczliwości związanymi z tymi mutacjami. Różnice fenotypowe odzwierciedlała także wrażliwość na Ca^{2+}, która wzrastała w obecności wariantów hiperkurczliwych i malała w obecności wariantów hipokurczliwych. Niezależnie od fenotypu, mutacje w P1 wzmacniały bezpośrednią interakcję między Tpm2.2 i Tn pod nieobecności aktyny, podczas gdy mutacje w P5 nie wywoływały takiego efektu. Wyniki te wskazują, że zmiany powinowactwa Tn do Tpm2.2 nie determinowały różnic fenotypowych między badanymi wariantami Tpm2.2.

Mutacje nie wpływały na kinetykę polimeryzacji aktyny ani na długość filamentów w stanie stacjonarnym. Analizy długości filamentów w warunkach obciążenia mechanicznego indukowanego przez miozynę generowanego przez ATP-zależne interakcje aktomiozyny, wykazały, że mutacje wpływały na stabilność filamentów w sposób zależny od kontekstu. Obecność Tn silnie chroniła filamenty przed zależnym od Cof2 przecinaniem i depolimeryzacją. Również w tym przypadku, efekty mutacji zależały od ich położenia w Tpm2.2 oraz od obecności Tmod1. Ponieważ mutacje nie zmieniały powinowactwa ani Cof2, ani Tmod1 do aktyny, obserwowane efekty dotyczące długości i stabilności filamentów prawdopodobnie wynikały ze współdziałania wielu czynników.

Podsumowując, podstawową funkcją wiążących aktynę powtórzeń P1 i P5 jest regulacja skurczu poprzez kontrolę oddziaływań aktyna-miozyna. Efekty patogennych mutacji w obrębie tych powtórzeń ściśle korelują z obserwowanymi u pacjentów fenotypami hiper- i hipokurczliwości. Ponadto, mutacje destabilizują filamenty i zmieniają ich długość, przez co mogą przyczyniać się do dezorganizacji cienkich filamentów oraz powstawania nieprawidłowych struktur obserwowanych w komórkach mięśniowych pacjentów.

Abbreviations

Abbreviation	Definition
ADF	Actin-depolymerizing factor
ANOVA	Analysis of variance
ATP	Adenosine triphosphate
ATPase	Adenosine triphosphatase
BSA	Bovine serum albumin
Ca^{2+}	Calcium ion
Cof1	Cofilin-1
Cof2	Cofilin-2
DTT	Dithiothreitol
Ea	Activation energy
EC_{50}	Half-maximal effective concentration
EC_{50}^{act}	Tpm concentration producing 50% maximal activation of ATPase activity
EC_{50}^{inh}	Tpm concentration producing 50% maximal inhibition of ATPase activity
EGTA	Ethylene glycol-bis(β-aminoethyl ether)-N,N,N′,N′-tetraacetic acid
ELISA	Enzyme-linked immunosorbent assay
F-actin	Filamentous actin
FRET	Förster resonance energy transfer
G-actin	Globular (monomeric) actin
GST	Glutathione S-transferase
HEPES	2-[4-(2-Hydroxyethyl)piperazin-1-yl]ethane sulfonic acid
HMM	Heavy meromyosin
K_d	Equilibrium dissociation constant
k_{ass}	Apparent rate constant of actomyosin reassociation
k_{diss}	Apparent rate constant of actomyosin dissociation
k_{off}	Dissociation rate constant
k_{on}	Association rate constant
LS	Light scattering
mantATP	2′(3′)-O-(N-Methylanthraniloyl)adenosine 5′-triphosphate
mantADP	2′(3′)-O-(N-Methylanthraniloyl)adenosine 5′-diphosphate
MOPS	3-(N-Morpholino)propanesulfonic acid
MW	Molecular weight
P1–P7	Tropomyosin actin-binding periods 1–7
PBS	Phosphate-buffered saline
PBS-T	Phosphate-buffered saline containing 0.05% Tween 20
pCa	Negative logarithm of the free Ca^{2+} concentration
pCa_{50}	pCa at half-maximal activation; an index of Ca^{2+} sensitivity
PIA	N-(1-Pyrenyl)iodoacetamide
P_i	Inorganic phosphate
SDS	Sodium dodecyl sulfate
SDS–PAGE	Sodium dodecyl sulfate–polyacrylamide gel electrophoresis
SD	Standard deviation

SD1	Actin subdomain 1
SD2	Actin subdomain 2
SD3	Actin subdomain 3
SD4	Actin subdomain 4
SEM	Standard error of the mean
S1	Myosin subfragment 1
TBS	Tris-buffered saline
TLCK	Nα-p-Tosyl-L-lysine chloromethyl ketone hydrochloride
Tmod	Tropomodulin
Tmod1	Tropomodulin-1
Tn	Troponin complex
TnC	Troponin C
TnI	Troponin I
TnT	Troponin T
TPM1	Gene encoding tropomyosin isoform Tpm1.1
TPM2	Gene encoding tropomyosin isoform Tpm2.2
TPM3	Gene encoding tropomyosin isoform Tpm3.12
TPM4	Gene encoding tropomyosin isoform Tpm4.2
Tpm	Tropomyosin
Tpm1.1	Alpha-tropomyosin; fast skeletal/cardiac muscle tropomyosin isoform 1.1
Tpm2.2	Beta-tropomyosin; skeletal muscle tropomyosin isoform 2.2
Tpm3.12	Gamma-tropomyosin; slow skeletal muscle tropomyosin isoform 3.12
Tpm4.2	Tropomyosin isoform 4.2
TRC	Tetramethylrhodamine cadaverine
TRITC	Tetramethylrhodamine isothiocyanate
Trp	Tryptophan
WT	Wild type

1 Introduction

Contraction of striated muscle is fundamentally based on the shortening of the sarcomere, the basic functional unit of muscle fibers. This process is mediated by the cyclic interactions between thick and thin filaments. Thin filaments are primarily composed of filamentous actin (F-actin), along with regulatory proteins such as tropomyosin (Tpm) and the troponin (Tn) complex, which together control the accessibility of myosin-binding sites on actin. Thick filaments are formed by myosin molecules whose globular head domains project outward and interact with actin (A. F. Huxley, 1957; Gordon et al., 2000).

Tpm is an essential regulatory protein of the thin filament in both muscle and non-muscle cells. It is characterized by a coiled-coil, super helical dimeric structure that extends longitudinally along both sides of the actin filament, facilitated by end-to-end polymerization. In striated muscle, each Tpm molecule spans seven actin monomers and associates with one Tn complex, a protein that consists of three subunits: Ca^{2+}-binding troponin C (TnC), inhibitory troponin I (TnI), and Tpm-binding troponin T (TnT). Together, Tpm and Tn form a basic unit responsible for the regulation of muscle contraction. The control of actin–myosin interactions is mediated by Ca^{2+}-dependent conformational changes within this regulatory system (Ebashi & Endo, 1968; Gordon et al., 2000). Binding of calcium ions to Tn complex induces a positional shift of Tpm on the actin filament, thereby modulating accessibility of myosin-binding sites on actin. This mechanism constitutes the molecular basis of muscle contraction regulation in response to calcium transients in muscle cells stimulated by motor neuron (Vibert et al., 1997; Gordon et al., 2000; Bers, 2002).

Because Tpm is the core regulatory protein of the striated muscle thin filament, mutations in Tpm genes may disrupt the regulatory mechanism leading to dysfunction in actin–myosin interactions. Pathogenic variants can alter Tpm binding to actin, shift its position on the thin filament, or disrupt cooperative regulation with Tn, causing abnormal calcium sensitivity and defective force generation (Michele & Metzger, 2000; Stenson et al., 2017). In *TPM*-linked muscle diseases defects in structure of the thin filament are often observed (Moraczewska, 2020), placing Tpm as a regulator of thin filament integrity. Therefore, *in vitro* studies of disease-causing mutations are essential for understanding the molecular mechanisms underlying thin filament regulation. Such studies not only provide insight into structure–function relationships within the Tpm molecule, but also advance our understanding of the molecular basis of disease.

1.1 Structure of Skeletal Muscle Fibers

Muscle tissue is classified into three types: skeletal, cardiac, and smooth muscle. Skeletal muscle is attached to the skeleton and is under voluntary control, whereas cardiac muscle is found in the heart and contracts involuntarily to pump blood. Smooth muscle lines the walls of hollow organs and blood vessels and also functions involuntarily, helping regulate processes such as movement of food, blood flow, and organ tone. These three muscle types differ in structure and function: skeletal and cardiac muscle are striated, while smooth muscle is non-striated. Skeletal muscle fibers are long cells specialized for rapid and powerful contraction, cardiac muscle cells are branched and connected for coordinated rhythmic activity, and smooth muscle cells are spindle-shaped and adapted for sustained, slower contractions. Together, they enable movement, circulation, and the mechanical activity of internal organs (*Muscle Types | SEER Training*, n.d.).

Skeletal muscle is composed of parallel, multinucleated, elongated fibers filled with myofibrils, the contractile elements arranged along the long axis of the cell. The muscle is supported by three layers of connective tissue: the epimysium, which surrounds the entire muscle; the perimysium, which encloses bundles of fibers and contains blood vessels and nerves; and the endomysium, which surrounds individual muscle fibers and connects them to the surrounding membrane and extracellular matrix. The muscle cell is surrounded by the plasma membrane, also known as the sarcolemma, which forms invaginations that extend into the interior of the cell (see Figure 1.1).

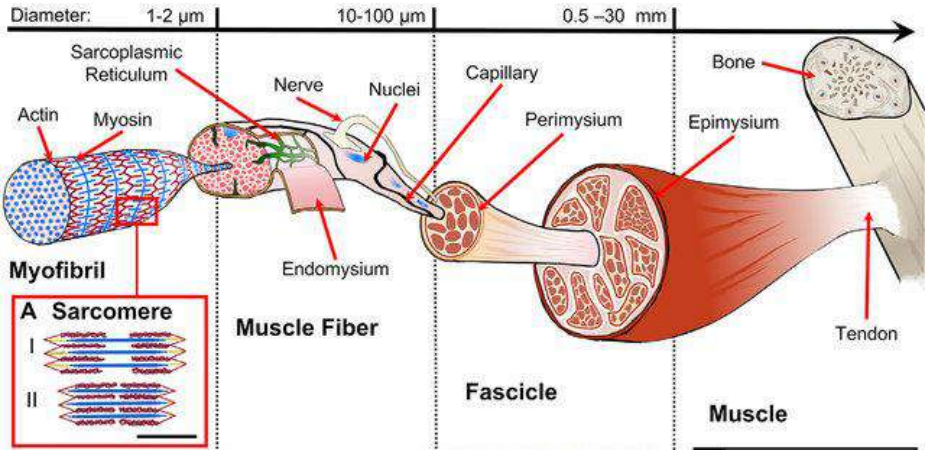

Figure 1.1 Schematic representation of muscle architecture, illustrating the hierarchical organization of muscle, muscle fibers, and myofibrils. Adapted from (Gotti et al., 2020) published under the CCA 4.0 International License.

These invaginations are tubular structures known as transverse tubules, or T-tubules. These membrane invaginations contain dihydropyridine receptors (DHPR) that make direct contacts with ryanodine receptors (RyR), Ca^{2+} release channels present in the membrane of the sarcoplasmic reticulum (SR). Muscle activation by motor neuron induces the DHPR leading to Ca^{2+} release from SR via RyR (MacIntosh, 2006; *Muscle Types | SEER Training*, n.d.).

Skeletal muscle exhibits a striated appearance resulting from the highly organized, repeating structural arrangement within the tissue. The striations are generated by numerous myofibrils (see Figure 1.1), each composed of repeating contractile units called sarcomeres. Each sarcomere has an average length of approximately 2.5 μm and represents the fundamental contractile unit (Paxton et al., 2003; Zhao et al., 2025). As contraction is driven by interactions between actin thin filaments and myosin heads, these interactions translate into contraction of the entire muscle. Therefore even small alterations in proteins responsible for contraction and the regulatory mechanisms affect the whole muscle performance. In the following paragraphs structure and function of the contractile machinery at the molecular level will be described in more details.

1.2 Structure of the Sarcomere

The generation of force and rapid movement in striated muscle depends on the highly coordinated process of sarcomere contraction. As shown on the electron micrograph of the sarcomere longitudinal section (Figure 1.2 A), it is a highly ordered molecular assembly comprising two parallel arrays of filaments: thin filament, which is primarily composed of α-actin and regulatory proteins, and thick filaments, consisting of myosin and associated proteins. The precise arrangement and interaction of these filaments underlie the contractile properties of muscle (A. F. Huxley, 1957). Morphologically, each sarcomere is delimited by two Z-disks, dense protein structures located at its lateral boundaries. The Z-disk bisects the I band, a lighter region that is shared between adjacent sarcomeres and contains only thin filaments. At the center of the sarcomere is the darker A band, which corresponds to the length of the thick filaments and includes a less dense central region known as the H zone. The H zone is traversed by the M line, a specialized structure that cross-links and stabilizes thick filaments within the sarcomere (see Figure 1.2 B). Thus, the Z-disk serves as the anchoring site for thin filaments, whereas the M band maintains the alignment and structural integrity of the thick filament lattice (A. F. Huxley, 1957).

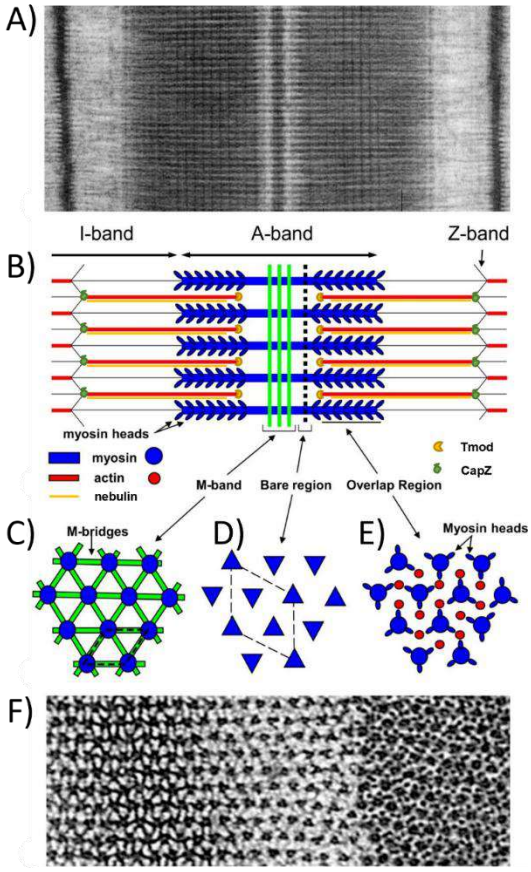

Figure 1.2 Structural organization of striated muscle sarcomere. (A) Electron micrograph of a frog sartorius muscle sarcomere and (B) schematic diagram of the sarcomere. (C-E) Schematic cross-sections at the M-band, bare region, and crossbridge region. (F) Corresponding electron micrographs of these three regions. In the bare region, myosin filaments show a triangular profile that reveals their rotational orientation. Adapted from (Millane & Luther, 2023) licensed under CC BY 4.0.

The thin filament is composed mainly of F-actin together with Tpm and Tn complex, which collectively regulate actin–myosin interaction in a calcium-dependent manner. The thick filament is formed primarily by myosin molecules, whose globular heads generate force through ATP-dependent cross-bridge cycle. Electron microscopy of the sarcomere cross-section revealed a regular hexagonal arrangement of the thick and thin filaments (Figure 1.2 C-F). A parallel order and precise length of the interacting filaments is crucial for synchronized contraction of sarcomeres.

1.2.1 Structure of the Thin Filament

The thin filament is a highly organized and functionally essential component of the sarcomere. The thin filament serves not only as the structural scaffold for force generation but also as the main regulatory platform controlling access of myosin to actin. Its architecture is based primarily on filamentous actin, which forms the backbone of the filament, together with the regulatory proteins like Tpm and the Tn complex (Bailey, 1946; Ebashi & Kodama, 1965).

These proteins act in a coordinated, calcium-dependent manner to control contraction and relaxation by modulating the exposure of myosin-binding sites on actin. The mechanism is described in more details in section 1.4.

Beyond its core actin–Tpm–Tn composition, the thin filament is stabilized by several accessory proteins that contribute to its precise assembly and maintenance. One of these proteins is nebulin, which extends along the thin filament and is widely regarded as a molecular ruler involved in determining and stabilizing thin filament length (K. Wang & Wright, 1988; Trinick, 1994, pp. 405–409; Marshall, 2004; Parry & Squire, 2017). One end of the filament is capped by CapZ, which anchors actin at the Z-disk and supports sarcomere assembly and structural integrity (Schafer et al., 1993, 1995; Yamashita et al., 2003). The opposite end is directed towards the center of the sarcomere and is capped with tropomodulin (Tmod) (Figure 1.2 B) (Weber et al., 1994; Coluccio, 1994; Gokhin & Fowler, 2011). Together, these proteins ensure that thin filaments remain precisely organized and properly sized, which is essential for efficient sarcomere function.

In this way, the thin filament should be viewed not as an isolated structure, but as part of an integrated sarcomeric network in which actin, Tpm, Tn, nebulin, CapZ, and Tmod collectively preserve the mechanical and regulatory properties required for normal muscle contraction.

1.2.1.1 Actin

Actin is a highly conserved globular protein (G-actin) that assembles into filamentous structures (F-actin) and is involved in a wide range of cellular functions, including cell movement, intracellular transport, and muscle contraction (Sheterline & Sparrow, 1994). Amino acid sequence of G-actin, a 375 a.a. (42-kDa) protein, is strongly conserved across species, and only minor interspecies differences are observed among actin paralogs. More pronounced differences occur between paralogs expressed in different tissues. In mammalian non-muscle cells, the cytoplasmic β- and γ-actin paralogs differ from the skeletal muscle α-actin by only 24 and 25 amino acid substitutions, respectively, most of which are conservative, out of a total of 374 amino acids for the β and γ and 375 amino acids for the α paralog. In striated muscle, the sarcomeric thin filament is built primarily from α-skeletal actin in skeletal muscle and α-cardiac actin in the heart. These two muscle-specific isoforms are highly similar, sharing approximately 99% sequence identity and differing at only four amino acid residues

out of 375 (Sheterline & Sparrow, 1994). This strong conservation reflects the essential structural and functional role of actin in contractile force generation.

G-actin is organized into two major domains, termed the inner and outer domains, which are separated by a nucleotide-binding cleft that accommodates both a nucleotide (ATP or ADP) and a divalent cation. In cells the divalent cation site is occupied by Mg^{2+}, but it is exchanged for Ca^{2+} during isolation and purification of G-actin from muscle. The domains are further divided into four subdomains (SD1–SD4), where SD1 and SD2 form outer domain and subdomains SD3 and SD4 fold into inner domain (Figure 1.3 A) (reviewed by Pollard, 2016).

Subdomains 1 and 2 are positioned in the outer domain of the actin filament (see Figure 1.3 B). The first structural model of F-actin was generated by fitting the crystal structure of G-actin into an electron density map of F-actin derived from X-ray diffraction of F-actin gels (Holmes et al., 1990). This model depicts the actin filament as a left-handed helix in which individual monomers are translated by 2.75 Å along the filament axis and rotated by 166° around the filament axis. Because the rotational angle is close to 180°, the filament appears as a right-handed double helix. The helical repeat occurs every 13 subunits (Kabsch & Vandekerckhove, 1992).

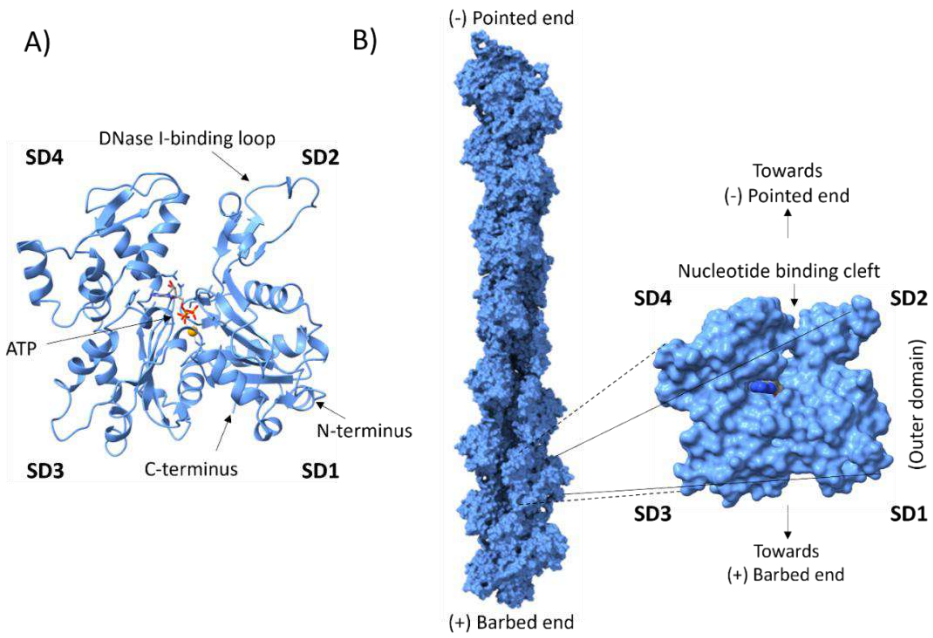

Figure 1.3 Structures of the G-actin molecule based on PDB: 1ATN. (A) Showing in ribbon diagram, numbers 1, 2, 3, and 4 label the four subdomains. (B) Space-filling model of F-actin showing (-) pointed end and (+) barbed end. (C) Structure of F-actin subunit based on PDB: 7UTI. Prepared using UCSF ChimeraX (Meng et al., 2023).

Within F-actin, individual actin monomers establish both longitudinal interactions with adjacent subunits along the same protofilament and lateral interactions with subunits in the neighboring protofilament. Consequently, each actin subunit interacts with three surrounding monomers, contributing to the stability and structural integrity of the filament. Structural studies of both G-actin and F-actin have provided important insights into the molecular basis of actin filament assembly, its interactions with myosin and numerous actin-binding proteins (Fujii et al., 2010; Murakami et al., 2010; Behrmann et al., 2012; Dominguez & Holmes, 2011; von der Ecken et al., 2015).

F-actin is a polar filament with two structurally distinct ends: the barbed end, also called the plus (+) end, and the pointed end, or minus (-) end (see Figure 1.3 B). The barbed and pointed ends were named after the appearance of the filament complex with myosin heads bound in rigor on electron microscopy images, which resemble an array of arrowheads. This polarity results from the uniform arrangement of actin monomers within the filament, with SD1/SD3 of each subunit oriented toward the barbed end and SD2/SD4 toward the pointed end (Holmes et al., 1990; Kabsch & Vandekerckhove, 1992).

Actin polarity is essential for its directional assembly and turnover of the filament with the plus end generally exhibiting faster subunit exchange and is the preferred site of filament elongation, whereas the pointed end is less dynamic (Dominguez & Holmes, 2011; Pollard, 2016). ATP-bound G-actin is the preferred form of actin monomer that is incorporated at both ends of the filament. On the filament, ATP is hydrolyzed to ADP-P_i followed by dissociation of P_i. Therefore, newly incorporated actin subunits are ATP-bound, whereas older subunits contain ADP-Pi or ADP, allowing actin-binding proteins (ABPs) to distinguish regions of the filament based on their "molecular age", as reflected by the nucleotide state. Because the association constant at the barbed (+) end is about 10-fold higher than at the pointed (-) end, at steady-state the elongation at the barbed end is compensated by depolymerization at the pointed end, a process referred to as treadmilling (reviewed by Pollard, 2016; Merino et al., 2020).

Nucleotide-dependent conformational changes occur primarily in the DNase I-binding loop (D-loop), located on top of SD2, and the C-terminal region at the intrastrain interface between adjacent actin subunits (Kabsch et al., 1990; Dominguez, 2019). ATP-bound filaments generally adopt a more open conformation, whereas ADP-Pi- and ADP-bound filaments exhibit a more closed structure (Figure 1.4). Because of the conformational rearrangements, the F-actin subunits become more flat than G-actin monomers (Oda et al., 2009; Fujii et al., 2010). In the

cytoskeleton, the ADP-bound state is less stable and is associated with increased depolymerization (Merino et al., 2020).

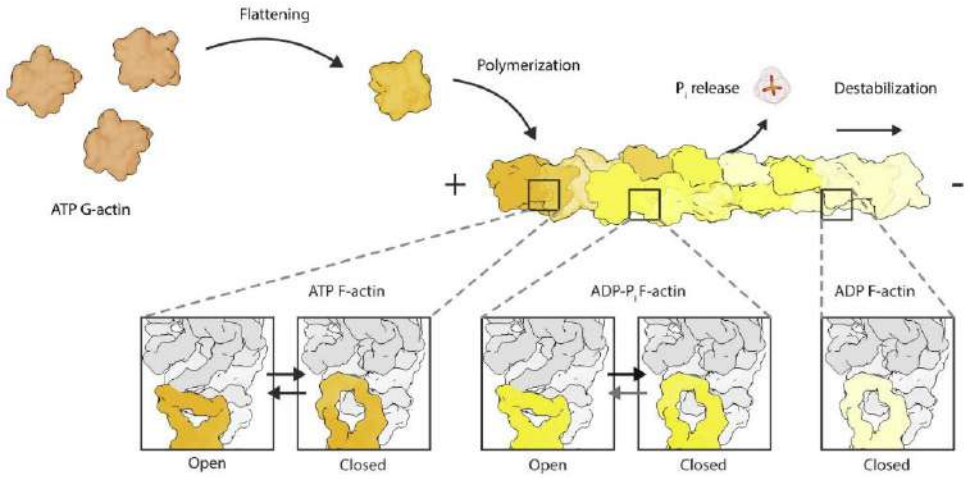

Figure 1.4 Conformational changes in the actin subunits associated with ATP hydrolysis on the actin filament. ATP-bound G-actin incorporates at the barbed (+) end and undergoes a conformational change upon polymerization into F-actin. A nucleotide state gradient along the filament reflects subunit age, which is communicated to the surface through the D-loop (yellow) of one subunit and the C-terminal tail of the adjacent subunit (gray). The closed D-loop conformation becomes increasingly prevalent with filament age and is locked in upon phosphate release. Adapted from (Merino et al., 2020), licensed under CC BY-NC-ND 4.0.

In contrast, actin filaments within mature muscle remain highly stable despite predominantly containing ADP-bound actin. This stability is maintained by thin filament-associated proteins, including nebulin, Tpm, Tmod, and CapZ, which protect the filament from turnover and disassembly (Z. Wang & Raunser, 2023). Therefore, in muscle the ATPase activity of actin acts as a molecular timer that regulates actin filament dynamics and is not directly linked to force generation during muscle contraction (Merino et al., 2018).

1.2.1.2 Tropomyosin

Tropomyosin is encoded by four genes: *TPM1* (encoding Tpm1 isoforms), *TPM2* (encoding Tpm2 isoforms), *TPM3* (encoding Tpm3 isoforms), and *TPM4* (encoding Tpm4 isoforms). In mammals, alternative splicing of mRNA exons from four genes encoding Tpm, as well as the use of alternative promoters, leads to the expression of about 40 different Tpm forms. Some of the isoforms are tissue-specific, whereas others are constitutively expressed. In different types of muscle fibers, products of the *TPM1*, *TPM2*, and *TPM3* genes are expressed in a muscle type-dependent manner (P. Gunning, 2008; Geeves et al., 2015).

Over the years of studies on various Tpm isoforms, diverse Tpm names were invented, which produced substantial inconsistency in the literature. To resolve this, Geeves, Hitchcock-

DeGregori and Gunning (2015) proposed a systematic nomenclature designating each isoform by its gene of origin and a sequential number. Under this system, the classical skeletal isoforms formerly designated by Greek letters are reclassified as Tpm1.1 (α-tropomyosin), Tpm2.2 (β-tropomyosin), and Tpm3.12 (γ- or slow tropomyosin), a scheme now adopted by NCBI RefSeq annotations for human, mouse, and rat (Geeves et al., 2015).

Skeletal muscle predominantly expresses three high-molecular-weight, striated-type paralogs, each generated from a distinct gene through tissue-specific splicing. Tpm1.1 arises from *TPM1* and is the principal isoform of fast-twitch fibers; Tpm2.2, from *TPM2*, is likewise enriched in fast and slow muscles; and Tpm3.12, from *TPM3*, is the dominant isoform in slow-twitch fibers (Pieples & Wieczorek, 2000; Corbett et al., 2005; Geeves et al., 2015; Lambert & Gussoni, 2023). A top-down proteomic survey of human, swine, and rat muscles confirmed Tpm1.1 and Tpm2.2 as dominant isoforms across species, while Tpm3.12 was detected specifically in human muscle, illustrating species-specific complexity in Tpm expression (Jin et al., 2016).

Expression of cardiac and skeletal muscle *TPM1* and *TPM2* is developmentally regulated. Tpm2.2 is the major Tpm isoform present in skeletal muscle at early stages of human embryonic development (Laurent-Winter et al., 1991; Zhu et al., 2017). The essential role for *TPM2* during muscle development was demonstrated in *TPM2*-deficient mice, in which severe skeletal muscle abnormalities were observed (McAdow et al., 2022).

The amino acid sequence of Tpm paralogs is determined by gene-specific variations rather than alternative exon splicing. Therefore, Tpm1.1 and Tpm3.12 differ by only 21 amino acid substitutions, whereas Tpm1.1 and Tpm2.2 exhibit approximately 40 substitutions (Matyushenko et al., 2018; Kopylova et al., 2020; Moraczewska, 2020).

Tpm is a dimeric coiled-coil protein that exists either as a homodimer, composed of two identical chains, or as a heterodimer formed by two distinct paralogs. Three principal muscle paralogs give rise to six possible dimeric combinations: the homodimers Tpm1.1/Tpm1.1, Tpm2.2/Tpm2.2, Tpm3.12/Tpm3.12 and the heterodimers Tpm1.1/Tpm2.2, Tpm1.1/Tpm3.12, and Tpm3.12/Tpm2.2. In mature organisms, four species (Tpm1.1/Tpm1.1, Tpm3.12/Tpm3.12, Tpm1.1/Tpm2.2, and Tpm3.12/Tpm2.2) are dominant in muscle tissue (Lehrer et al., 2011; Janco et al., 2013; Gregorich et al., 2014; Jin et al., 2016).

In terms of overall architecture, Tpm isoforms share a highly conserved structural organization. Each Tpm molecule forms a coiled-coil superhelix composed of two α-helical polypeptide chains intertwined along their entire length (Hitchcock-DeGregori et al., 2002). The coiled coil is approximately 400 Å in length and 20 Å in width. Its sequence is characterized by a heptad repeat pattern (*a, b, c, d, e, f, g*), in which positions *a* and *d* are predominantly hydrophobic. These residues from one α-helix interact with the corresponding residues of the second α-helix, forming the hydrophobic core of the molecule (Figure 1.5 A, B) (Stewart, 2001; Kirwan & Hodges, 2010). This interaction has been described by Crick as a "*knobs-in-holes*" packing arrangement, in which the spatial complementarity of residues creates a structurally stable interface between the two helices (Brown et al., 2001). Additional structural stability is provided by electrostatic interactions among oppositely charged residues exposed on the surface of the helix, particularly at positions *e* and *g* (Figure 1.5 A).

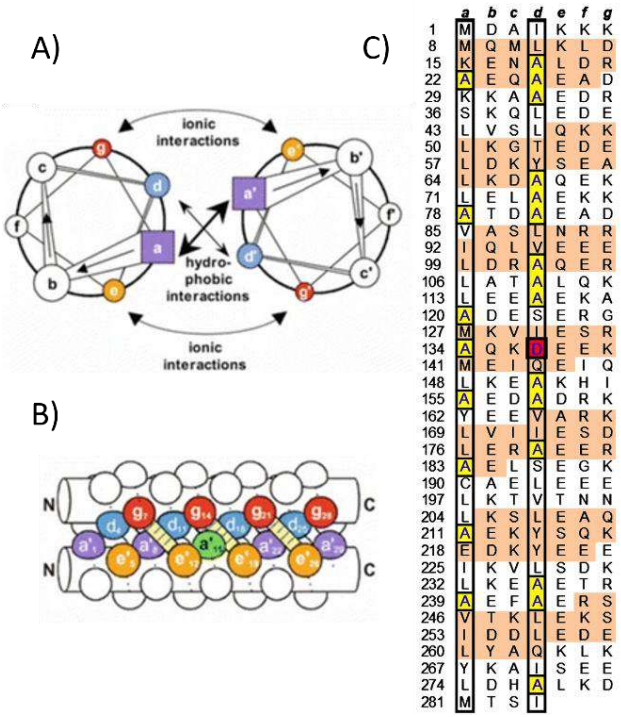

Figure 1.5 Schematic illustration of amino acid positions in two-stranded coiled coil structure of Tpm. (A) Helical wheel representation viewed from the C-terminus. (B) Side view of the α-helical backbones. Residues in the heptad repeat (*a*–*g*) are labelled, with positions *a* and *d* forming the hydrophobic core and positions *e* and *g* contributing to interhelical electrostatic interactions through salt-bridge formation. (C) Sequence of Tpm1.1 divided into heptapeptide repeats. Residues occupying the a and d positions of the heptad repeat form the hydrophobic stripe of the coiled coil (outlined by vertical boxes). The α-zones of each pseudo-repeat, which are positioned in proximity to actin subdomains 1 and 3, are distinguished by tan shading, whereas the 2nd halves, located over actin subdomains 2 and 4, are indicated by a white background. Alanine clusters at the *a* and *d* positions, together with the non-canonical D137, are highlighted in yellow and red, respectively. The figure is adapted from (Hitchcock-DeGregori & Barua, 2017; Lehman et al., 2020).

Tpm molecules polymerize into linear chains in such a way that the C- and N-terminal fragments of adjacent molecules overlap, forming a type of junction. The structure of this junction was first determined by NMR for rat muscle α-tropomyosin (Tpm1.1) (Greenfield et al., 2006). This structure showed that the C-terminal chains split to form a kind of pocket into which the N-terminal chains of the next Tpm molecule enter. A similar structure was obtained for rat non-muscle Tpm; the difference concerned only the number of amino acid residues involved in forming the junction. In skeletal or smooth muscle, the correct structure of the junction region also depends on N-terminal methionine acetylation. The absence of the acetyl group destabilizes the N-terminus of the superhelix and reduces Tpm affinity for actin. The main role of acetylation is probably to facilitate binding of the ends of Tpm molecules (Greenfield et al., 2009; P. W. Gunning et al., 2015; Hitchcock-DeGregori & Barua, 2017).

Early crystallographic studies suggested that the contact sites between Tpm and actin are periodically repeated along the Tpm sequence (Phillips, 1986). The length of the Tpm molecule allows it to interact with seven actin subunits. This forms the basis for dividing the Tpm molecule into seven binding periods (P1-P7). These periods can be further divided into α and β zones corresponding to the 1st and 2nd half of each actin-binding period (Figure 1.6).

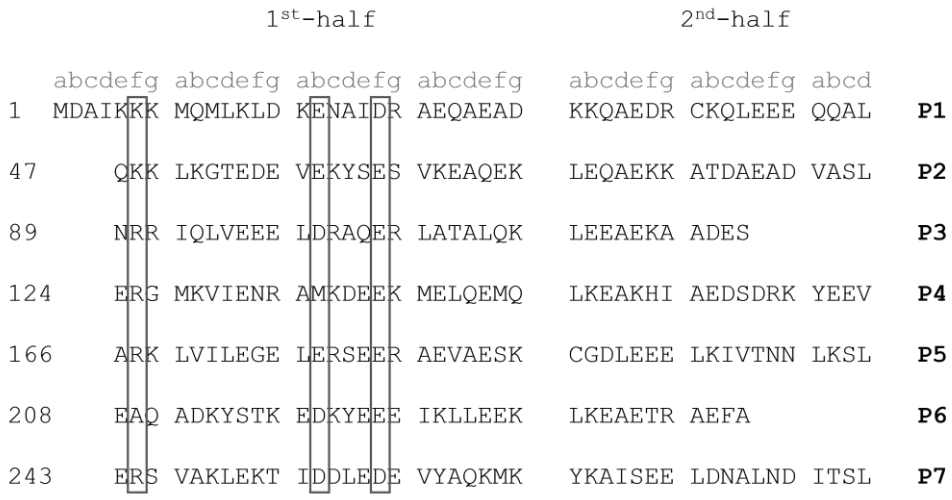

Figure 1.6 Distribution of the seven semi-conserved periodic repeats (P1–P7) along the N-terminal and C-terminal halves of the Tpm2.2 sequence (NP_003280.2). The letters above the sequence indicate the positions of the coiled-coil heptad repeat (a–g). Consensus sites are outlined by vertical boxes. The heptad register and consensus sites for the Tpm2.2 sequence are based on the assignment reported by (Barua, 2013).

When bound to actin filament, Tpm makes direct contacts with actin subunits through ionic interactions between negatively charged amino acids occupying positions *b*, *c*, and *f*, facing outward Tpm coiled coil so that they can form ionic interactions with Lys326 and Lys328 on successive actin subunits along the thin filament (Figure 1.7) (X. Li et al., 2011; von der

Ecken et al., 2015; Lehman, 2026). The sites of Tpm direct interactions with actin are evolutionarily conserved and are called consensus sites (Phillips, 1986; Barua et al., 2011).

The structural work showed that Tpm does not bind as a rigid rod, but instead adopts a bent superhelical conformation that closely follows the long-pitch helix of F-actin (Brown et al., 2005). More recent cryo-EM studies have significantly refined this view and have provided more advanced atomic models of F-actin–Tpm complex. Tpm is positioned asymmetrically on the actin filament, with specific residues from actin subdomains 1 and 3 contributing to the binding interface. Tpm binds along the long-pitch helix of F-actin as a continuous coiled-coil cable, making extensive contacts with seven actin subunits. Electrostatic interactions between the negatively charged surface of Tpm and a positively charged groove on F-actin mediate Tpm binding along the actin filament (see Figure 1.7) (von der Ecken et al., 2015).

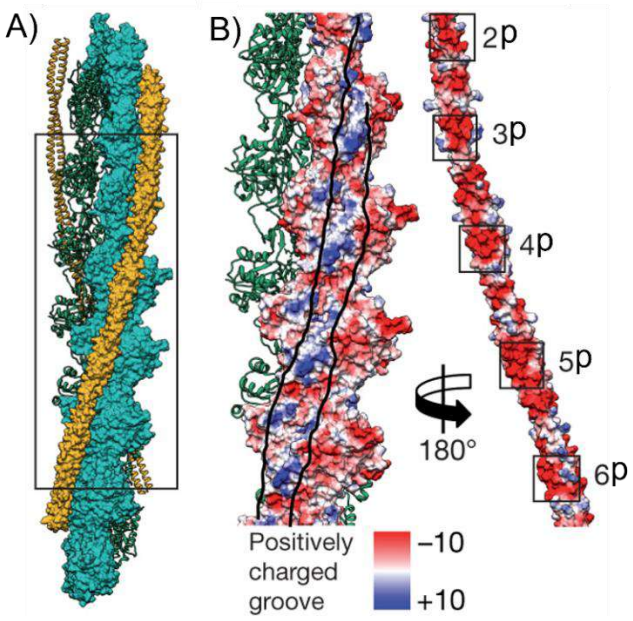

Figure 1.7 Structural overview of the F-actin–Tpm complex. (A) F-actin subunits are shown in green and cyan, with Tpm shown in yellow. (B) One half of the filament is displayed as a surface representation. The electrostatic surface potentials of F-actin and Tpm (pseudo-repeats 2–6) are shown, ranging from −10 to +10 kcal mol^{-1} at pH 7.5. For clarity, Tpm has been rotated by 180° and shifted to the right to better visualize the F-actin–Tpm interface, which is outlined on the molecular surfaces. Adapted from (von der Ecken et al., 2015) with the permission from *Springer Nature.*

1.2.1.3 Troponin Complex

As mentioned above, the thin filament of striated muscle contains the Tn complex, which is composed of three subunits: TnC, TnI, and TnT (Figure 1.8). Within the Tn complex, TnT is the largest subunit of the complex, which binds Tpm and anchors the entire Tn complex to the thin filament. Electron microscopy studies have shown that TnT adopts an elongated,

rod-like conformation and that two functional Tpm-binding regions, originally termed T1 and T2, can be distinguished within this subunit. The T1 region interacts with the C-terminus of Tpm and with the Tpm overlap region, whereas the T2 region binds central region of Tpm, TnI, and TnC to form the globular core domain of troponin (Vinogradova et al., 2005). Structural studies have demonstrated that this core adopts a W-shaped architecture formed by helices from TnI and TnT, with the central portions of these subunits assembling into a TnT–TnI coiled-coil structure called "IT arm" that serves to support and position TnC on the thin filament (Vinogradova et al., 2005; Yang et al., 2014; Yamada et al., 2020; Tobacman, 2021).

TnC occupies a central position in Ca^{2+}-dependent regulation because it is the Ca^{2+}-binding subunit of the complex. TnC can bind calcium through EF-hand motifs, which are grouped into two rounded domains linked by one long central α-helix. This arrangement makes TnC look like an elongated, dumbbell-shaped molecule (reviewed by Aborode et al., 2024). In the absence of Ca^{2+}, the N-terminal regulatory domain of TnC remains in a closed conformation, whereas Ca^{2+} binding to this domain induces a transition to the open state, exposing a hydrophobic pocket that accommodates the TnI switch peptide and thereby initiates regulatory rearrangements within the complex (see Figure 1.8) (Vinogradova et al., 2005).

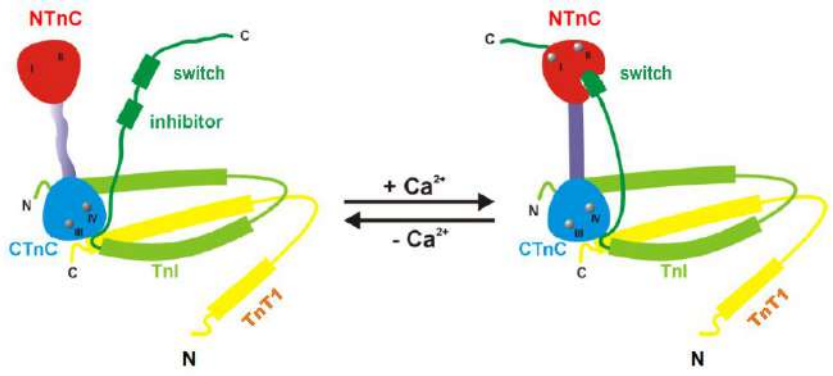

Figure 1.8 Illustration of calcium–dependent interactions between TnC and segments of TnI and TnT. Transition of the N-terminal domain of TnC into the open state leads to binding of the TnI switch segment, which restores the helical structure of the TnC linker and, in turn, results in extension of the inhibitory region of TnI. Adapted from (Moraczewska et al., 2012) published under the CC BY-SA 4.0 international License.

Cryo-EM structures revealed details of cardiac Tn interactions with actin and Tpm. This work confirmed that Tn is not a compact switch but an elongated regulatory assembly, with the TnI C-terminal region extending along Tpm and interacting with actin in the Ca^{2+}-free state. The N-terminal region of TnT extends toward the Tpm head-to-tail junction of the opposite strand (Figure 1.9), (Yamada et al., 2020; Risi et al., 2021, 2025).

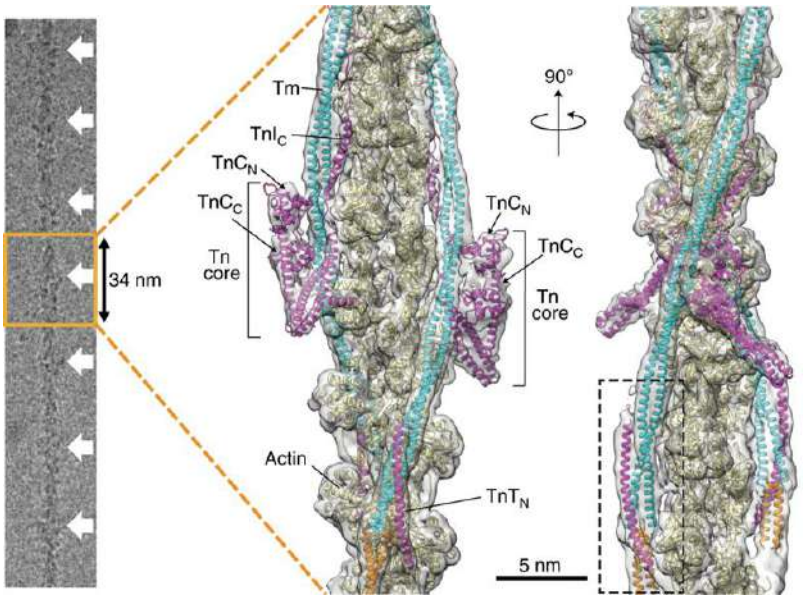

Figure 1.9 Representative cryo-EM image showing periodic troponin binding on the actin thin filament (the left image) and fitted model shown in two views, containing approximately 12 actin subunits, two Tpm coiled coils, and two Tn ternary complexes positioned along Tpm. Dashed box shows Tpms junction region with TnT. Adapted from (Yamada et al., 2020) published under the CC BY 4.0 international License.

1.2.2 Structure of the Thick Filament

Thick filaments are bipolar, spindle-shaped polymers assembled from myosin II molecules and non-myosin proteins, including titin and myosin-binding protein C (MyBP-C) (Craig & Woodhead, 2006). Myosin II is the principal force-generating motor protein of striated and smooth muscle, and is distinct from the broader myosin superfamily by its ability to self-assemble into bipolar filaments (Warrick & Spudich, 1987). In thick filaments, the elongated α-helical tails of myosin molecules assemble to form the filament backbone, whereas the myosin heads project outward from the surface. These filaments have an antiparallel tail interactions at the central region and parallel interactions along each half. The central region forms a bare zone, where filament polarity reverses and myosin heads are absent (Figure 1.10 A) (reviewed by Craig et al., 2026). Titin is mainly associated with sarcomere elasticity, but it also contributes to the overall organization of the contractile apparatus by spanning from the Z-disk toward the M-line and helping to maintain the alignment and structural coordination of sarcomeric components (Parry & Squire, 2017). MyBP-C is an important regulator of thick-filament behavior and muscle contraction. By localizing to the C-zone of the thick filament, MyBP-C helps organize myosin heads and influences their availability for interaction with actin. In cardiac muscle, MyBP-C modulates the strength and timing of contraction by affecting cross-bridge formation and contractile activation (Craig et al., 2026).

The myosin II molecule is a hexamer consisting of two identical heavy chains and two pairs of light chains – regulatory and essential light chain (Figure 1.10 B) (Warrick & Spudich, 1987). In the C-terminal region, the two heavy chains wind around each other to form a left-handed coiled-coil superhelix known as the rod. Moving toward the N-terminal end, the rod bifurcates into two short neck segments, each folding into a globular motor domain known as the myosin head. Non-covalent interactions in the neck anchor four light chains: one essential light chain (ELC) and one regulatory light chain (RLC) per head, with the RLC positioned at the distal neck at its junction with the rod (Knight & Trinick, 1984).

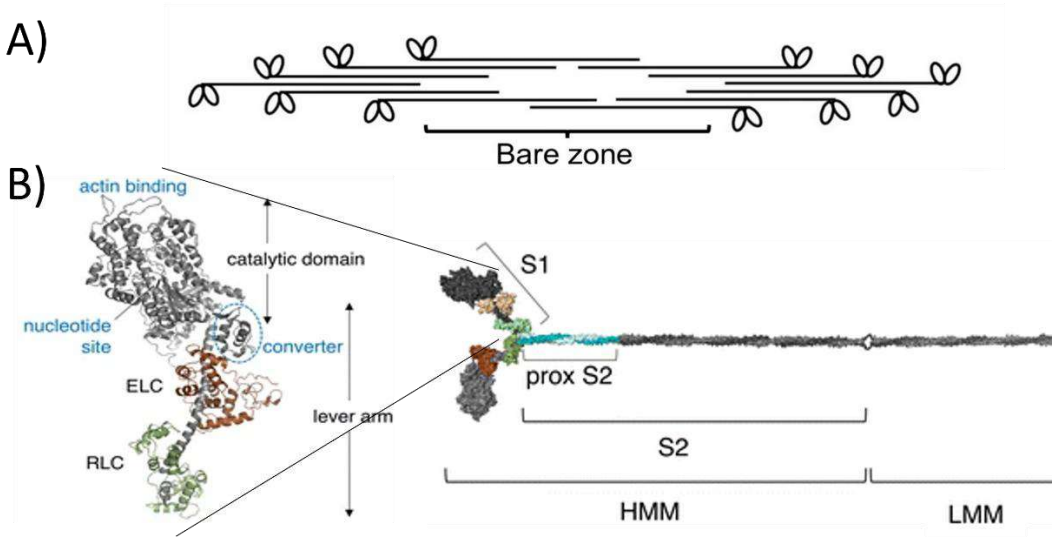

Figure 1.10 Structural organization of skeletal thick filament. (A) schematic illustration of the thick filament, adapted from (Craig et al., 2026). (B) Model of full-length human β-cardiac myosin II. Full-length myosin II showing the major domains: subfragment 1 (S1), proximal S2 (prox S2), subfragment 2 (S2), heavy meromyosin (HMM), and light meromyosin (LMM). Ribbon structure shows the S1 head in the pre-stroke state with key structural domains indicated. ELC, essential light chain; RLC, regulatory light chain. Adapted from (Trivedi et al., 2018) published under the CC BY 4.0 international License.

The distinct functional domains of myosin II were first characterized by controlled proteolytic digestion. Cleavage near the midpoint of the rod divides the molecule into light meromyosin (LMM), which is almost entirely α-helical and retains the ability to aggregate at low ionic strength, and heavy meromyosin (HMM), comprising both heads connected by subfragment 2 (S2). Under more stringent conditions, the heads, subfragment 1 (S1), can be released from S2. Both S1 and HMM retain ATPase activity and the capacity to bind actin, whereas LMM retains only the ability to self-assemble into filaments (Offer & Knight, 1996). The junction between S2 and LMM contains local helical irregularities that create a flexible hinge, enabling S2 together with the motor domains to swing outward from the filament backbone which is essential for productive cross-bridge cycling (Atkinson & Stewart, 1992). Within the motor domain, a prominent cleft separates two subdomains, upper (U50) and lower

(L50), with actin-binding sites near the cleft mouth and the nucleotide-binding pocket on the opposing face of the head (Figure 1.10 B) (Rayment et al., 1993; Rassier & Månsson, 2025).

1.3 Molecular Mechanism of Contraction

Muscle contraction is associated with the cyclic attachment and detachment of myosin heads from actin, a process intimately correlated with ATP hydrolysis occurring within the catalytic pocket of the myosin head. Based on observations of cross-bridges in the electron microscope and kinetic studies of ATP hydrolysis by myosin, a mechanism of force and movement generation in the muscle cell was first proposed by Hugh Huxley (H. E. Huxley, 1969) and independently by Andrew Huxley (A. F. Huxley, 1957). Subsequently the mechanism was elaborated through biochemical and structural analyses (H. E. Huxley, 1969; H. E. Huxley & Kress, 1985; Geeves & Holmes, 1999; Spudich, 2001; Zeng et al., 2004).

Cross-bridge cycle involves cyclic conformational changes of the myosin head occurring in conjunction with successive steps of nucleotide hydrolysis (Figure 1.11). ATP binding by the myosin head induces detachment from the actin filament, yielding the post-rigor state. Subsequent hydrolysis of ATP to ADP and P_i is accompanied by a change in the angle of the head relative to the long axis of the thick filament and a substantial increase in affinity for actin, producing the pre-power stroke state. This primed configuration permits re-attachment of the head to actin, forming a weak actomyosin complex. Actin binding activates release of hydrolysis products, first P_i, then ADP leading to a return of the actin-bound head to its original angular position; this mechanical transition displaces the actin filament and generates force in what is termed the power stroke. Following product release, the filaments are tightly coupled in the nucleotide-free rigor state. Binding of ATP to myosin head allows the actomyosin to enter the next cycle (Galler et al., 2005; Geeves & Holmes, 2005; Park et al., 2024).

The structural basis for the transmission of conformational changes within myosin head to filament displacement is provided by the lever arm mechanism, supported by the crystal structure of the myosin S1 motor domain. Relatively small rearrangements within the motor domain produce large angular changes in a rigid α-helical segment of the C-terminal myosin heavy chain, the lever arm, amplifying small motions into a substantial displacement relative to the actin filament (see the myosin S1 illustrated in the center of Figure 1.11) (Houdusse & Sweeney, 2016; Rassier & Månsson, 2025).

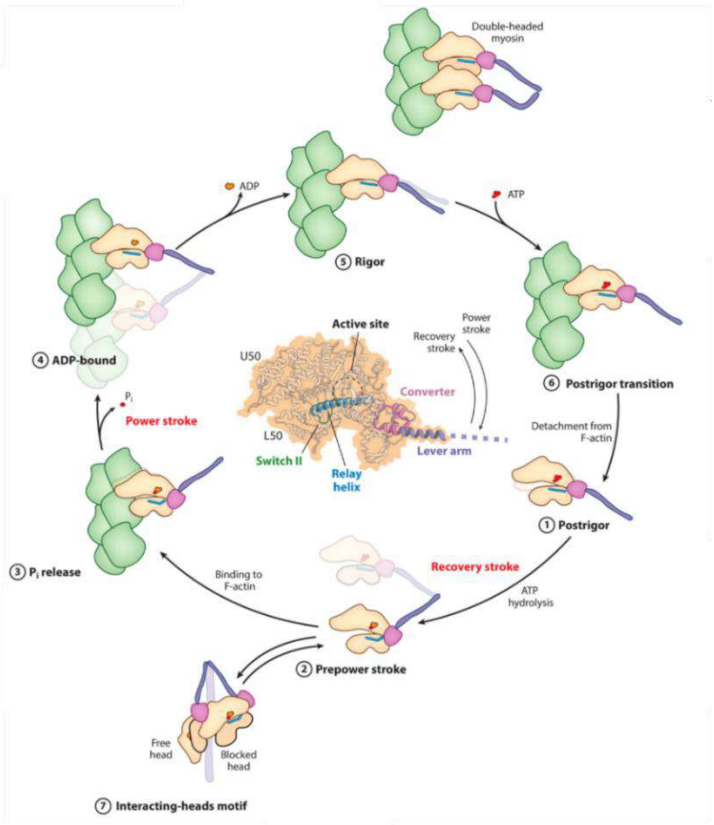

Figure 1.11 Cyclic actin–myosin interactions during muscle contraction. Schematic view of the myosin motor domain bound to F-actin showing key structural elements that undergo conformational changes during the ATP-driven cross-bridge cycle, including switch II, the relay helix, the converter domain, and the lever arm. Surrounding panels illustrate successive biochemical states (ATP binding, hydrolysis, and product release), the associated conformational changes in myosin and transitions in myosin–actin interactions. Reproduced from (Z. Wang & Raunser, 2023) published under the CC BY 4.0 international License.

1.4 Regulation of Actin-Myosin Interactions by Tpm-Tn complex

Tpm changes its azimuthal position on the filament in response to Ca^{2+} binding to Tn and to attachment of myosin heads. Through these positional changes, the Tpm-Tn complex regulates the transition of the thin filament between inactive 'off' and active 'on' states, thereby controlling actin-myosin interactions during contraction (reviewed by Lehman, 2026).

The classical three-state model (McKillop & Geeves, 1993) describes thin filament regulation through the blocked state, closed state, and myosin-induced open state, commonly referred to as the B-state, C-state, and M-state (see Figure 1.12). In the B-state, which predominates at low Ca^{2+} concentration, Tpm occupies a position that sterically blocks strong myosin binding to actin. This inhibited state is stabilized by TnI and TnT interactions with actin and Tpm. When Ca^{2+} binds to the N-terminal regulatory domain of TnC, conformational changes within the Tn complex weaken the inhibitory interaction of TnI with actin-Tpm (Figure 1.9). This allows Tpm to move toward the C-state, where myosin-binding sites on actin are

partially exposed. In this state, weak myosin binding becomes possible, but full activation requires further displacement of Tpm. The M-state is promoted by the binding of strongly attached myosin heads to actin. In this state, Tpm is shifted further away from the myosin-binding interface, allowing strong actin-myosin interactions and force generation. Thus, Ca^{2+} binding initiates thin filament activation by shifting the equilibrium from the B-state toward the C-state, whereas myosin binding stabilizes the M-state. This mechanism explains why thin filament activation is cooperative: the binding of one myosin head can promote further Tpm movement and increase the probability of neighboring myosin-binding events (McKillop & Geeves, 1993; Vibert et al., 1997; Lehman et al., 2020; Rynkiewicz et al., 2022; Z. Wang & Raunser, 2023).

Analyses of structural changes in Tpm during the transition from the blocked to the open state reveal a rotation accompanied by a translocation of approximately 23 Å, consistent with an azimuthal rotation of 31.5° (Lehman, 2017). Other studies identified conserved residues in the 2nd half of Tpm that form specific electrostatic contacts with actin (Lys328, Glu226, Asp311) and myosin (Asp312, Lys295, Lys300). The weakness along with specificity of these electrostatic interactions allows for the dynamic, reversible regulation of thin filament state that is essential for normal contractile cycling (Barua et al., 2012).

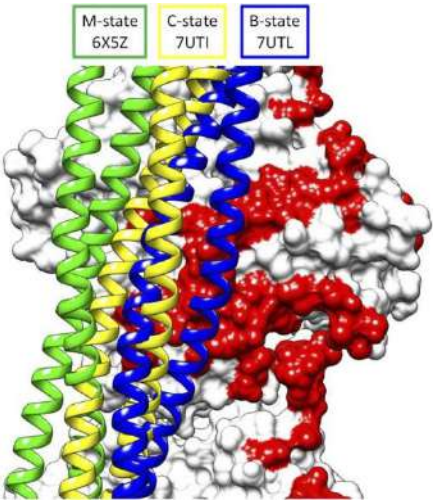

Figure 1.12 Movement of Tpm over actin (white surface, pointed end up) during thin filament activation showing the three structural states of Tpm; the M-state (green), C-state (yellow), and B-state (blue). As Tpm moves from B- to M-state the myosin binding site (red) on actin are relived. Adapted from (Rynkiewicz et al., 2022) published under the CC BY 4.0 international License.

The cooperative nature of Tpm switching between the states means that the activation state of one regulatory unit influences its neighbors, generating the sigmoidal Ca^{2+}-dependence of force characteristic of striated muscle and ensuring that the thin filament behaves as an

allosteric ensemble rather than as a collection of independent switches (Moraczewska, 2002; Moore et al., 2016).

An atomic model of the F-actin–Tpm–myosin complex in the M-state of the filament was constructed by fitting high-resolution structures of skeletal Tpm1.1, F-actin, and the *Dictyostelium discoideum* myosin motor domain into electron microscopy reconstructions (Behrmann et al., 2012). This model demonstrates that when bound in rigor state, the myosin motor domain interacts simultaneously with two adjacent actin monomers, forming an extensive contact surface, and identifies Tpm residues involved in contacts with both actin and myosin.

The transition of Tpm from the C-state to the fully activated M-state is influenced directly by structural elements on the myosin head that participate in actin binding. In particular, Loop-4, located near the tip of the myosin head, approaches Tpm on the thin filament and is positioned to promote Tpm displacement during activation (Figure 1.13). Within this loop, the charged side chain of Arg369 and Glu370 extend toward positively charged residues on Tpm, suggesting that electrostatic repulsion may help drive Tpm across the actin surface toward the M-state (Doran et al., 2020, 2023; Rynkiewicz et al., 2024). The functional importance of these Loop-4 residues is supported by their conservation among muscle myosin and by mutation studies showing that changes in Arg369 or Glu370 impair a complete M-state movement of Tpm (Doran et al., 2023; Lehman, 2026).

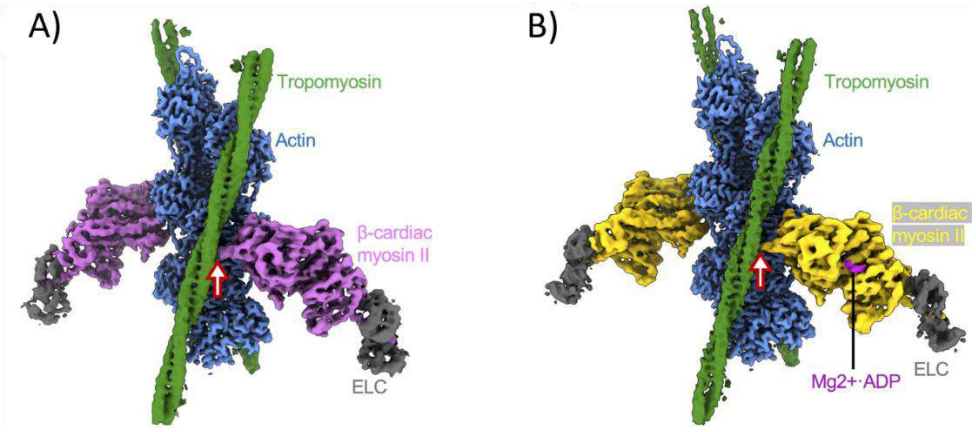

Figure 1.13 Composite cryo-EM reconstructions of the human cardiac actin–β-myosin–Tpm complex. (A) Rigor actin–β-cardiac myosin II–Tpm complex. (B) Mg^{2+}ADP-bound complex, showing myosin-induced displacement of Tpm on actin. Arrows indicate possible interactions between myosin and Tpm. Adapted from (Doran et al., 2023) with permission from *Rockefeller University Press*.

1.5 Regulation of Thin Filament Length and Stability

Thin filament length varies between muscle types and fiber populations and is adjusted according to the functional demands of each muscle. This regulation contributes to differences in sarcomere architecture and contractile properties. Therefore, precise control of thin filament length is essential for maintaining sarcomere organization, proper actin-myosin overlap, and efficient force generation. Thin filament length is controlled by a balance between actin polymerization, stabilization, capping, severing, and depolymerization. Several actin-binding proteins contribute to this process, including Tpm, tropomodulin (Tmod), capping protein (CapZ), nebulin-related proteins, and members of the actin-depolymerizing factor/cofilin (ADF/cofilin) family (Littlefield & Fowler, 2008; Szikora et al., 2022).

Thin filaments are capped at both ends. The barbed end is capped by the capping protein complex, CapZ, whereas the pointed end is capped by Tmod (Figure 1.14). Tmod (Tmod1–Tmod4 in vertebrates) plays an important role at the pointed end of the thin filament, where it caps actin and limits the exchange of actin subunits. Its affinity for actin is increased by Tpm, suggesting that Tpm not only stabilizes the filament along its length but also contributes to pointed-end regulation. During capping, Tmod binds to two Tpm molecules and at least one actin molecule (Colpan et al., 2013). The strength of this interaction depends on the specific Tmod and Tpm isoforms involved (Yamashiro et al., 2014). These binding affinities affect the correct localization of Tmod and its ability to cap the pointed ends of actin filaments in cells (Rao et al., 2014; Fowler & Dominguez, 2017; Szikora et al., 2022). Although in muscle Tn forms a tight complex with Tpm, it is not known whether Tn and Ca^{2+} affect capping the pointed end by Tmod and the thin filament length regulation.

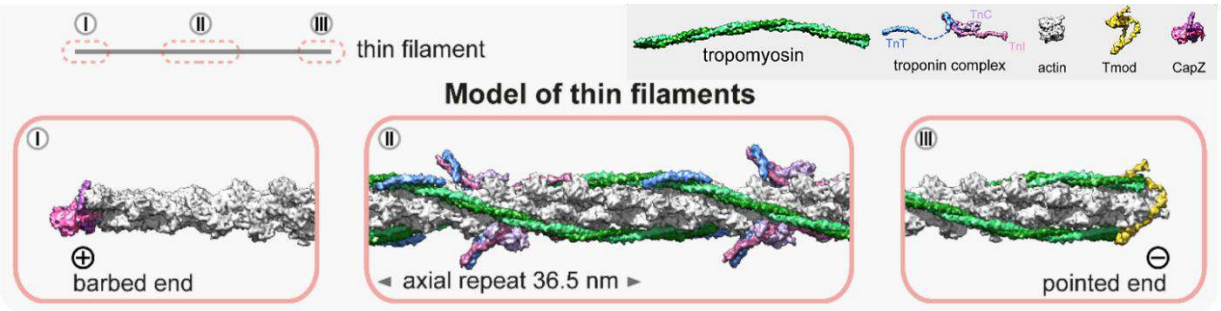

Figure 1.14 Molecular representation of the thin filament. The figure shows three main regions of the thin filament: (I) the barbed end, which is not covered by Tpm or Tn and is capped by the CapZ heterodimer; (II) the central region, which is associated with Tpm–Tn complex; and (III) the pointed end, which is capped by Tmod. Adapted from (Szikora et al., 2022), published under the CCA 4.0 International License.

Actin filament disassembly and severing are mainly controlled by the ADF/cofilin family of proteins. In vertebrates, this family includes ADF/destrin, cofilin-1 (Cof1), and cofilin-2 (Cof2). Cof1 is widely expressed in non-muscle tissues, whereas Cof2 is the predominant muscle isoform and is especially important for sarcomeric actin turnover. Structural studies show that cofilin contains distinct actin-binding surfaces that support interaction with G-actin and F-actin, allowing cofilin to regulate both actin monomer availability and filament stability (Hayden et al., 1993; Lappalainen & Drubin, 1997; Bamburg, 1999; Fass et al., 2004; Andrianantoandro & Pollard, 2006).

Cofilin binds at the interface between two subunits of the long-pitch helix. (Figure 1.15) Cofilin binds to F-actin with high positive cooperativity and a preference for ADP-actin. When cofilin binds to F-actin, it alters filament twist and weakens contacts between neighboring actin subunits, making the filament more susceptible to severing. Cofilin can sever actin filaments through building very small, asymmetrically growing clusters that preferentially extend toward pointed ends, suggesting that local structural changes, rather than large cofilin cluster formation or mechanical forces, are sufficient to promote filament severing (Bibeau et al., 2021). Severing often occurs near boundaries between cofilin-decorated and undecorated regions of the filament, where mechanical differences create local instability. This process generates new filament ends, which can either depolymerize or participate in further actin remodeling. Thus, cofilin does not simply remove actin subunits; it reorganizes filament architecture to promote controlled actin turnover (McGough et al., 1997; McCullough et al., 2011). Cofilin is assisted by a group of actin-binding proteins, such as coronin, cyclase-associated protein (CAP) and actin-interacting protein (Aip). Recent study showed that in the presence of CAP and cofilin, the rate of actin depolymerization exceeds spontaneous depolymerization at pointed end 330-fold (Shekhar et al., 2019; P. Li et al., 2025; Oosterheert et al., 2025; Palmer et al., 2026).

In striated muscle, Cof2 has a specific role in regulating thin filament length. Cof2 localizes near the central region of the sarcomere, close to the M-band, where it promotes actin filament disassembly at or near the pointed ends (Kremneva et al., 2014). This activity is important for trimming thin filaments and preventing uncontrolled elongation. Loss or depletion of Cof2 leads to abnormal filament length, irregular actin organization, and sarcomere disruption, demonstrating that cofilin-mediated turnover is necessary for maintaining uniform thin filament architecture (Ono, 2010; Agrawal et al., 2012).

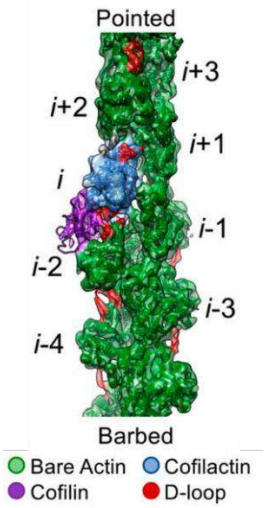

Figure 1.15 Cryo-EM reconstruction of cofilin bound to an actin filament. Adapted from (Huehn et al., 2020) published under the CCA 4.0 International License.

The activity of Cof2 is also influenced by other actin-binding proteins, especially Tpm. Tpm isoforms associated with contractile and cytoskeletal actin filaments differentially regulate cofilin-induced severing and depolymerization (Robaszkiewicz et al., 2016, 2023). In the absence of other regulatory proteins, muscle Tpm isoforms generally protect actin filaments from cofilin-mediated severing and depolymerization, although their effects on cofilin affinity for actin may be relatively modest. Tpms generally protect actin filaments from Cof2-induced depolymerization, with muscle Tpm isoforms showing the strongest effect. In contrast, Cof1 activity is inhibited by Tpm3.1 and Tpm1.1, but not by the Tpm1.1/Tpm2.2 heterodimer. The effects on actin polymerization also differ between isoforms: Cof2 inhibits polymerization directly, whereas Cof1 requires Tpm to acquire this inhibitory effect. Cofilins remove Tpm from actin filaments, but with different efficiencies depending on the Tpm and cofilin isoform involved. This suggests that Tpm may regulate cofilin activity mainly by modifying filament accessibility or structural flexibility rather than completely preventing cofilin binding (Robaszkiewicz et al., 2016).

Generally, thin filament length correlates well with the physiological requirements of the muscle, as slow-twitch fibers have longer thin filaments, while thin filaments in fast-twitch fibers are shorter (Granzier et al., 1991; Castillo et al., 2009; Gokhin et al., 2010, 2012). This observation also suggests that slow-twitch muscles have longer optimal sarcomere resting lengths, which might be one reason as to why they are able to efficiently maintain longer-term contractions. Therefore, to achieve optimal contraction characteristics, the thin filament length is expected to be precisely specified.

Taken together, these findings indicate that thin filament length and stability are maintained through a balance between filament protection and disassembly. Tmod limits actin subunit exchange at the pointed end, Tpm stabilizes the filament and regulates the access of actin-binding proteins, and Cof2 promotes controlled filament severing and depolymerization. Collectively, these mechanisms preserve the structural integrity and organization of thin filaments within the sarcomere while allowing the actin turnover required for muscle maintenance and repair.

1.6 Congenital Muscle Diseases

Skeletal muscle genetic disorders are caused by mutations in various sarcomeric proteins, as well as proteins involved in membrane stability, excitation-contraction coupling, calcium handling, mitochondrial function, and neuromuscular transmission. These disorders include a broad spectrum of neuromuscular and skeletal muscle diseases, such as muscular dystrophies, congenital myopathies, metabolic myopathies, mitochondrial myopathies, and distal arthrogryposis. Although their clinical presentation is highly variable, common features include muscle weakness, hypotonia, delayed motor development, exercise intolerance, respiratory involvement, and joint contractures (Ravenscroft et al., 2015; Dowling et al., 2021).

Congenital myopathies are a heterogeneous group of inherited skeletal muscle diseases that usually present at birth or in early childhood with hypotonia, muscle weakness, delayed motor development, and variable respiratory involvement. Although these disorders are rare, they are clinically important because severe forms can cause feeding problems, respiratory insufficiency, scoliosis, joint contractures, and long-term motor disability (Cassandrini et al., 2017; Ravenscroft et al., 2018; Papadimas et al., 2020; Zhang et al., 2024). Pathological findings in muscle biopsies from patients with congenital myopathies reveal a range of histopathological features, as shown in Figure 1.16.

Congenital myopathies are caused by pathogenic variants in genes required for normal skeletal muscle structure, contraction, calcium signaling, membrane organization, and muscle development. More than 30 causative genes have been associated with congenital myopathies, and recent reviews describe more than 40 clinicopathological forms. The inheritance pattern may be autosomal dominant, autosomal recessive, X-linked, or caused by a *de novo* mutation. One major group of causative genes encodes proteins of the thin filament, including *ACTA1*, *NEB*, *TPM2*, *TPM3*, *TNNT1*, *TNNT3*, *CFL2*, and *LMOD3* (Ravenscroft et al., 2018; Papadimas et al., 2020; Zhang et al., 2024).

Nemaline myopathy is one of the best-characterized congenital myopathies and is defined by the presence of nemaline rods, also called nemaline bodies, in skeletal muscle fibers. Clinically, nemaline myopathy usually presents with generalized muscle weakness, hypotonia, facial weakness, delayed motor development, and sometimes respiratory muscle involvement. The most common genes that cause nemaline myopathy are *NEB* and *ACTA1*, but mutations in *TPM2*, *TPM3*, *TNNT1*, *TNNT3*, *CFL2*, *KBTBD13*, *KLHL40*, *KLHL41*, *LMOD3*, *MYPN*, and other genes have also been reported (Sewry et al., 2019).

Congenital fiber-type disproportion (CFTD) is a disease diagnosed based on differences in number and size of skeletal muscle fibers. The hallmark of this type of myopathy is a decrease in size of slow, type 1 muscle fibers. CFTD is genetically heterogeneous and often is associated with mutations in *TPM3*, *RYR1*, *ACTA1*, *TPM2*, *SEPN1*, *MYH7*, *TTN*, *SCN4A*. *TPM3* has been described as an important genetic cause of this subtype, while *TPM2* is a rarer but well-established cause (Cassandrini et al., 2017; Papadimas et al., 2020).

Cap myopathy is a rare congenital myopathy characterized by cap-like structures at the periphery of muscle fibers. These cap structures are associated with myofibrillar disruption, thickened Z-lines, and abnormal accumulation of thin filament proteins. Cap myopathy overlaps clinically and genetically with nemaline myopathy and congenital fiber-type disproportion, especially in cases caused by *TPM2* or *TPM3* mutations (Marttila et al., 2014; Cassandrini et al., 2017; Sewry et al., 2019).

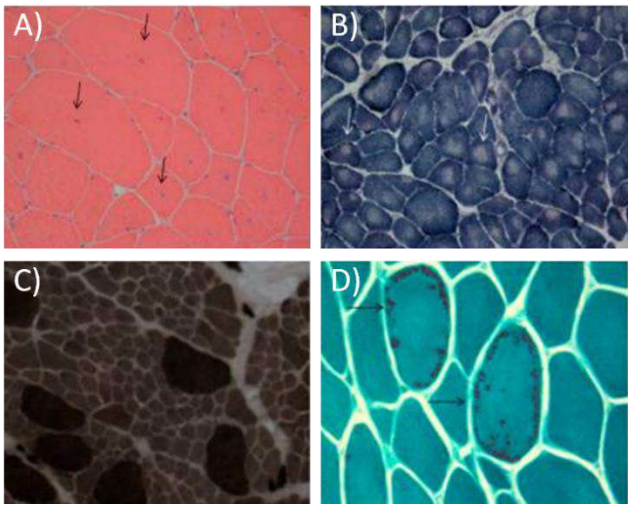

Figure 1.16 Muscle biopsy findings in congenital myopathies: (A) prominent centrally located nuclei (arrow) in centronuclear myopathy, H&E stain, ×20; (B) prominent central cores (arrow) in central core disease, NADH stain, ×20; (C) type 1 fiber hypotrophy, shown as lighter fibers relative to darker type 2 fibers, in congenital fiber-type disproportion, ATPase pH 9.4 stain, ×20; and (D) nemaline rods within muscle fibers (arrow) in nemaline myopathy, Gomori trichrome stain, ×40. Adapted from (Papadimas et al., 2020) published under the CC BY 4.0 international License.

Distal arthrogryposis (DA) is a clinically and genetically heterogeneous group of disorders characterized by congenital contractures mainly affecting the hands and feet. DA1 is usually autosomal dominant and presents with clenched fists, overlapping fingers, ulnar deviation, camptodactyly, and positional foot deformities. DA2B is considered a milder form of Freeman-Sheldon syndrome (DA2A) and includes similar distal joint involvement, often with facial features such as a triangular face, down-slanting palpebral fissures, small mouth, prominent chin, and short stature. Distal arthrogryposis is not primarily considered a muscle disease. Rather, it is a group of congenital limb contracture disorders characterized by multiple contractures affecting predominantly the hands and feet. Therefore, DA belongs to the broader category of arthrogryposis multiplex congenita (Tajsharghi, Kimber, et al., 2007; Kowalczyk & Feluś, 2016).

Congenital muscle diseases are disorders in which the primary defect is in skeletal muscle, however, distal arthrogryposis is defined by congenital joint contractures, with muscle weakness usually being mild or absent. The contractures in distal arthrogryposis are thought to result from reduced fetal movement (fetal akinesia) during development. Interestingly, there is considerable genetic overlap between distal arthrogryposis and congenital myopathies. Many DA-associated genes encode the sarcomeric proteins (*TPM2, TNNI2, TNNT3,* etc.). Mutations in these genes can impair muscle contraction during fetal development. If fetal movement is sufficiently reduced, congenital contractures develop. Thus, although the underlying molecular defect often involves muscle contractile proteins, the clinical phenotype is dominated by joint contractures rather than muscle weakness (Kowalczyk & Feluś, 2016; Papadimas et al., 2020; Whittle et al., 2021).

Mutations in Tpm genes can disturb thin filament regulation and lead to congenital myopathies and other contractile disorders. Pathogenic variants may increase or decrease calcium sensitivity, alter Tpm's affinity for actin, or destabilize its coiled-coil structure, which can produce either hypercontractile phenotypes such as distal arthrogryposis or hypocontractile phenotypes such as nemaline myopathy and related congenital myopathies (Robinson et al., 2007; Clarke, 2008).

In skeletal muscle, mutations in *TPM2* are classically associated with congenital myopathies such as nemaline myopathy, cap myopathy, congenital fiber-type disproportion but some of them are also related with distal arthrogryposis, Escobar syndrome, and multiple pterygium syndrome. Most *TPM2*-related congenital myopathies or distal arthrogryposes are

autosomal dominant, although rare recessive cases have also been reported. Figure 1.17 summarizes location of missense mutation sites within the exons of *TPM2* (Marttila et al., 2014; Ochala et al., 2012; Quijano-Roy et al., 2012; Tajsharghi et al., 2012; Vogt et al., 2020).

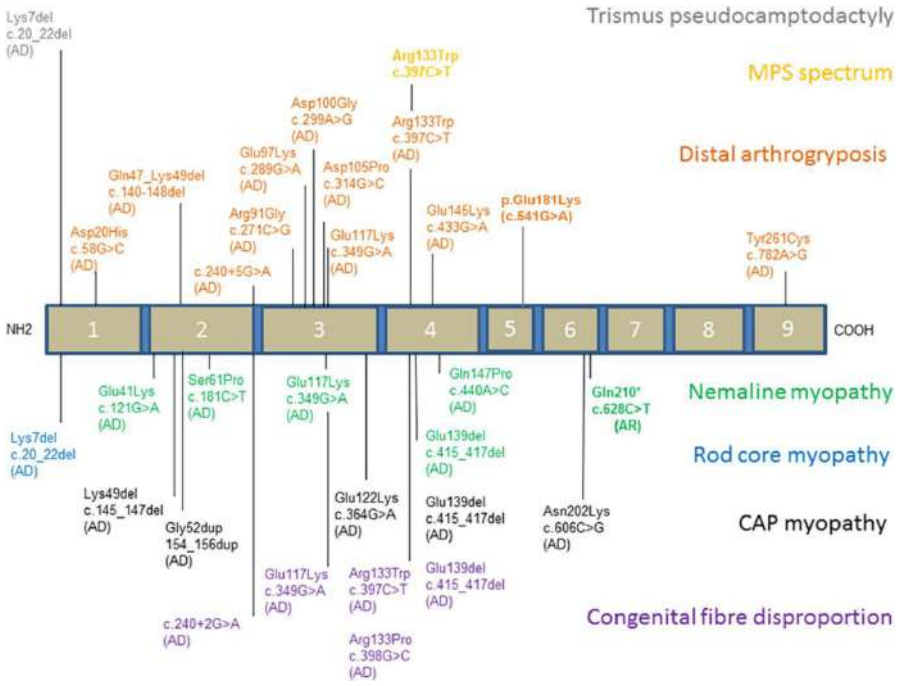

Figure 1.17 Schematic illustration of the representative mutation sites within the exons of *TPM2* reported to date. Adapted from (Vogt et al., 2020) with permission from *Wiley*.

1.7 Disease-causing mutations as a tool in deciphering structure-function relationships in Tpm2.2

Missense mutations in *TPM2* give rise to single amino acid substitutions distributed throughout the Tpm2.2 molecule (Figure 1.17) and are thought to be the primary cause of several forms of inherited muscle disease. The pathological consequences of these mutations provide compelling evidence for the functional importance of the affected regions of Tpm2.2. In this sense, disease-causing mutations can be regarded as "experiments" performed by Nature, revealing residues and structural elements that are essential for proper muscle function. Because these natural experiments occur in the context of the whole organism throughout development, their clinical manifestations are influenced by numerous genetic, developmental, and physiological factors, resulting in considerable phenotypic variability among affected individuals. By contrast, biochemical analyses of individual Tpm2.2 variants allow specific functions of the protein to be examined in isolation, providing insight not only into the molecular mechanisms underlying pathological states, but also into the structure–function relationships that govern the activity of the entire protein. Therefore, *in vitro* characterization

of disease-associated Tpm2.2 mutations provides valuable insight into the molecular mechanisms that regulate thin filament function in health and disease.

2 Aims and Objectives of the Thesis

Tpm plays a central role in regulating the timing and extent of muscle contraction through its interactions with actin, myosin, Tn complex, and other sarcomeric proteins. Despite decades of investigation of the molecular mechanisms of Tpm-mediated regulation, it is still not fully understood how Tpm integrates regulation of the contractile cycle of muscle and the thin filament integrity.

The main aim of the dissertation was to decipher how structural alterations within actin-binding periodic repeats determine multiple functions of Tpm2.2.

To execute this goal, four disease-linked missense mutations in *TPM2* were selected based on their localization within the first or second half of the actin-binding periods P1 and P5. The D20H and E181K substations in Tpm2.2, positioned within the first halves of P1 and P5, respectively, have been reported to cause hypercontractile phenotypes in individuals with distal arthrogryposis. Conversely, the E41K and N202K substations, located within the second halves of P1 and P5, respectively, are associated with nemaline myopathy and cap disease, disorders characterized by reduced contractile function and hypocontractile muscle phenotypes.

Effects of these mutations on different Tpm2.2 functions were tested in an array of biochemical assays to achieve the following specific goals:

1) To evaluate how the four selected substitutions alter interactions of Tpm2.2 with the thin filament.
2) To characterize the impact of the mutations on regulation of the actomyosin ATPase cycle.
3) To decipher the effect of mutations on Ca^{2+}-sensitivity of the Tpm2.2-Tn regulatory complex.
4) To analyze effects of the mutations on myosin motor function.
5) To investigate the role of *TPM2* mutations in the thin filament dynamics, stability and length regulation by Cof2 and Tmod1.

3 Materials

3.1 Preparation of muscle proteins

The following muscle proteins were utilized in this research: actin, myosin (specifically the proteolytic myosin S1 and HMM), Tpm, Tn complex and other related muscle proteins. The compositions of the solutions and buffers employed during the isolation of individual muscle proteins are detailed in the subsequent subsections.

3.1.1 Materials for actin isolation

Actin for this research was obtained from chicken skeletal muscle, specifically from pectoral muscles that had been cleared of connective tissue membranes. The compositions of the solutions and buffers used during the standard actin isolation procedure (Spudich & Watt, 1971) are presented in Table 3.1.

Table 3.1 Solutions and buffers for actin isolation.

Name	**Composition**
Guba-Straub solution	0.15 M phosphate buffer, pH 6.5 KH_2PO_4 K_2HPO_4 0.3 M KCl
Actin extraction solution I	0.4% $NaHCO_3$ 0.1 mM $CaCl_2$
Actin extraction solution II	10 mM $NaHCO_3$ 10 mM Na_2CO_3 0.1 mM $CaCl_2$
Extraction Buffer G	5 mM Tris-HCl, pH 7.6 0.1 mM $CaCl_2$ 0.2 mM ATP 1 mM DTT 0.02 % NaN_3
Polymerizing salts	0.6 M KCl (*in substantia*) 2 mM $MgCl_2$

3.1.2 Materials for myosin isolation and the preparation of myosin-S1 and HMM

The head domain of myosin isoform II, specifically myosin-S1 and HMM were obtained by TLCK-treated α-chymotrypsin digestion (Sigma-Aldrich, Darmstadt, Germany) of rabbit skeletal myosin. The compositions of the solutions used for the preparation of myosin, myosin-

S1 and HMM according to the standard procedure (Margossian & Lowey, 1982) are presented in Table 3.2 and Table 3.3.

Table 3.2 Solutions for myosin isolation and preparation of myosin-S1.

Name	**Composition**
Guba-Straub solution with PMSF	0.15 M phosphate buffer, pH 6.5 K_2HPO_4 KH_2PO_4 0.3 M KCl 0.2 mM PMSF
Dialysis buffer	2 mM $MgCl_2$ 0.2 M CH_3COONH_4 (Ammonium acetate) 0.1 mM PMSF
Digestion buffer	20 mM K-PIPES, pH 7.0 120 mM NaCl 2.5 mM K-EDTA, pH 8.0 1 mM DTT
Low-salt buffer prior to ion-exchange (Q-Sepharose FF) chromatography	20 mM K-PIPES, pH 7.0 1 mM DTT
High-salt buffer	20 mM K-PIPES, pH 7.0 1 mM DTT 0 – 0.6 M NaCl

HMM, containing both heads connected by a short fragment of the tail (subfragment 2, S2), was obtained by digestion of myosin with TLCK-treated chymotrypsin (Sigma-Aldrich, Darmstadt, Germany). The compositions of the solutions and buffers used for the preparation of HMM are presented in Table 3.3.

Table 3.3 Solutions and buffers for HMM preparation

Name	**Composition**
Myosin buffer	20 mM K-PIPES, pH 7.0 120 mM NaCl 1 mM DTT 2.5 mM K-EDTA, pH 8.0
Digestion buffer	0.05 mg/ml TLCK-treated α-chymotrypsin Myosin buffer
Digestion stop solution	0.5 mM PMSF 100% ethanol
Dialysis buffer	40 mM KCl

	10 mM imidazole, pH 7.0 1 mM DTT

3.1.3 Materials for troponin isolation

The troponin complex for this research was obtained from rabbit skeletal muscle. The compositions of the solutions and buffers used for the isolation of the troponin complex according to the standard procedure (Potter, 1982) are presented in Table 3.4.

Table 3.4 Solutions and buffers for troponin isolation.

Name	**Composition**
Triton solution	1% Triton X-100 50 mM KCl 5 mM Tris-HCl, pH 8.0
Triton solution with protease inhibitors	As above (*id.*) chymostatin (6.08 μg/ml in DMSO) leupeptin (5 μg/ml in H_2O) benzamidine (100 μg/ml in H_2O) pepstatin (1 μg/ml in ethanol) PMSF (17.4 μg/ml in isopropanol)
Extraction buffer with Protease inhibitors	1 M KCl 25 mM Tris-HCl, pH 8.0 0.1 mM $CaCl_2$ 0.1 mM DTT chymostatin (6.08 μg/ml in DMSO) leupeptin (5 μg/ml in H_2O) benzamidine (100 μg/ml in H_2O) pepstatin (1 μg/ml in ethanol) PMSF (17.4 μg/ml in isopropanol)
Dialysis buffer prior to DEAE Sepharose chromatography	20 mM Tris-HCl pH 7.5 0.1 mM $CaCl_2$ 0.5 mM DTT 0.02% NaN_3 chymostatin (6.08 μg/ml in DMSO) leupeptin (5 μg/ml in H_2O) benzamidine (100 μg/ml in H_2O) pepstatin (1 μg/ml in ethanol) PMSF (17.4 μg/ml in isopropanol)
Elution buffer	20 mM Tris-HCl pH 7.5 0.1 mM $CaCl_2$

	0.5 mM DTT 0.02% NaN_3 chymostatin (6.08 µg/ml in DMSO) leupeptin (5 µg/ml in H_2O) benzamidine (100 µg/ml in H_2O) pepstatin (1 µg/ml in ethanol) PMSF (17.4 µg/ml in isopropanol) 0 – 0.6 M NaCl

3.2 Competent cells

Three different *E. coli* strains were used in this study: *E. coli* XL1-Blue (Agilent, Santa Clara, CA, United States), DH5α (Agilent, Santa Clara, CA, United States), and BL21(DE3) (Novagen, Darmstadt, Germany). The XL1-Blue strain was transformed with linear DNA obtained after PCR amplification and was used for propagation and circularization of the mutated DNA construct. The DH5α (Dam^+) strain was transformed with circular plasmid DNA and served for plasmid amplification. The BL21(DE3) strain was used for the expression of recombinant proteins encoded by the corresponding cDNA constructs. The characteristics of the bacterial strains used are summarized in Table 3.5.

Table 3.5 Characteristics of *E. coli* strains used in this study

Bacterial strain	**Characteristics**
XL-1 Blue	*Genotype:* endA1 gyrA96 (nal^R) thi-1 recA1 relA1 lac glnV44 F'[::Tn10 $proAB^+$ $lacI^q$ Δ(lacZ)M15] hsdR17(r_K^- m_K^+); *Characteristics:* resistant to tetracycline and nalidixic acid; *Growth medium used during transformation:* NZY medium (0.5% yeast extract, 0.5% NaCl, pH 7.5, 1% casein)
DH5α	*Genotype:* F^- endA1 glnV44 thi-1 recA1 relA1 gyrA96 deoR nupG Φ80d*lacZ*ΔM15 Δ(*lacZYA-argF*)U169, hsdR17(r_K^- m_K^+), λ–; *Characteristics:* resistant to nalidixic acid; *Growth medium used during transformation:* LB broth medium (0.5 % yeast extract, 1% NaCl, 1% peptone)
BL-21 (DE3)	*Genotype:* $F^–$ ompT gal dcm lon $hsdS_B(r_B^-$ $m_B^-)$ λ(DE3 [lacI lacUV5-T7 gene 1 ind1 sam7 nin5]); *Characteristics:* expression strain containing the λ prophage with the gene encoding T7 RNA polymerase under control of the lacUV5 promoter and the lacIq gene. Expression is negatively regulated by the lac operator and induced by IPTG;

	Growth medium used during transformation: SOC medium (20 mM glucose, 0.5% yeast extract, 0.05% NaCl, 2.5 mM KCl, 10 mM $MgCl_2$, 10 mM $MgSO_4$, 2% peptone,

3.3 Solutions for the production and purification of recombinant wild-type Tpm2.2 and its variants

Recombinant wild-type skeletal Tpm2.2 and its variants were expressed in the *E. coli* strain BL21(DE3) (Novagen, Darmstadt, Germany). Bacterial cultures were grown on agar plates (1.2% agar dissolved in LB Broth medium) as well as in LB Broth medium (0.5 % yeast extract, 1% NaCl, 1% peptone). Ampicillin was used as a selective agent at a final concentration of 50 μg/ml.

The composition of reagents used for the isolations of wild-type skeletal Tpm2.2 and its variants from bacterial cells and their subsequent purification are presented in Table 3.6.

Table 3.6 Composition of reagents used for the production and purification of Tpm2.2 from BL21(DE3) cells.

Steps	**Composition**
Lysis buffer	50 mM Tris-HCl, pH 7.5 0.5 mg/ml lysozyme 20% saccharose 10 mM EDTA
Dialysis buffer to remove the excess of salt	20 mM Tris-HCl, pH 7.5 0.5 mM DTT 0.02% NaN_3
Chromatographic separation on DEAE–cellulose (elution buffer)	20 mM Tris-HCl, pH 7.5 0.5 mM DTT 0 – 1 M NaCl
Dialysis buffer (after chromatography)	30 mM NaCl 2 mM $MgCl_2$ 1 mM DTT 5 mM imidazole, pH 7,0 0.02% NaN_3

3.4 Solutions for polyacrylamide electrophoresis

To separate proteins according to their molecular weights, polyacrylamide gel electrophoresis under denaturing conditions (SDS-PAGE) was used. SDS-PAGE gels were prepared using the solutions listed in Table 3.7.

Table 3.7 Composition of buffers and solutions used for SDS-PAGE.

Name	**Composition**
10% resolving gel	10% acrylamide–bisacrylamide 0.38 M Tris-HCl, pH 8.5 0.1% SDS 0.1% TEMED 0.1% ammonium persulfate
12% resolving gel	12% acrylamide–bisacrylamide 0.38 M Tris-HCl, pH 8.5 0.1% SDS 0.1% TEMED 0.1% ammonium persulfate
15% resolving gel	15% acrylamide–bisacrylamide 0.38 M Tris-HCl, pH 8.5 0.1% SDS 0.1% TEMED 0.1% ammonium persulfate
5% stacking gel	5% acrylamide–bisacrylamide 0.125 M Tris-HCl, pH 6.8 0.1% SDS 0.1% TEMED 0.1% ammonium persulfate
Sample buffer (Laemmli buffer)	0.06 M Tris-HCl, pH 6.8 25% glycerol 2% SDS 0.01% bromophenol blue 5% β-mercaptoethanol
Fixing solution	50% methanol 10% glacial acetic acid
Staining solution	0.25% Coomassie Brillant Blue G250 50% methanol 10% glacial acetic acid
Distaining solution	50% methanol 10% glacial acetic acid

3.5 Binding of Tpm2.2 variants to F-actin

Binding of Tpm2.2 variants to F-actin was tested either in the absence or presence of Tn by a cosedimentation assay. The composition of solutions used for this assay is presented in Table 3.8.

Table 3.8 Composition of buffers and solutions used for binding of Tpm2.2 variants to F-actin.

Name	Composition
Actin polymerization buffer	5 mM Tris-HCl, pH 7.6 0.1 mM $CaCl_2$ 0.2 mM ATP 1 mM DTT 0.02 % NaN_3 30 mM NaCl 2 mM $MgCl_2$
Actin binding buffer (ABB)	30 mM NaCl 2 mM $MgCl_2$ 5 mM imidazole, pH 7.0 0.5 mM DTT

3.6 Binding of Cof2 to F-actin in the absence and presence of the thin filament regulatory proteins

Binding of Cof2 to the F-actin-Tpm complex was assessed by co-sedimentation. The composition of solutions used for this assay is presented in Table 3.9.

Table 3.9 Composition of buffers and solutions used for binding of Cof2 to F-actin.

Name	Composition
Actin polymerization buffer	5 mM Tris-HCl, pH 7.6 0.1 mM $CaCl_2$ 0.2 mM ATP 1 mM DTT 0.02 % NaN_3 100 mM NaCl 2 mM $MgCl_2$
Actin binding buffer (ABB)	100 mM NaCl 2 mM $MgCl_2$ 5 mM Tris-HCl, pH 7.5 1 mM DTT

3.7 Binding of Tmod1 to F-actin

Binding of Tmod1 to the pointed end of the F-actin-Tpm and F-actin-Tpm-Tn + Ca^{2+} complexes with their barbed-end capped with CapZ was assessed by co-sedimentation followed by SDS–PAGE analysis of the pelleted fractions and subsequent detection of Tmod1 by Western blot. The composition of solutions used for this assay is presented in Table 3.10.

Table 3.10 Composition of buffers and solutions used for binding of Tmod1 to the pointed end of the F-actin-Tpm and F-actin-Tpm-Tn + Ca^{2+} complexes.

Name	Composition
Actin polymerization buffer	5 mM Tris-HCl, pH 7.6
	0.1 mM $CaCl_2$
	0.2 mM ATP
	1 mM DTT
	0.02 % NaN_3
	100 mM KCl
	2 mM $MgCl_2$
Assay buffer (AB)	100 mM KCl
	2 mM $MgCl_2$
	5 mM Tris-HCl, pH 7.6
	0.2 mM ATP
	0.5 mM DTT

Western blot analysis was performed using the semi-dry electroblotting Trans-Blot Turbo system (Bio-Rad, Hercules, CA, USA). Proteins were separated by SDS-PAGE using 12% TGX Stain-Free gels (Bio-Rad, Hercules, CA, USA). Protein transfer was carried out onto a 0.45 µm LF (low-fluorescence) PVDF membrane using the Trans-Blot Turbo Transfer Membranes & Filter Paper Kit (Bio-Rad, Hercules, CA, USA).

For detection of Tmod1 bound to actin, rabbit polyclonal IgG primary antibodies (Abcam, Cambridge, UK) were applied, followed by goat anti-rabbit IgG secondary antibodies (Bio-Rad, Hercules, CA, USA). Immunoreactive bands were visualized using the enhanced chemiluminescence Clarity Max Western ECL Substrate system (Bio-Rad Laboratories, Hercules, CA, USA).

3.8 Materials used for actomyosin ATPase assays

Actomyosin ATPase measurements were performed in 96-well plates at 25 °C using the NADH-coupled assay. The composition of solutions used for the NADH-coupled assay is presented in Table 3.11.

Table 3.11 Composition of solutions for actomyosin ATPase activity measurements by using malachite green assay.

Name	Composition
ATPase buffer	25 mM HEPES pH 7.3
	25 mM KCl
	5 mM $MgCl_2$

	1 mM DTT
Reaction buffer	0.3 µM S1 2 mM ATP 0.4 mM NADH 10 U/ml lactate dehydrogenase 1 mM Phosphoenol-pyruvate (PEP) 20 U/ml pyruvate kinase

The composition of solutions used for the measurement of actomyosin ATPase activity is presented in Table 3.12. Inorganic phosphate (P_i) released during ATP hydrolysis was quantified colorimetrically using the ferrous ammonium sulfate-molybdate method, in which phosphomolybdate complexes formed under acidic conditions were reduced to yield a blue-colored complex measurable spectrophotometrically.

Table 3.12 Composition of solutions for actomyosin ATPase activity measurements by using malachite green assay.

Name	**Composition**
Starting buffer (pH 7.0)	24 mM ATP 25 mM $MgCl_2$
Phosphate buffer	1 mM KH_2PO_4 10 mM KH_2PO_4
Stopping buffer	13.3% SDS 0.12 M EDTA, pH 7.0
Coloring reagent	0.5% $(NH_4)_6Mo_7O_{24}$ x $4H_2O$ 0.5 M H_2SO_4 30 mM $FeSO_4$

Actomyosin ATPase sensitivity to varying Ca^{2+} concentrations was measured using Ca^{2+}/EGTA buffers containing defined concentrations of free calcium ions (Table 3.13).

Table 3.13 Composition of solutions containing defined free Ca^{2+} concentrations.

Free Ca^{2+} concentration	**Volume ratio EGTA/CaEGTA**	**8 mM EGTA [mL]**	**8 mM Ca / 8 mM EGTA [mL]**
$1x10^{-7}$	1.90	4.75	2.50
$2x10^{-7}$	0.95	2.50	2.63
$4x10^{-7}$	0.46	2.50	5.26
$6x10^{-7}$	0.32	1.25	3.95
$8x10^{-7}$	0.24	1.25	5.27

$1x10^{-6}$	0.19	0.63	3.29
$3x10^{-6}$	0.08	0.25	3.29
$6x10^{-6}$	0.03	0.16	3.95
$8x10^{-6}$	0.02	0.16	5.27
$1x10^{-5}$	0.02	0.05	3.29

Free Ca^{2+} concentrations were calculated using the online PyChelator web tool (https://amrutelab.github.io/PyChelator/) with ionic strength determined using an online ionic strength calculator (http://calistry.org/calculate/ionic-strength-calculator) based on the EGTA/CaEGTA buffering system and the appropriate stability constants for the experimental pH and temperature.

3.9 Single turnover measurements of myosin-actin interactions

Single turnover experiments were performed to determine acto-myosin dissociation kinetics and individual ATP hydrolysis events under conditions where myosin heads were allowed to hydrolyze only one ATP molecule. The composition of solutions used for this assay is presented in Table 3.14.

Table 3.14 Composition of buffers and solutions used for single turnover experiments.

Name	**Composition**
ST Assay buffer (AB)	25 mM KCl 5 mM $MgCl_2$ 25 mM Hepes, pH 7.3 0.5 mM DTT

3.10 *In vitro* motility assay

In vitro motility assay was used to analyze actin filament sliding velocities and the functional effects of nucleotide-dependent conformational changes in myosin on force generation and actomyosin communication. The composition of solutions used for this assay is presented in Table 3.15.

Table 3.15 Composition of buffers and solutions used for *in vitro* motility assay.

Name	**Composition**
IVM Assay buffer (AB)	25 mM MOPS, pH 7.4 25 mM KCl

	4 mM $MgCl_2$ 1 mM EGTA 1 mM DTT
Blocking buffer	1% (w/v) Bovine Serum Albumin (BSA) In IVM assay buffer as above (*id.*)
Reaction buffer	0.05 % (w/v) BSA 2 mM ATP 0.4 % (w/v) methylcellulose 30 mM glucose 250 U/ml catalase 25 U/ml glucose oxidase In IVM assay buffer as above (*id.*)

3.11 Measurement of Tpm–Tn interactions using an indirect ELISA assay

Indirect Enzyme Linked Immunosorbent Assay (ELISA) was used to determine interactions between Tpm and Tn in the absence of F-actin. The composition of solutions used for this assay is presented in Table 3.16.

Table 3.16 Composition of buffers and solutions used for an indirect ELISA assay.

Name	**Composition**
ELISA Assay buffer (AB)	25 mM MOPS, pH 7.4 25 mM KCl 5 mM $MgCl_2$ 1 mM EGTA 10 mM DTT
Blocking buffer	5% (w/v) BSA 0.05% Tween-20 Phosphate-buffered saline
TPM2 rabbit polyclonal primary antibody (Proteintech, Manchester, England)	Diluted 1:330 in blocking buffer
Goat anti-rabbit secondary antibody conjugated to horseradish peroxidase (ThermoScientific, MA, USA)	Diluted 1:500 in blocking buffer
TMB Peroxidase EIA Substrate solution (Bio-Rad, Hercules, CA, USA)	

3.12 Assessment of Tpm2.2 and Cof2-mediated regulation of actin filament length, severing and depolymerization

Actin dynamics were analysed by using F-actin labeled with tetramethyl-rhodamine cadaverine (TRC) (Zedira, Darmstadt, Germany) using bacterial transglutaminase. TRC-labeled filaments were visualized using an Olympus IX83 microscope. To analyze the impact of Tpm2.2 and Cof2 on actin stability, TRC-labeled filaments were introduced in flow cells coated with positively charged lipids. To evaluate how Tpm2.2 variants influence filament length during actomyosin interactions, flow cells were coated with HMM. The composition of solutions used for this assays are presented in Table 3.17.

Table 3.17 Composition of buffers and solutions used for regulation of actin filament length, severing and depolymerization.

Name	**Composition**
FM Assay buffer (AB)	25 mM MOPS, pH 7.4 25 mM KCl 4 mM $MgCl_2$ 1 mM EGTA 1 mM DTT
Blocking buffer	0.05% (w/v) Bovine Serum Albumin (BSA) In FM assay buffer as above (*id.*)
Oxygen-scavenging system	30 mM glucose 250 U/ml catalase 25 U/ml glucose oxidase In FM assay buffer as above (*id.*)
Reaction buffer	0.05 % (w/v) BSA 2 mM ATP 0.4 % (w/v) methylcellulose 30 mM glucose 250 U/ml catalase 25 U/ml glucose oxidase In FM assay buffer as above (*id.*)

3.13 Equipment

The following main laboratory equipment was used in this study:

- Protein electrophoresis apparatus Mini-PROTEAN 3 Cell (Bio-Rad Laboratories, Hercules, CA, USA)

- Semi-dry electroblotting apparatus Trans-Blot Turbo system (Bio-Rad, Hercules, CA, USA)
- Microplate reader iMark (Bio-Rad, Hercules, CA, USA)
- Synergy4 microplate reader (Bio-Tek, Winooski, Vermont, USA)
- Fluorescence microscope Olympus IX83 (Olympus Corporation, Tokyo, Japan)
- Spectrofluorometer Jasco, FP 8350 spectrofluorometer (Tokyo, JAPAN)
- UV–VIS spectrophotometer GENESYS 180 (Thermo Fisher Scientific Inc., Waltham, MA, USA) and UV–VIS spectrophotometer BioSpectrometer (Eppendorf AG, Hamburg, Germany)
- Low-pressure chromatography system BioLogic and NGC Chromatography System (Bio-Rad Laboratories, Hercules, CA, USA)
- Ultracentrifuge Optima L-90K (Beckman Coulter, Brea, CA, USA)
- Hi-tech Scientific SF61 double mixing stopped-flow system (TgK Scientific Limited, Bradford on Avon, UK
- Spectrofluorometer FluoroMax-4 (HORIBA Jobin Yvon, Kyoto, Japan)
- OriginPro® software (Northampton, MA, USA)
- SigmaPlot 12.0, software (Systat Software Inc., San Jose, CA, USA)

The following auxiliary laboratory equipment was used in this study:

- Thermal cycler DNA Engine (Bio-Rad Laboratories, Hercules, CA, USA)Autoclave MLS-3751L (Panasonic Healthcare Co., Ltd., Tokyo, Japan)
- Overhead homogenizer RZR 2021 (Heidolph Instruments GmbH, Schwabach, Germany)
- High shear homogenizer Silent crusher M (Heidolph Instruments GmbH, Schwabach, Germany)
- Ultrasonic homogenizer Sonopuls HD 2070 (Bandelin Electronic GmbH & Co. KG, Berlin, Germany)
- Shaking incubator SM-30 CONTROL TH30 (Edmund Bühler GmbH, Hechingen, Germany)
- Rocking platform Duomax 1030 (Heidolph Instruments GmbH, Schwabach, Germany)
- pH meter CP-401 (Elmetron Sp. z o.o., Zabrze, Poland)
- Ultrasonic cleaner U-501 (Ultron UAB, Vilnius, Lithuania)
- Single-stage vacuum filtration pump 4EKF56CX-4 (ABM Greiffenberger Antriebstechnik GmbH, Marktredwitz, Germany)
- Ultrapure water purification system Milli-Q EQ 7008 (MilliporeSigma, Burlington, MA, USA)
- Circulating thermostat HAAKE DC10 with HAAKE K10 bath (Thermo Haake GmbH, Karlsruhe, Germany)
- Circulating water bath Thermo Scientific A25 (Thermo Fisher Scientific, Waltham, MA, USA)
- Refrigerated circulating bath Thermo Scientific AC200 (Thermo Fisher Scientific, Waltham, MA, USA)

4 Methods

4.1 Preparation of muscle proteins

4.1.1 Preparation of G-actin from skeletal muscle

Skeletal muscle acetone powder was prepared from rabbit or chicken fast skeletal muscle following the general approach of Feuer et al. (1948). Briefly, skeletal muscle was dissected from freshly sacrificed animals and kept on ice throughout the procedure to minimize proteolysis. Myosin-rich (dark red) muscle and connective tissues were carefully removed to enrich for fast skeletal muscle fibers. The cleaned muscle tissue was finely minced using a pre-cooled grinder to increase the surface area for subsequent solvent extraction. The minced tissue was then treated with cold acetone to remove lipids and other low molecular weight solutes, resulting in the precipitation and stabilization of structural proteins. The acetone-treated tissue was thoroughly dried to obtain a stable, delipidated powder containing actin, myosin fragments, and associated regulatory proteins. The resulting acetone powder was stored at –20 °C until further use for protein extraction and purification. The freshly extracted rabbit muscle used in the experiment was a gift from the Department of Pathobiochemistry and Clinical Chemistry, Collegium Medicum in Bydgoszcz. The animals were sacrificed according to the procedures approved by the Committee for Ethical Experiments on Animals of Collegium Medicum.

Actin was isolated from acetone powder according to Spudich and Watt (Spudich & Watt, 1971). One gram of rabbit skeletal muscle acetone powder was suspended in 20 mL of G-buffer (Table 3.1) and incubated at 4 °C for 15 minutes with gentle stirring. The suspension was filtered using a Büchner funnel connected to a vacuum pump, with the filter paper pre-equilibrated in G-buffer (qualitative filter paper 403, medium filtration rate, particle retention 5–10 µm; VWR, Cat. No. 0113A00004). For the first polymerization step, KCl and $MgCl_2$ were added to final concentrations of 50 mM and 2 mM, respectively, and the solution was incubated at room temperature for 1 h with gentle stirring. To remove regulatory proteins – Tpm and Tn, from actin filaments, KCl concentration was gradually increased to 0.6 M, followed by additional 1.5 h incubation at room temperature with stirring. The mixture was centrifuged at 40,000 rpm (164,178 x g) for 1 h at 4 °C using Beckman Coulter Type 70 Ti rotor. The supernatant was discarded, and the pellet was dissolved in approximately 4 mL of cold G-buffer. The suspension was homogenized on ice using a Potter–Elvehjem homogenizer and transferred into a dialysis membrane for overnight dialysis against G-buffer at 4 °C, with at least one buffer change. The dialyzed G-actin solution was centrifuged again at 40,000 rpm for

1 h at 4 °C using the Type 70 Ti rotor to remove residual impurities. G-actin was stored on ice in G-buffer and used within two weeks. Concentration of G-actin was determined spectrophotometrically using the Eppendorf BioSpectrometer® (Hamburg, Germany) from absorbance at 290 nm and extinction coefficient of 0.63 $mL.mg^{-1}.cm^{-1}$ for a 0.1% (w/v) actin solution (MW 42,000).

G-actin used in the polymerization experiments was gel-filtered on a Sephacryl® S-200 HR (Cytiva, Germany) column. The collected fractions were analyzed on the SDS-polyacrylamide gel electrophoresis (SDS-PAGE) to determine protein purity and pulled (Pardee & Spudich, 1982).

4.1.2 Preparation of myosin and its proteolytic subfragments

Myosin from rabbit skeletal muscle was isolated according to the standard procedure described by Margossian and Lowey (Margossian & Lowey, 1982), with minor modifications. Rabbit skeletal muscle tissue was finely dissected, minced, and homogenized. The resulting muscle homogenate was extracted with Guba–Straub solution supplemented with phenylmethylsulfonyl fluoride (PMSF), using three volumes of extraction buffer relative to the wet weight of the muscle tissue (See 3.1.1 in Materials section). After 10 minutes of extraction, the suspension was centrifuged for 20 minutes at 10,000 rpm. The obtained supernatant was subsequently diluted fourteenfold with deionized cold water and incubated for 2 hours at 4 °C to allow for myosin precipitation. Following removal of the supernatant by vacuum aspiration, the precipitate was collected by centrifugation for 30 minutes at 16,000 rpm. The resulting pellet was dissolved in 0.5 M KCl and again diluted fourteenfold with deionized cold water. The precipitated protein was recovered by centrifugation for 20 minutes at 19,000 rpm, after which the pellet was dissolved in a minimal volume of 0.5 M KCl. This solution was subjected to ultracentrifugation for 1.5 hours at 45,000 rpm using a Beckman 70 Ti rotor. The final supernatant was dialyzed against 0.2 M ammonium acetate (CH_3COONH_4) containing 2 mM $MgCl_2$. The concentration of myosin was determined spectrophotometrically at 280 nm using an extinction coefficient of 0.51 for a myosin solution at a concentration of 1 mg/ml. Myosin was either used directly or mixed 1:1 (v/v) with glycerol for long-term storage at −20 °C.

Single-headed myosin subfragment 1 (S1) and heavy meromyosin (HMM) containing two myosin heads were obtained by limited digestion of rabbit skeletal muscle myosin using TLCK-treated α-chymotrypsin as described in (Margossian & Lowey, 1982).

Myosin S1 was obtained from rabbit skeletal muscle myosin by full-length myosin glycerol stock was diluted 10-fold with cold digestion buffer (20 mM K-PIPES, pH 7.0, 120 mM NaCl, 2.5 mM K-EDTA, pH 8.0, 1 mM DTT) to a total protein amount of approximately 500 mg. The diluted myosin solution was stirred for 10 minutes at room temperature (RT) and then incubated for an additional 20 minutes at RT. Myosin filaments were sedimented by centrifugation at 16,000 rpm, 4 °C, for 20 minutes. The pellet was resuspended in 25 mL digestion buffer at room temperature to obtain a 2% thick-filament suspension (≈20 mg/mL^{-1}). TLCK-treated α-chymotrypsin was added to a final concentration of 0.05 mg/mL^{-1}. Digestion was carried out under slow stirring at room temperature for up to 30 minutes. Proteolysis was stopped by addition of PMSF to 1 mM final concentration followed by 10 minutes incubation at RT. The solution was centrifuged at 35,000 rpm, 4 °C, for 20 minutes to sediment insoluble material. The supernatant was dialyzed against 3 x 1 L of low-salt buffer (20 mM K-PIPES, pH 7.0, 1 mM DTT), 1 h per change, followed by overnight dialysis against fresh buffer. After dialysis, insoluble material was removed by centrifugation at 35,000 rpm, 4 °C, for 20 minutes. The dialyzed protein solution was filtered through a 0.22 µm filter. Myosin-S1 subfragments were separated from other components by ion-exchange chromatography (Q-sepharose FF). Pure fractions of myosin-S1 were collected after checking purity of chromatography fractions on SDS-PAGE. Protein concentration was determined by measuring absorbance at 280 nm and 320 nm. To account for light scattering, the absorbance at 320 nm was subtracted from the absorbance at 280 nm. The final protein concentration was calculated using an extinction coefficient of 0.83 for a 0.1% protein solution with a molecular weight of 130 kDa. Myosin-S1 was aliquoted in small portions, snap-freezed and stored – 80 °C for further uses.

The preparation of HMM was performed via limited proteolysis of rabbit skeletal muscle myosin. To initiate the cleavage of the myosin, the myosin solution in myosin buffer (see the Table 3.3 in Materials) was pre-warmed to 25 °C. Digestion was carried out by adding TLCK-treated chymotrypsin to a final concentration of 0.05 mg/mL. The reaction was maintained at a constant temperature of 25 °C for exactly 6.5 minutes. The proteolytic process was terminated by the addition of a 0.5 mM ethanolic solution of PMSF. The reaction mixture was immediately transferred to an ice bath to rapidly lower the temperature. To remove the inhibitor and stabilize the protein fragments, the solution was dialyzed against a buffer containing 40 mM KCl, 10 mM imidazole, pH 7.0, and 1mM DTT. To separate the soluble HMM from the insoluble light meromyosin (LMM) and any remaining undigested myosin, the solution was ultra-centrifugated for 30 minutes at 40,000 rpm, +4 °C, using a Beckman 70 Ti

rotor. The supernatant, containing the purified HMM, was carefully collected for further experimental use. The concentration of the HMM was determined spectrophotometrically by measuring absorbance at 280 nm and 320 nm. To account for light scattering, the absorbance at 320 nm was subtracted from the absorbance at 280 nm. The final protein concentration was calculated using an extinction coefficient of 0.6 for a 0.1% protein solution, assuming a molecular weight for HMM of 350 kDa. HMM was aliquoted in small portions, snap-freezed and stored – 80 °C for further uses.

4.1.3 Preparation of Tn from skeletal muscle

Troponin (Tn) was isolated from rabbit skeletal muscle with the Potter method described in (Potter, 1982). Muscle ether powder was prepared from rabbit skeletal muscle using a detergent-based extraction procedure. Skeletal muscle tissue was carefully cleaned of connective tissue, finely dissected, and homogenized in Triton X–100 solution, using five volumes of buffer relative to the wet weight of the muscle tissue (see Material Table 3.4). The resulting homogenate was centrifuged for 15 minutes at 16,000 rpm at 4 °C. The pellet was transferred to a beaker and resuspended in Triton X–100 solution supplemented with protease inhibitors, using a volume equal to the weight of the muscle homogenate. To enhance solubilization, the suspension was further homogenized using an high shear homogenizer (Silent crusher M, Heidolph Instruments GmbH, Germany). Following homogenization, the suspension was centrifuged for 15 minutes at 16,000 rpm at 4 °C. This cycle of homogenization and centrifugation was repeated eight times. Protease inhibitors (chymostatin, leupeptin, benzamidine, pepstatin, PMSF) were added to the Triton X–100 solution during every second homogenization cycle. Individual cycles differed with respect to homogenization time, which was progressively reduced and shortened to 1 minute in the final cycle, as well as centrifugation speed, which was decreased to 10,000 rpm in the final step. After completion of the extraction cycles, the final pellet was resuspended in pre-cooled 95% ethanol and collected by vacuum filtration on Whatman No. 4 filter paper using a Büchner funnel. This procedure was repeated three times. To further dehydrate the tissue, the pellet was subsequently resuspended in diethyl ether and filtered through Whatman paper; this step was also repeated three times. For final drying, the troponin preparation was spread evenly on filter paper and allowed to air-dry. The dried ether-extracted troponin powder was ground and stored in tightly sealed containers at – 20 °C until further use.

Rabbit skeletal muscle ether powder was weighed and extracted overnight at 4 °C using a 15:1 (v/w) ratio of extraction buffer (Table 3.4). The resulting suspension was centrifuged at 11 000 rpm for 30 minutes at 4 °C, and the supernatant was collected and set aside. The pellet was then resuspended directly in the centrifuge bottles with 1 M KCl at a ratio of 7.5:1 (v/w relative to the starting tissue) and centrifuged again at 11 000 rpm for 30 minutes at 4 °C. The supernatant from this step was combined with the supernatant from the first extraction, while the pellet was discarded. The combined extract was adjusted to pH 4.6 using 7.5% CH_3COOH (sterile-Acetic Acid) to precipitate Tpm. Acid should be added so slowly by pipetting. The precipitated Tpm was collected by centrifugation at 11 000 rpm for 30 min at 4°C. The pH of the supernatant from this centrifugation was then adjusted to 8.0 with sterile 1 M Tris, incubate on ice in the fridge for 1 hour. Then ammonium sulfate was slowly added to reach 40% saturation (243 g per liter) with constant stirring in 1 hour while maintaining the pH between 7.0 and 8.0. The mixture was centrifuged at 11 000 rpm for 15 min at 4°C, and the pellet was discarded. Additional ammonium sulfate (125 g per liter) was then added to the supernatant to reach 60% saturation under the same conditions. After centrifugation, the 40 – 60% ammonium sulfate pellet, containing the crude skeletal troponin fraction, was collected, while the supernatant was discarded. The pellet was resuspended in a minimal volume of dialysis buffer (Table 3.4) and then dialyzed overnight in the fridge at 4°C. The dialyzed troponin fraction was further purified by anion-exchange chromatography on DEAE Sepharose. The sample was applied to the column equilibrated with dialysis buffer containing protease inhibitors to prevent proteolytic degradation during purification. Bound proteins were eluted by increasing ionic strength with elution buffer, and fractions containing troponin were identified by SDS-PAGE and pooled. All steps were carried out at 4 °C.

The concentration of Tn was determined from the absorbance at 280 nm. The molar concentration was calculated using the extinction coefficient of 0.45 for a 0.1% (w/v) protein solution with a molecular weight of 69 kDa (Margossian & Lowey, 1982; Cachia et al., 1985).

4.2 Mutagenesis of *TPM2* DNA coding Tpm2.2

Synthetic DNA containing sequence of codons that translate into human Tpm2.2 sequence (NM_003289.4) was synthesized and codon-optimized for bacterial expression by Shanghai ShineGene Molecular Biotech, Inc. The sequence was extended at the 5'end by Met-Ala-Ser codons to compensate for the lack of acetylation of the recombinant Tpms protein expressed in bacterial cells. This routinely used modification has previously been shown to

restore the native actin-binding affinity of recombinant Tpm (Monteiro et al., 1994). The cDNA was cloned into pET11a vector (Novagen Inc., Madison, WI, USA) between restriction sites *NcoI* and *BamHI* (Śliwinska et al., 2021). The plasmid was used as a template to prepare the mutants: Asp20His (D20H), Glu41Lys (E41K), Glu181Lys (E181K), and Asn202Lys (N202K). Complementary primers were designed using online Primer-X tools (https://www.bioinformatics.org/primerx/). Primer forward sequences for mutagenesis were the following:

D20H: 5' CTGGACAAAGAAAACGCTATCCATCGTGCTGAACAAGCAAGC 3'

E41K: 5' GTTGCAAACAGCTGGAGAAAGAACAGCAGGCACTGC 3'

E181K: 5' GAACTGGAACGCTCAGAAAAACGTGCTGAAGTTGCTG 3'

N202K: 5' GAAAATCGTTACCAAAAACCTGAAATCTCTGGAAGCTCAGG 3'

The reverse sequences were:

D20H: 5' GCTTCTGCTTGTTCAGCACGATGGATAGCGTTTTCTTTGTCCAG 3'

E41K: 5' GCAGTGCCTGCTGTTCTTTCTCCAGCTGTTTGCAAC 3'

E181K: 5' CAGCAACTTCAGCACGTTTTTCTGAGCGTTCCAGTTC 3'

N202K: 5' CCTGAGCTTCCAGAGATTTCAGGTTTTTGGTAACGATTTTC 3'

The mutated codons are underlined.

The forward and reverse primers were synthesized by Eurofins Genomics (Luxembourg). The substitutions were introduced using the QuikChange® II Site-Directed Mutagenesis Kit (Agilent Technologies, Santa Clara, CA, USA) (see Table 4.1). The method employs high-fidelity, Pfu-based PCR to amplify the entire plasmid using a pair of complementary oligonucleotide primers containing the desired mutation (see above).

Table 4.1 Reagents for the PCR reaction mixture.

Reagent	**Volume (µl)**	**Final Concentration**
Template DNA: pET11a	1	50 ng/µl
primer_5' – 3'	1	125 ng/µl
primer_3' – 5'	1	125 ng/µl
dNTP mix	1	2 mM
Reaction buffer	5	10 x
PfuTurbo DNA polymerase	1	2,5 U/µl
ddH_20	4	–

Following thermal cycling (Table 4.2), the parental methylated plasmid DNA was selectively digested with *DpnI*, leaving the newly synthesized, unmethylated mutant plasmid intact.

Table 4.2 PCR thermal profile and number of cycles.

Steps	**Temperature [°C]**	**Time [s]**	**Number of cycles**
Initial denaturation	95	30	1
Denaturation	95	30	18
Primer annealing	55	60	18
Primer extension	68	600	18

The presence of the mutations was verified via double digestion using the restriction endonucleases *NdeI* and *BamHI*. The *NdeI* recognition site is located within the cDNA sequence encoding the N-terminal Met-Ala-Ser extension, while the *BamHI* site is situated at the 3' terminus. The resulting DNA fragments were separated by electrophoresis on a 0.7% agarose gel. Fragment sizes were determined by comparison with the Perfect Plus™ 1 kb and 100 bp DNA molecular weight markers (EURx, Gdańsk, Poland).

Mutant plasmids were transformed into XL-1 blue super competent cells and single colonies were selected after overnight growth. The plasmid was isolated with commercial plasmid isolation kit (GeneMATRIX Plasmid Miniprep DNA Purification Kit, Eurx, Gdańsk, Poland). The mutant plasmids were further transformed into DH5α cells for additional amplification and purification. Mutations were verified by sequencing using T7 promoter primer. Automatic sequencing was outsourced to Eurofins Genomics (Luxembourg).

4.3 Recombinant Tpm2.2 variants expression and purification

To produce the wild type and mutant Tpm2.2, *E. coli* strain BL21(DE3) cells (Novagen, Thermo Scientific™, MA, USA) were transformed with the plasmids isolated from DH5α. Expression and purification of N-terminally extended wild type and mutant Tpm2.2 was done as in (Śliwinska et al., 2021).

The first step in the production of recombinant Tpm was the transformation of BL21(DE3) cells with the pET11a plasmid containing cDNA encoding Tpm2.2 or its mutated variants. For transformation, 1 µL of the appropriate plasmid was added to 20 µL of competent

cells previously thawed on ice and incubated for 5 minutes on ice. The bacterial cells were then subjected to heat shock at 42 °C for 30 seconds. Plasmid uptake was halted by incubation on ice for 2 minutes. Following transformation, the bacteria were recovered in 80 µL of liquid SOC medium (20 mM glucose, 0.5% yeast extract, 0.05% NaCl, 2.5 mM KCl, 10 mM $MgCl_2$, 10 mM $MgSO_4$, 2% peptone) and incubated with shaking (250 rpm) at 37 °C for 1 hour. Subsequently, 50 µL of the liquid culture was plated onto Luria–Bertani (LB) agar (1.2 % agar, 1% NaCl, 1% peptone, 0.5% yeast extract) supplemented with 50 µg/mL ampicillin. The plates were incubated for 16 hours at 37 °C. After incubation, the plates saved at +4 °C till further use. A single colony of transformed BL21(DE3) cells was inoculated into 10 mL of LB broth (1% NaCl, 1% peptone, 0.5% yeast extract) and incubated for 16 hours at 37 °C. An aliquot of 5 mL of the overnight culture was then transferred into 600 mL of LB broth supplemented with 50 µg/mL ampicillin and grown with shaking at 240 rpm, 37 °C. When the culture reached an optical density (OD) of 0.2 – 0.3, measured at λ = 550 nm, Tpm2.2 expression was induced with 0.4 mM isopropyl β-D-1-thiogalactopyranoside (IPTG). Bacteria were grown up to 1.5 OD_{550} and pelleted at 11,000 rpm for 20 minutes at 4 °C. The bacterial pellet was homogenized in lysis buffer (50 mM Tris-HCl pH 7.5, 10 mM EDTA, 20% sucrose, 0.5 mg/mL lysozyme) using Potter homogenizer. Following a one-hour incubation on ice, the suspension underwent two freeze-thaw cycles (at –80 °C, for 10 minutes). To facilitate protein solubilization, the NaCl concentration was adjusted to 0.2 M after the initial thaw and subsequently increased to 1.0 M during the second cycle. The bacterial lysate was sonicated 2 times for 3 minutes in Bandelin sonicator at 60 – 70% power and centrifuged for 1 hour at 40,000 rpm +4 °C. Supernatant was collected and boiled for 4 minutes. After cooling, Tpm2.2 was separated from other proteins by $(NH_4)_2SO_4$, precipitation. $(NH_4)_2SO_4$, was first added to 35% of saturation at 4 °C and the solution was centrifuged for 30 minutes at 30 000 rpm +4 °C, supernatant was collected and $(NH_4)_2SO_4$ was increased to 70% saturation. After centrifugation for 1 hour at 40,000 rpm +4 °C, pellets were collected, resuspended in dialysis buffer (20 mM Tris-HCl pH 7.5, 0.5 mM DTT, 0.02% NaN_3) and dialyzed exhaustively. Tpm2.2 was further purified using Macro-Prep® 25 Q strong anion exchange media in 0 − 0.5 M NaCl gradient using NGC Chromatography system (Bio-Rad, Hercules, California, USA). Purity of the isolated proteins were checked using the SDS-PAGE. The concentration was determined spectrophotometrically using the theoretical molar extinction coefficient 17,880 $M^{-1}cm^{-1}$ calculated by the bioinformatics tool Expasy ProtParam (Expasy is operated by the SIB Swiss Bioinformatics Institute). Protein concentrations were additionally confirmed by the analysis of differential absorption spectra of tyrosine according to (Moraczewska, Nicholson-Flynn, et al., 1999). The assay is based on the

difference in absorbance of tyrosine residues measured under acidic and alkaline conditions. For baseline correction, 450 µL of 6 M guanidine hydrochloride (GuHCl), pH 6.0, was added to the reference cuvette, and 450 µL of 6 M GuHCl, pH 12.0, was added to the measuring cuvette. A blank spectrum was recorded in scan mode between 270 and 320 nm. Subsequently, 50 µL of protein sample was added to each cuvette (final volume 500 µL), mixed thoroughly, and spectra were recorded again in scan mode. The difference in absorbance was calculated by subtracting the absorbance at 275 nm from that at 294 nm to correct for background contributions. Protein concentration was calculated using the molar extinction coefficient of tyrosine (ε = 1480 $M^{-1}.cm^{-1}$ per tyrosine residue, adjusted for the number of tyrosines in the protein) and assuming a 1 cm optical path length. Concentrations were determined from at least two independent measurements and averaged. The proteins were aliquoted and stored at –80 °C for further use.

4.4 Polyacrylamide gel electrophoresis

Protein separation by molecular weight was carried out using polyacrylamide gel electrophoresis (SDS-PAGE). Electrophoresis was carried out in a discontinuous system using either 10%, 12% or 15% resolving gel and a 5% stacking gel (see Table 3.7 in Materials). The running buffer contained 25 mM Tris-HCl, 192 mM glycine, and 0.1% SDS.

Protein samples (5–25 µL) were mixed 1:1 with sample buffer (Laemmli buffer) (see Table 3.7 in Materials) containing SDS and a reducing agent, and denatured by heating at 95 °C for 3 minutes prior to loading onto the gel. Electrophoresis was performed using the Mini-PROTEAN II system (BioRad, Hercules, CA, USA) at a constant voltage of approximately 120 V until complete protein separation was achieved.

Following electrophoresis, polyacrylamide gels were fixed, stained with Coomassie Brilliant Blue G-250 for at least 1 hour, and subsequently distained until clear protein bands were visible. The composition of buffers and staining solutions is provided in Table 3.7.

4.5 Expression and purification of cofilin-2

Recombinant Cof2 was expressed in *E. coli* BL21 (DE3) cells carrying a plasmid encoding mouse Cof2 subcloned into the pGAT2-MM expression vector, designated pPL93 (a gift from Pekka Lappalainen, University of Helsinki). The construct encodes an N-terminal GST tag followed by a thrombin cleavage site. Protein purification was performed using GST-affinity chromatography as described in (Robaszkiewicz et al., 2016).

A single bacterial colony was used to inoculate LB medium supplemented with ampicillin (final concentration 50 µg/mL). Cultures were grown in four 1L flasks containing 600 mL LB medium each and incubated overnight at 28 °C without shaking. The following day, cell density was measured spectrophotometrically at 550 nm, and cultures reached an OD_{550} of approximately 0.4. Protein expression was induced by the addition of IPTG to a final concentration of 0.4 mM, followed by incubation for an additional 4 h at 37 °C with shaking at 250 rpm. After induction, cultures reached an OD_{550} of approximately 1.8. Cells were harvested by centrifugation at 11,000 rpm for 20 minutes. Cell pellets were resuspended in 20 mM Tris-HCl, pH 7.5, centrifuged at 3,000 rpm for 15 minutes, and stored at −80 °C until further processing.

Frozen cell pellets were thawed on ice and resuspended in Buffer A (50 mM Tris-HCl, pH 7.5, 100 mM NaCl). Cells were lysed by sonication on ice using two cycles of 3 minutes total sonication time, with 30 s cooling intervals between pulses, at 50–70% power. Cell debris was removed by centrifugation at 11,000 rpm for 20 minutes at 4 °C using a Beckman 70Ti rotor. The clarified supernatant was retained for affinity purification.

Glutathione-agarose beads (Pierce, Rockford, IL, USA) were washed and equilibrated in Buffer A. The clarified lysate was incubated with calibrated glutathione-agarose beads (1.5 mL beads per pellet equivalent) overnight at 4 °C on a horizontal shaker to allow binding of GST-Cof2. Beads were then collected by centrifugation at 4,000 rpm for 3 minutes at 4 °C and washed multiple times with Buffer A to remove unbound proteins.

After washing, beads were resuspended in Buffer A to a final volume of approximately 4 mL. Human serum thrombin (Sigma-Aldrich, St Louis, MO, USA) was added to a final concentration of 0.9 mg/mL, and the suspension was incubated overnight at 4 °C on a horizontal shaker to cleave Cof2 from the GST tag. Following cleavage, beads were pelleted by centrifugation at 3,000 rpm for 2 minutes at 4 °C, and the supernatant containing cleaved Cof2 was collected.

Protein purity and cleavage efficiency were assessed by SDS-PAGE. After electrophoretic analysis, the Cof2 solution was filtered through a 0.45-µm syringe filter. Protein concentration was determined spectrophotometrically using an absorption coefficient of 0.79 for 0.1% protein solution at 280 nm and a molecular weight of 18,500 Da. Protein samples were stored at –80 °C.

4.6 Expression and purification of tropomodulin 1

Tropomodulin-1 (Tmod1) was expressed in *E. coli* BL21(DE3) cells (Invitrogen, Carlsbad, CA, USA) using the pET21b vector encoding an N-terminal hexahistidine tag which was a kind gift from A. Kostyukova (Voiland School of Chemical Engineering and Bioengineering, University of Washington, Pullman, WA, USA) according to (A. Kostyukova et al., 2000; Moraczewska et al., 2019). Colonies were selected on LB agar plates containing ampicillin (final concentration is 50 µg/mL). Several fresh colonies were used to inoculate starter cultures, which were subsequently expanded into larger LB cultures supplemented with ampicillin. Cells were grown at 37 °C with shaking until mid-log phase ($OD_{550} \approx 0.6$) at which point protein expression was induced by addition of IPTG to a final concentration of 0.4 mM. Cultures were incubated and harvested after several hours ($OD_{550} \approx 1.8$). Cells were collected by centrifugation for 15 minutes at 11,000 rpm +4 °C and resuspended in 20 mM Tris-HCl, pH 7.5, 100 mM NaCl, protease inhibitors, and 1 mM Pefabloc. Cells were sonicated 2 seconds on/8 seconds off, during 5 minutes on ice untill fully destroyed. Homogenate was centrifuged for 30 minutes at 16,000 rpm +4 °C and the presence of Tmod1 in inclusion bodies was confirmed by SDS-PAGE analysis of soluble and insoluble fractions.

Inclusion bodies were resuspended in 50 mM sodium phosphate, pH 7.0, 150 mM NaCl, 10 mM imidazole, pH 7.0, and 6 M urea to solubilize the recombinant protein. After overnight solubilization at 4 °C, insoluble material was removed by centrifugation for 1 hour at 50,000 rpm +4 °C. The clarified supernatant was applied to a column packed with Ni^{2+}-NTA agarose resin equilibrated with the loading buffer (50 mM sodium phosphate, pH 7.0, 150 mM NaCl, 10 mM imidazole, and 6 M urea). The column was washed extensively with the loading buffer and His-tagged Tmod1 was eluted using the loading buffer supplemented with 250 mM imidazole. Eluted fractions were analyzed by SDS-PAGE, and fractions containing Tmod1 were pooled. Pooled fractions were subjected to stepwise dialysis at 4 °C to gradually remove urea and allow protein refolding. Dialysis buffers contained 20 mM Tris-HCl, pH 7.5, 150 mM NaCl, 1 mM EDTA, and 1 mM DTT, with urea concentrations decreasing incrementally until complete removal. Refolded protein was further purified by anion-exchange chromatography using column packed with DE Sepharose® (Cytiva, Germany) resin. The protein was loaded into the column and washed with loading buffer followed by elution with a 0 – 0.6 M NaCl linear gradient. Fractions containing purified Tmod1 were identified by SDS-PAGE, pooled, and dialyzed into final storage buffer containing 20 mM Tris-HCl, pH 8.0, 1 mM EDTA, and 1 mM DTT, overnight. Concentration of the protein was determined by absorbance at 280 nm

using an extinction coefficient 0.1% protein solution (w/v) = 3.95 $mL.mg^{-1}.cm^{-1}$ (equivalent to $\varepsilon_{(280)}$ = 15,930 $M^{-1}cm^{-1}$) and a molecular weight of 40.3 kDa. Pure Tmod1 was aliquoted, snap freezed and stored at –80 °C for further use.

4.7 Fluorescent labeling of G-actin with N-(1-pyrene)iodoacetamide

Actin was fluorescently labeled at Cys374 with a pyrene moiety by incubation of G-actin with N-(1-pyrene)iodoacetamide (PIA) (Sigma-Aldrich, Germany) as described in (Kouyama & Mihashi, 1981; Criddle et al., 1985). G-actin was polymerized to a final concentration of 2 mg/mL in 0.1 M KCl at room temperature for 3 hours with continuous stirring. A 1.4-fold molar excess of PIA was then added slowly to the F-actin solution while stirring, and the reaction mixture was incubated overnight at room temperature with gentle agitation, protected from light. Following incubation, the labeled F-actin was pelleted by ultracentrifugation at 40,000 rpm for 1 hour at 4 °C. The supernatant was discarded, and the pellet was resuspended in 3 mL of G-buffer. To remove residual dimethylformamide (DMF) and unreacted PIA, the suspension was dialyzed extensively against G-buffer with at least three buffer changes, protected from light. The pyrene-labeled G-actin was then clarified by ultracentrifugation at 40,000 rpm for 1 hour at +4 °C.

The pyrene–G-actin was gel filtrated by using with Sephacryl® S-200 HR (Cytiva, Germany) column protected from light. Eluted fractions were checked by SDS-PAGE and clear fractions combined together. Combined fractions was stored on ice and used within two weeks. Protein concentrations and labeling ratios were determined using the following molar extinction coefficients: 26,600 $M^{-1}.cm^{-1}$ at 290 nm for G-actin and 22,000 $M^{-1}.cm^{-1}$ at 344 nm for pyrene.

4.8 Fluorescent labeling of Tpm2.2 with N-(1-pyrene)iodoacetamide

The wild type and mutant Tpm2.2 were fluorescently labeled at Cys36 and Cys190 by incubation with PIA (Sigma-Aldrich, Germany) according to the method described in (Robaszkiewicz et al., 2015). Tpm2.2 was diluted 1:1 (vol:vol) with 8 M guanidine chloride to expose the Cys residues to the solution. A 20-fold molar excess of PIA was added to the Tpm solution. After 4 hours of incubation in the darkness at room temperature, the solution was incubated at +4 °C overnight. The reaction was quenched by 2-fold molar excess of DTT over the labeling dye and the proteins were dialyzed against 0.5 M NaCl, 10 mM Hepes pH 7.6, at +4 °C for 24 hours and then against 30 mM NaCl, 10 mM Hepes pH 7.6, at +4 °C for additional 24 hours. Concentrations of the labeled proteins were determined by SDS-PAGE using wild-

type Tpm2.2 of known concentration for standard curve. Pyrene concentration was determined spectrophotometrically using the molar extinction coefficient as given above. Labeling ratios of different preparations ranged from 173% to 262%. Given two Cys residues in one Tpm2.2 chain, the maximal expected labeling ratios would be 400%, thus the obtained labeling ratios showed that the preparations of labeled Tpm2.2 ranged from 1.7 to 2.6 labels per Tpm2.2 dimer.

4.9 Binding of Tpm2.2 variants to F-actin

Binding of Tpm2.2 variants to F-actin were tested in the absence and presence of Tn by a cosedimentation assay. F-actin was obtained by polymerization of 30 μM G-actin in G-buffer supplemented with 30 mM NaCl and 2 mM $MgCl_2$, and incubated at room temperature for 20 minutes.

For binding of Tpm alone, 30 μM F-actin was diluted to 3 μM with 30 mM NaCl, 2 mM $MgCl_2$, 5 mM imidazole, pH 7.0, 0.5 mM DTT and mixed with either mutant or wild-type Tpm2.2 at concentrations ranging from 0 to 1 μM. Tpm2.2-decorated actin filaments were pelleted at 40,000 rpm, at 20 °C, for 1 hour using a Beckman Coulter Optima™ L-90K ultracentrifuge, rotor type 42.2 Ti. Pellets were suspended in Laemmli buffer (Laemmli, 1970). Proteins present in pellets and supernatants were separated on 12% SDS-PAGE and visualized by Coomassie Blue G-250 staining. F-actin:Tpm2.2 ratios in pellets and unbound Tpm2.2 in supernatants were quantitated densitometrically using Image Lab software version 6.1.0.7 (Bio-Rad, Hercules, CA, USA).

In order to analyze actin binding of Tpm2.2 variants in the presence of Tn ($\pm Ca^{2+}$), F-actin and Tpm2.2 variants were diluted to 5 μM and 1.4 μM, respectively, in 6 mM NaCl, 5 mM $MgCl_2$, 25 mM HEPES, pH 7.5, 1 mM DTT, with either 0.1 mM $CaCl_2$ or 0.2 mM EGTA. Tn complex was added at increasing concentrations ranging from 0 to 3 μM. Proteins were incubated at room temperature for 20 minutes and pelleted at 40,000 rpm in Beckman 40.2 rotor for 1 h at 20 °C. After ultracentrifugation, protein pellets were collected and suspended in Laemmli sample buffer (Laemmli, 1970). Proteins in pellets and supernatants were analyzed on 15% SDS-PAGE. F-actin, Tpm-TnT and TnI bands in pellets and Tpm-TnT bands in supernatants were quantitated densitometrically using ChemiDoc™ MP imaging sytem (BioRad, Hercules, CA, USA) and Image Lab software, version 6.1.0.7 (BioRad, Hercules, CA, USA). F-actin:Tpm-TnT densitometric ratios were calculated and plotted as a function of Tn concentration.

4.10 Binding of Cof2 to F-actin in the absence and presence of the thin filament regulatory proteins

Binding of Cof2 to the F-actin-Tpm complex was assessed by co-sedimentation followed by SDS–PAGE analysis of the pelleted and supernatant fractions. F-actin was obtained by polymerization of 30 μM G-actin in G-buffer supplemented with 100 mM NaCl and 2 mM $MgCl_2$, and incubated at room temperature for 20 minutes. 30 μM F-actin was diluted to 3 μM and mixed with either mutant or wild-type Tpm2.2 at 0.75 μM in 100 mM NaCl, 2 mM $MgCl_2$, 5 mM Tris-HCl, pH 7.5, and 1 mM DTT. Cof2 was added at increasing concentrations ranging from 0 to 5 μM. Proteins were incubated and pelleted as described above (See 4.9). Proteins in pellets and supernatants were analyzed on 12% SDS-PAGE. F-actin, Tpm and Cof2 bands in pellets and Cof2 bands in supernatants were quantitated densitometrically using ChemiDoc™ MP imaging system (BioRad, Hercules, CA, USA) and Image Lab software, version 6.1.0.7 (BioRad, Hercules, CA, USA). Cof2:F-actin and Tpm:F-actin densitometric ratios were calculated and plotted as a function of Cof2 concentration and Cof2:F-actin (vol:vol) ratio, respectively. Cof2:F-actin densitometric ratios were plotted as a function of unbound Cof2 concentration left in the supernatant.

Binding of Cof2 to the F-actin-Tpm-Tn + Ca^{2+} complex was assessed by co-sedimentation followed by SDS–PAGE analysis of the pelleted and supernatant fractions. F-actin was obtained by polymerization of G-actin as described above. 30 μM F-actin was diluted to 3 μM and mixed with either mutant or wild-type Tpm2.2 at 0.75 μM in the presence of Tn at 2.4 molar excess of Tpm concentration and 0.1 mM Ca^{2+} in 100 mM NaCl, 2 mM $MgCl_2$, 5 mM Tris-HCl, pH 7.5, and 1 mM DTT. Cof2 was added at increasing concentrations ranging from 0 to 5 μM. Proteins were incubated and pelleted as described above (See 4.9). Proteins in pellets and supernatants were analyzed on 10% SDS-PAGE. F-actin, Tpm-TnT and Cof2 bands in pellets and Cof2 bands in supernatants were quantitated densitometrically using ChemiDoc™ MP imaging system (BioRad, Hercules, CA, USA) and Image Lab software, version 6.1.0.7 (BioRad, Hercules, CA, USA). Cof2:F-actin and Tpm–TnT: F-actin densitometric ratios were calculated and plotted as a function of Cof2 concentration and Cof2:F-actin (vol:vol) ratio, respectively. Cof2:F-actin densitometric ratios were plotted as a function of unbound Cof2 concentration left in the supernatant.

Binding of Cof2 to F-actin–Tpm complex in the presence of Tmod1 was assessed by co-sedimentation assay as described above, with the following modifications. Tmod1 was included at concentrations of 5, 10, or 50 nM in samples containing 3 μM F-actin and 0.75 μM

Tpm2.2, while Cof2 was added at increasing concentrations ranging from 0 to 5 μM. Pellet and supernatant fractions were resolved by 12% SDS-PAGE. Bands corresponding to F-actin, Tpm, and Cof2 in the pellet fractions, as well as Cof2 in the supernatant fractions, were quantified by densitometry and analyzed as described above.

4.11 Binding of Tmod1 to F-actin

Binding of Tmod1 to the pointed end of the F-actin-Tpm and F-actin-Tpm-Tn + Ca^{2+} complexes with their barbed-end capped with CapZ was assessed by co-sedimentation followed by SDS–PAGE analysis of the pelleted fractions and subsequent detection of Tmod1 by Western blot. The assay was performed essentially as described previously (Colpan et al., 2016; Moraczewska et al., 2019). G-actin at 20 μM was polymerized in G-buffer with 100 mM KCl, 2 mM $MgCl_2$, in the presence of 0.14 μM CapZ, for one hour at room temperature and then diluted 4-times in 1x assay buffer which contained 5 mM Tris-HCl, pH 7.6, 100 mM KCl, 2 mM $MgCl_2$, 0.2 mM ATP, 0.5 DTT with either 2 μM Tpm or 2 μM Tpm together with 4 μM Tn, and 1 mM $CaCl_2$, final concentrations. Tmod1 was added at a final concentration of 10 nM, incubated at room temperature for 20 minutes and then mixtures were spun down at 40,000 rpm at + 20 °C. Pellets were dissolved in G-buffer and separated either on 12% SDS-PAGE or 12% TGX Stain-Free gels (Bio-Rad, Hercules, CA, USA). Separated proteins were transferred to PVDF membrane using Trans-Blot Turbo transfer system (Bio-Rad, Hercules, CA, USA). Membranes were blocked 1 hour in Every Blot blocking buffer (Bio-Rad, Hercules, CA, USA) and Tmod1 was detected using a primary rabbit polyclonal anti-Tmod1 antibody (Abcam, Cambridge, UK). A peroxidase-conjugated AffiniPure goat anti-rabbit IgG (H+L) secondary antibody (Bio-Rad, Hercules, CA, USA) was used. Chemiluminescence signal was detected with the Clarity Max ECL Western Blotting Substrate (Bio-Rad, Hercules, CA, USA). Images of the SDS–PAGE gels and developed blots were acquired using a Molecular Imager ChemiDoc XRS+ system (Bio-Rad, Hercules, CA, USA). Densitometric analysis of the protein bands was performed using Image Lab software (Bio-Rad, Hercules, CA, USA).

4.12 Measurements of the actomyosin ATPase activity

ATPase measurements were performed in 96-well plates at 25 °C using the NADH-coupled assay according to (Franz et al., 2021). The NADH-coupled ATPase assay is based on coupling ATP hydrolysis to NADH oxidation via the enzymatic activities of pyruvate kinase and lactate dehydrogenase, enabling quantitative measurement of ATPase activity by monitoring the decrease in NADH absorbance at 340 nm (see Figure 4.1). 5 μM F-actin and

Tpm2.2 variants added at concentrations ranging from 0 to 5.6 µM were preincubated at room temperature in the ATPase buffer (25 mM HEPES pH 7.3, 25 mM KCl, 5 mM $MgCl_2$ and 1 mM DTT) for 30 minutes. Reactions were started by the addition of 0.3 µM S1, 2 mM ATP, 0.4 mM NADH, 1 mM phosphoenol-pyruvate (PEP), 10 U/ml lactate dehydrogenase and 20 U/ml pyruvate kinase (final concentrations). Time courses of the reactions were monitored at 340 nm using a Synergy4 microplate reader (Bio-Tek, Winooski, Vermont, USA). Data were analyzed using the OriginPro® software (Northampton, MA, USA) and fit to the Hill-Langmuir-equation:

$$ATPase\ rate = Start + (End - Start) \cdot \frac{[Tpm]^n}{IC_{50}{}^n + [Tpm]^n} \qquad \text{Equation 1}$$

where "*Start"* reflects the actin-activated S1 ATPase activity in the absence of Tpm2.2, "*End*" represents the actin-activated S1 ATPase activity at saturating concentrations of Tpm2.2, "[*Tpm*]" is the tropomyosin concentration, "*n*" defines the Hill coefficient and "IC_{50}" defines the concentration of Tpm required for half-maximal inhibition of the ATPase activity.

For temperature-dependence measurements, actin-activated myosin ATPase activity was assessed in 96-well plates at controlled temperatures ranging from 22 °C to 40 °C using the NADH-coupled assay. F-actin was diluted to a final concentration of 5 µM in ATPase buffer and pre-incubated for 20 minutes at room temperature with 0.714 µM Tpm2.2 variants and 1.071 µM Tn. The reaction was started by the addition of 0.3 µM S1, 2 mM ATP, 0.6 mM NADH, 1.5 mM phosphoenol-pyruvate (PEP), 28 U/ml lactate dehydrogenase and 20 U/ml pyruvate kinase (final concentrations). Time courses of the reactions were monitored and data analyzed as described above. To calculate the activation energy values (E_a) Arrhenius equation was used:

$$ln(k) = ln(A) - \frac{E_a}{R} \cdot \frac{1}{T} \qquad \text{Equation 2}$$

where *ln(k)* is the natural logarithm of the measured actomyosin ATPase activity, *ln(A)* is the natural logarithm of the pre-exponential factor, *R* is the universal gas constant (8.314 J $mol^{-1}K^{-1}$) and *T* is the absolute temperature expressed in Kelvin.

Dependence of the ATPase activity on Tn concentration was analyzed at the following protein concentrations in ATPase buffer (25 mM HEPES pH 7.3, 25 mM KCl, 5 mM $MgCl_2$ and 1 mM DTT): 5 µM actin, 0.714 µM Tpm, 1.0 µM S1, 0–2 µM Tn. Reaction mixtures included 2 mM ATP, 0.6 mM NADH, 28 U/mL lactate dehydrogenase (LDH), and 20 U/mL pyruvate kinase (PK). Time courses of the reactions were monitored and data analyzed as described above.

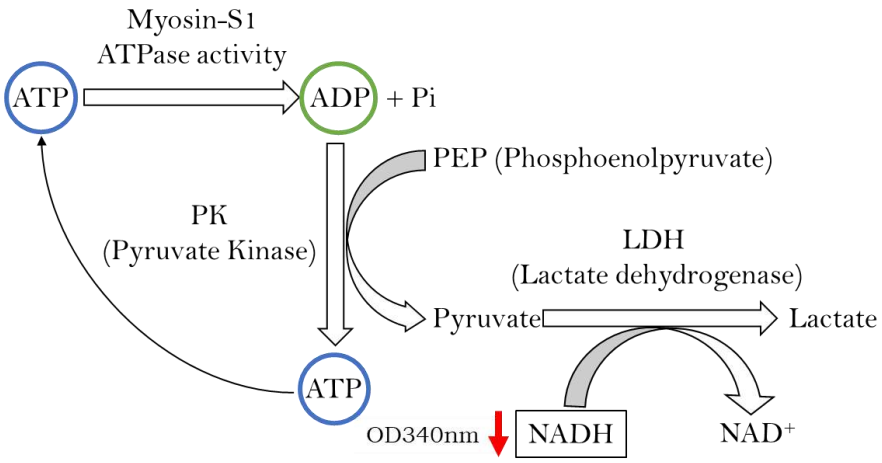

Figure 4.1 Schematic illustration of NADH-coupled assay work flow. For details see the text.

Tpm-Tn-dependent regulation of actin-activated myosin S1 ATPase activity and Ca^{2+} sensitivity were analyzed at 23–25°C via a colorimetric molybdenum blue assay with ferrous sulfate as a reducing agent (Feuer & Molnar, 1948; Śliwinska et al., 2021) in a 96-well plate reader (iMark, Bio-Rad). To analyze regulation of the ATPase at increasing Tpm-Tn concentrations, reaction mixtures (5 µM F-actin, 1 µM myosin S1, 0–1.4 µM wild-type/mutant Tpm2.2, and Tn at a 1:2 Tpm:Tn ratio) were tested in 30 mM NaCl, 2 mM $MgCl_2$, 5 mM imidazole (pH 7.0), 1 mM DTT, and either 0.1 mM $CaCl_2$ or 0.2 mM EGTA. The ATPase was initiated with 3 mM MgATP and stopped with SDS/EDTA after 6 minutes. Inorganic phosphate was quantified colorimetrically at 750 nm (iMark, Bio-Rad). Data were normalized at each Tpm-Tn concentration to unregulated acto-S1 ATPase activity. In the presence of Ca^{2+} the experimental data were fitted in SigmaPlot 12.5 to a hyperbolic equation:

$$y = y^0 + \frac{ax}{b+x} \qquad \text{Equation 3}$$

where x is Tpm concentration, y^0 is the minimal ATPase activity (in the absence of Tpm), a is the maximal ATPase activity, and b is the [Tpm] required for 50% of activation (EC_{50}^{act}).

In the absence of Ca^{2+} (EGTA), the experimental data were fitted to Eq. 1, where x – Tpm concentration, y^0 – the predicted minimum ATPase activity (at saturating Tpm concentration), a – difference between maximum and minimum ATPase activity, and b – [Tpm] required for 50% of inhibition (EC_{50}^{inh}).

The Ca^{2+}-sensitivity was measured at the following protein concentrations: 5 µM actin, 1 µM Tpm, 2 µM Tn and 1 µM S1. Ca^{2+} concentrations were varied from 1 x 10^{-10} to 1 x 10^{-3} M by adjusting Ca^{2+}/EGTA ratio to obtain the desired free Ca^{2+} levels, as previously described by (Śliwinska et al., 2021). The precise amounts of Ca^{2+} and EGTA were calculated using the

PyChelator web tool (https://amrutelab.github.io/PyChelator/) with ionic strength determined using an online ionic strength calculator (http://calistry.org/calculate/ionic-strength-calculator). The calculated Ca^{2+}/EGTA ratios were then used to prepare solutions containing exact [Ca^{2+}] (see Table 3.13 in Materials).

4.13 Single turnover measurements of myosin-actin interactions

Single turnover experiments were performed in the assay buffer (25 mM Hepes, pH 7.3, 25 mM KCl, 5 mM $MgCl_2$ and 0.5 mM DTT) at 25 °C as described (Franz et al., 2021). To measure the very fast, millisecond initial rates, the Hi-tech Scientific SF61 double mixing stopped-flow system (TgK Scientific Limited, Bradford on Avon, UK) (see Figure 4.2) was used.

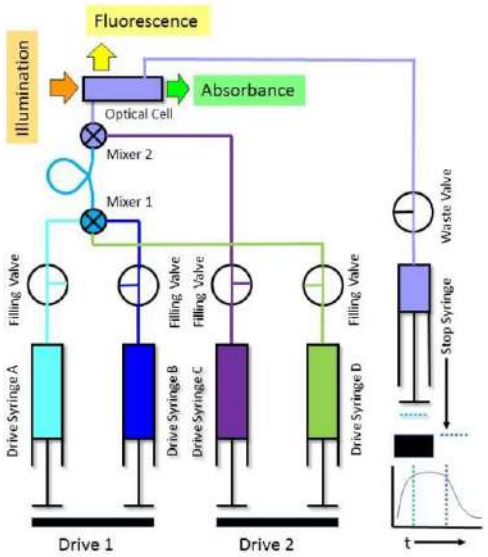

Figure 4.2 Schematic illustration of stopped-flow system. In the present experiments, the syringes mounted in drive 2 were not used. (https://www.hi-techsci.com).

To determine acto-myosin dissociation kinetics, time traces of pyrene fluorescence were recorded following rapid mixing in a stopped-flow apparatus at 25 °C in the assay buffer. Syringe-A contained 0.5 μM S1, 0.5 μM pyrene-labeled F-actin, and 2 μM Tpm2.2, while syringe-B contained 0.4 μM ATP. Upon rapid mixing, ATP-induced dissociation of S1 from pyrene actin was detected as an increase in pyrene fluorescence. The time-dependent fluorescence changes were recorded and analyzed to determine the kinetic parameters associated with ATP binding and acto–myosin complex dissociation.

To monitor individual ATP hydrolysis events under conditions where myosin heads were allowed to hydrolyze only one ATP molecule, myosin was preincubated with Tpm2.2 decorated F-actin, and the reaction was initiated by rapid mixing with fluorescently labeled

mant-ATP using a stopped-flow apparatus at 25 °C in the assay buffer. Syringe-A was filled with 1 µM S1, 3 µM F-Actin and 5 µM Tpm2.2 and syringe-B was filled with 0.8 µM mantATP. The time-dependent changes in fluorescence was recorded to resolve kinetic transitions associated with ATP binding, hydrolysis, phosphate (P_i) release, and ADP dissociation.

4.14 *In vitro* motility assay

In vitro motility assay was used to analyze actin filament sliding velocities and the functional effects of nucleotide-dependent conformational changes in myosin on force generation and actomyosin communication. Experiments were performed as described in (Franz et al., 2021). To obtain fluorescently labeled actin filaments, 2 µM F-actin was incubated on ice with 1.5 molar excess of tetramethyl rhodamine isothiocyanate (TRITC)-phalloidin in assay buffer (25 mM MOPS pH 7.4, 25 mM KCl, 4 mM $MgCl_2$, 1 mM EGTA, and 1 mM DTT). In this labeling method, the fluorescent TRITC remains conjugated to phalloidin, which tightly binds between actin subunits in F-actin. .

Tpm2.2-decorated actin filaments were prepared by incubating 10 nM TRITC- F-actin with 5 µM Tpm2.2 on ice for 1 h. In the experiments where Ca^{2+}-dependent activation was analyzed, 0.5 µM TRITC- F-actin was incubated with 1 µM Tpm2.2 variants and 1 µM Tn on ice.

Purified HMM at a concentration of 0.1 mg/ml was immobilized on nitrocellulose-coated coverslips and blocked with 1% (w/v) BSA in assay buffer before the addition of either undecorated or Tpm2.2-decorated TRITC-F-actin, respectively (see illustration in Figure 4.3). For assays using TRITC-F-actin-Tpm2.2-Tn complexes, pre-made 100 nM regulated filaments were diluted to 10 nM in the assay buffer supplemented with 0.05 % (w/v) BSA. The motility reaction was initiated by introducing assay buffer supplemented with 0.05 % (w/v) BSA, 2 mM ATP, 0.4 % (w/v) methylcellulose, 30 mM glucose, 250 U/ml catalase, 25 U/ml glucose oxidase.

For each condition, 100 images with a frame rate of 10 per second were recorded using an Olympus IX83 inverted microscope. Videos were analyzed using the automated tracking software DiaTrack3.05 (Vallotton et al., 2017). Average sliding velocities were obtained from Gaussian fits to the velocity distributions using the OriginPro® software (Northampton, MA, USA).

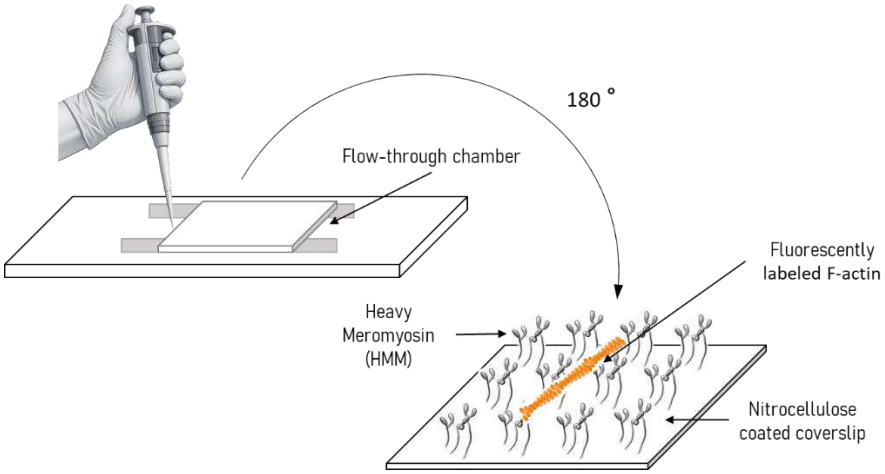

Figure 4.3 Schematic illustration of *in vitro* motility assay. This illustration was created in PowerPoint with the help of artificial intelligence model (ChatGPT).

4.15 Förster Resonance Energy Transfer (FRET) measurements

Fluorescence measurements were conducted using a FluoroMax-4 (HORIBA Jobin Yvon, Kyoto, Japan) spectrofluorometer. All experiments were carried out under gentle stirring, with the sample contained in a 4 x 10 mm Hellma cuvette thermostated via a circulating water bath (ThermoScientific A25 and AC200, respectively) to maintain a constant temperature of 20.0 ± 0.3 °C. The excitation and emission slit widths were adjusted such that the detected photon count rate did not exceed 1.0 x 10^6 counts per second.

Förster Resonance Energy Transfer (FRET) was employed to quantify the kinetics of Tpm2.2 binding to actin. The four tryptophan residues located within actin subdomain 1 served as fluorescence donors, while pyrene-labeled Cys36 and Cys190 of Tpm2.2 acted as acceptors (Figure 4.4).

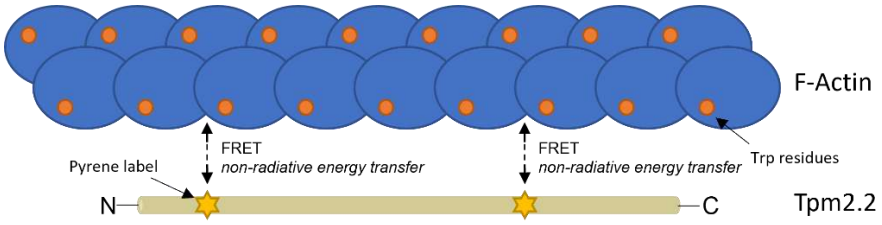

Figure 4.4 Schematic representation of the FRET mechanism between F-actin and pyrene-labeled Tpm2.2, illustrating the proximity-dependent energy transfer between pyrenes and Trp residues.

Donor and acceptor species were rapidly mixed in assay buffer (10 mM HEPES, pH 7.6, 30 mM NaCl, 2 mM $MgCl_2$) to final concentrations of 2 µM of F-actin and 0.2 µM of Tpm2.2. The cluster of Trp residues are located close to the pyrene-labeled Tpm2.2 acceptors, therefore a non-radiative energy transfer is observed as a broad excimer peak of fluorescence

between 450 and 550 nm. Because the pyrene labels are located close to the mutation sites, variations in FRET efficiency can be interpreted as a direct readout of mutation-induced changes in the binding geometry of Tpm2.2 on actin filaments.

Fluorescence traces were normalized to the initial donor intensity (prior to FRET) and subsequently fitted to a single-exponential decay function:

$$F(t) = ae^{-bt} + c \quad \text{Equation 4}$$

where a is the amplitude, b the rate of fluorescence decay (s^{-1}), and c the horizontal asymptote.

FRET efficiencies were calculated from the equation:

$$E = 1 - \frac{F_{DA}}{F_D} \quad \text{Equation 5}$$

where F_D is the Trp fluorescence intensity of F-actin in the absence of Tpm2.2 and F_{DA} is the Trp fluorescence intensity of F-actin in the presence of Tpm2.2.

4.16 Analysis of pyrene-labelled Tpm2.2 excimer fluorescence

Excimer fluorescence of pyrene-labeled Tpm2.2 was measured over a range of myosin S1 concentrations using a FluoroMax-4 (HORIBA Jobin Yvon, Kyoto, Japan) spectrofluorometer. The F-actin-Tpm complex was reconstituted by incubating 2 μM actin with 0.2 μM Tpm2.2 in assay buffer (10 mM HEPES, pH 7.6, 30 mM NaCl, 2 mM $MgCl_2$) at room temperature for at least 15 minutes to ensure complex formation and stabilization of the fluorescence signal. Aliquots of myosin S1 were then added to the preassembled F-actin–Tpm2.2 complex to achieve final S1 concentrations between 0 and 1.5 μM (Figure 4.5).

Because Tpm chains are folded in-register, cysteine residues are symmetry-equivalent. Therefore, pyrene rings attached to Cys on both chains can interact with each other to produce excimer fluorescence. This signal serves as a highly sensitive probe for the conformational state and orientation of Tpm while associated with the actin filament (Y. Ishii & Lehrer, 1990).

Fluorescence was excited at 340 nm, and the excimer emission was monitored at 485 nm using a 15-second integration time followed by a 15-second interval during which the UV xenon flash lamp was switched off to minimize photobleaching. To maintain consistent optical geometry, the cuvette was untouched during the experiment. Final fluorescence curves were corrected for dilution (≤3.8%) and represent the average of 3-4 independently recorded series. Because each mutant originated from separate purification batches with varying pyrene-labeling efficiencies, the curves were normalized according to the asymptotic values of their clearly defined plateaus.

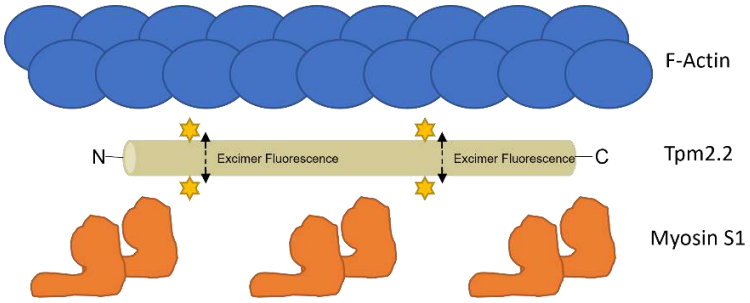

Figure 4.5 Schematic illustration of the assay used to measure excimer fluorescence of pyrene-labeled Tpm2.2 induced by myosin S1.

The resulting normalized data were fitted in SigmaPlot 12.0 using the following equation:

$$y = \frac{F[S1]^n K^n}{1+[S1]^n K^n} \qquad \text{Equation 6}$$

where F is the normalized fluorescence change, [S1] is S1/actin molar ratio, K is the 1/[S1] required for 50% maximal change of the excimer fluorescence, and n is the cooperativity coefficient.

4.17 Measurement of Tpm–Tn interactions using an indirect ELISA assay

Indirect Enzyme Linked Immunosorbent Assay (ELISA) was used to determine interactions between Tpm and Tn in the absence of F-actin (See illustration in Figure 4.6). For this, 96-well Corning® High Bind 96-well EIA/RIA clear flat-bottom microplates (Corning, NY, USA) were coated with skeletal muscle Tn complex by adding 0.2 µg of Tn in assay buffer (25 mM MOPS, pH 7.4, 25 mM KCl, 5 mM $MgCl_2$, 1 mM EGTA, and 10 mM DTT) to each well followed by incubation overnight at 4 °C. After incubation, the Tn solution was removed, and wells were washed three times with phosphate-buffered saline containing 0.05% Tween-20 (PBS-T) to eliminate unbound protein. All subsequent incubation and washing steps were performed at room temperature (23 – 25 °C). Wells were blocked with 5% BSA in PBS-T for 1 hour to minimize nonspecific protein binding, followed by three washes with PBS-T. Tpm2.2 variants, diluted to 100 – 4 ng per well in assay buffer, were added to the wells and incubated for 2 hours. Equivalent amounts of BSA were included as a negative control. After removing the protein solutions, the wells were washed three times with PBS-T. Following the manufacturer's recommendations, the TPM2 rabbit polyclonal primary antibody (Proteintech, Manchester, England) was diluted 1:330 in blocking buffer, and 100 µL of the diluted antibody was added to each well. After a 2-hour incubation, the antibody solution was discarded, and the wells were washed three times with PBS-T. Next, 100 µL of goat anti-rabbit secondary antibody conjugated to horseradish peroxidase (ThermoScientific, MA, USA), diluted 1:500 in blocking buffer according to the manufacturer's instructions, was added to each well and incubated for 1 hour. The antibody solution was then removed, and the wells were washed three times with

PBS-T. Following the washes, 100 µL of TMB Peroxidase EIA Substrate solution (Bio-Rad, Hercules, CA, USA) was added to each well. After a 5-minute incubation, absorbance was measured at 655 nm (Abs^{655}) using an iMark™ microplate reader (Bio-Rad, Hercules, CA, USA).

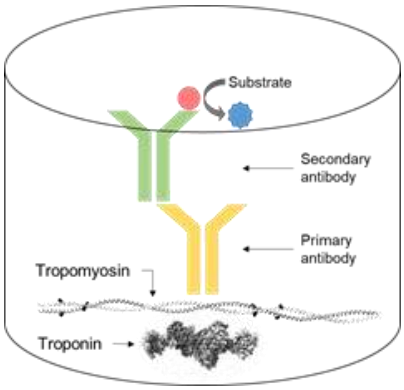

Figure 4.6 Schematic illustration of indirect ELISA assay.

The averaged experimental data points were fitted to the Hill equation using SigmaPlot 12.0:

$$Abs^{655} = \frac{Abs_{max}^{655}[Tpm]^n}{K^n+[Tpm]^n} \qquad \text{Equation 7}$$

where Abs^{655} is the absorbance at 655 nm, Abs_{max}^{655} is the maximum absorbance, [Tpm] is the amount of Tpm/well in nanogram, K is [Tpm] at 50% Abs_{max}^{655}, and n is the Hill coefficient.

4.18 Analysis of actin polymerization kinetics using fluorescence of pyrene-labelled actin

Actin polymerization kinetics was monitored by measuring the increase in fluorescence of pyrene-labeled actin upon filament formation according to (Moraczewska et al., 2004). Prior to use, G-actin was ultracentrifuged at 40 000 rpm in 40.2 Ti Beckman rotor for 1 h in order to remove protein aggregates.

Actin polymerization was monitored by the increase in fluorescence of 5 µM G-actin containing 5% of pyrene-labeled actin. Actin in G-buffer was polymerized by 100 mM KCl and 2 mM $MgCl_2$ either in the absence or presence of 2 µM Tpm2.2 variants. The assay was conducted in a 96-well black microplates (Nunc™ F96 MicroWell™ black polystyrene plate, Thermo Fisher Scientific, USA) at 20 °C. Pyrene fluorescence excited at 366 nm was followed at 387 nm emission wavelength for 90 minutes in a Jasco FP-8350 Spectrofluorometer (Tokyo, JAPAN) equipped with a plate reader.

Fluorescence was measured using the following instrumental settings: response time 20 milliseconds, sensitivity set to high, cycle interval 0.2 minutes, total acquisition time 60 minutes, excitation bandwidth 5 nm, and emission bandwidth 5 nm. The increase in pyrene fluorescence intensity was a measure of actin filament formation. For data analysis, fluorescence traces were baseline-subtracted using the initial data points and fitted to a Hill equation to determine the maximal velocity (V_{max}). All data points were subsequently normalized to the calculated V_{max} to obtain fractional activity. Non-linear regression analysis of the normalized datasets was then performed to determine the apparent half-maximal constant ($K_{0.5}$) and the Hill coefficient (n).

4.19 Assessment of Tpm2.2 and Cof2-mediated regulation of actin filament length, severing and depolymerization

To visualize actin dynamics, G-actin was site-specifically labeled at Gln41 with tetramethyl-rhodamine cadaverine (TRC) (Zedira, Darmstadt, Germany) using bacterial transglutaminase, following the protocol established by (Ngo et al., 2016). Briefly, 0.04 mg/mL transglutaminase, 36 μM TRC and 24 μM G-actin (1.5:1 TRC to G-actin molar ratio) were mixed and incubated overnight on ice. Than TRC-G actin was polymerized by overnight incubation with 25 mM KCl, 4 mM $MgCl_2$ and used within one week. TRC-labeled 480 nM F-actin was incubated overnight on ice with either 160 nM Tpm2.2 variants or a regulatory complex consisting of 240 nM Tn and 10 nM Tmod1 in assay buffer (25 mM MOPS pH 7.4, 25 mM KCl, 4 mM $MgCl_2$, 1 mM EGTA, and 1 mM DTT with 0.05 % (w/v) BSA).

To analyze the impact of Tpm2.2 and Cof2 on actin stability, TRC-labeled filaments were visualized using an Olympus IX83 microscope (100 x magnification) in flow cells coated with positively charged lipids (Figure 4.7 A). Flow cells were blocked with 10 mg/mL BSA. TRC-actin filaments at 240 nM were introduced, followed by the addition of 80 nM Tpm variants, either alone or in the presence of 120 nM Tn, 5 nM Tmod1, or both 120 nM Tn and 5 nM Tmod1. Unbound filaments were removed by washing the cells with an assay buffer supplemented with an oxygen-scavenging system (3 mg/mL glucose, 0.1 mg/mL glucose oxidase, and 0.01 mg/mL catalase). Depolymerization was initiated by the introduction of 240 nM Cof2.

To evaluate how Tpm2.2 variants influence filament length during actomyosin interactions, flow cells were coated with HMM (Figure 4.7 B). Purified HMM at 0.1 mg/mL was immobilized on nitrocellulose-coated coverslips and passivated with 1% (w/v) BSA. A

flow-cell was then assembled by attaching the HMM-coated coverslip to a glass slide using parafilm. Labeled 480 nM TRC-F-actin as described above was incubated overnight on ice either alone or with 160 nM Tpm2.2 variants, in the absence or presence of 240 nM Tn, 10 nM Tmod1, or both 240 nM Tn and 10 nM Tmod1 in assay buffer (25 mM MOPS pH 7.4, 25 mM KCl, 4 mM $MgCl_2$, 1 mM EGTA, and 1 mM DTT with 0.05 % (w/v) BSA). Non-regulated or regulated TRC-labeled F-actin was diluted 4.8-fold and introduced into the flow cell. Interactions were triggered by adding the assay buffer containing 2 mM ATP and 0.4% (w/v) methylcellulose to maintain filaments near the surface, along with an enzymatic oxygen scavenger. Snapshots were taken prior to ATP addition. Upon adding ATP, frames were recorded for 30 seconds to capture filament behavior before, during, and after interaction.

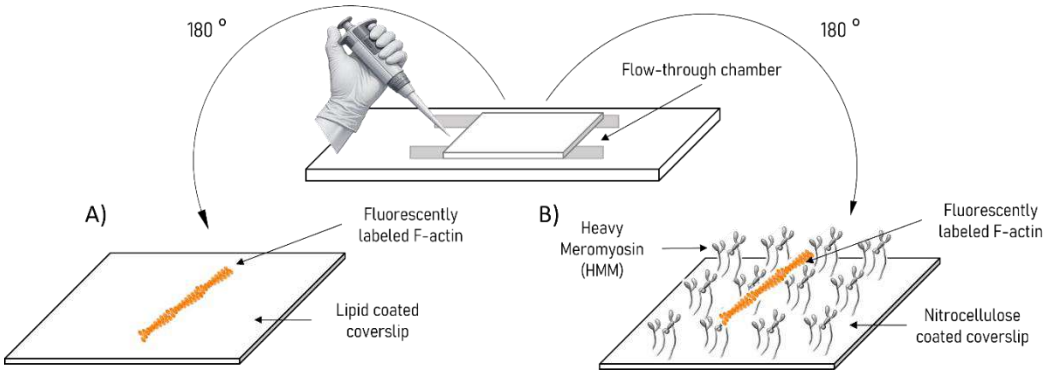

Figure 4.7 Schematic illustration of chambers used in fluorescence microscopy assay. This illustration was created in PowerPoint with the help of artificial intelligence model (ChatGPT).

The frames from both observations were analyzed using FIJI (ImageJ) software. The average filament length was calculated from all filaments captured across 3 to 4 independent experimental repeats.

5 Results

The aims of the thesis were executed using an array of *in vitro* assays. The point mutations selected for this work were introduced in *TPM2* gene via site-directed mutagenesis and the resulting proteins were expressed in bacteria. Thin filaments were reconstructed using proteins purified from muscle tissue and recombinant proteins, which allowed full control of the protein composition in each assay, enabling the functional effects of the mutations to be characterized.

5.1 Rationale for selecting the amino acid substitutions in Tpm2.2 molecule

To address the goals, four *TPM2* mutations were carefully selected (Figure 5.1 A) from the Tpm2.2 variants previously reported as pathogenic. Among the selected substitutions, D20H (1st-half of actin-binding period P1) and E181K (1st-half of actin-binding period P5), are associated with a hypercontractile phenotype (Quijano-Roy et al., 2012; Beck et al., 2013), while E41K (2nd-half of P1) and N202K (2nd-half of P5) are linked to hypocontractility(Tajsharghi, Ohlsson, et al., 2007; Ohlsson et al., 2008). All substitutions occur at the "f" position of the heptad repeat, placing them on the outer surface of the coiled coil, where they are potentially accessible for interactions with other components of the thin filament.

Periods P1 and P5 were chosen specifically because they engage distinct elements of the Tn complex: P1 lies within the region implicated in binding the mobile TnT tail, whereas P5 lies within the central segment of Tpm that contacts the core domain of the Tn complex (TnT2–TnI–TnC) (Figure 5.1 B). By selecting these specific naturally occurring substitutions in Tpm, where the associated disease phenotypes overlap with Tn interaction sites, we can ask whether the direction of the functional defects caused by mutations is dictated by the position of the substitution in the 1st- and/or 2nd- half, or whether Tpm periods that interact with distinct Tn subunits modulate the mechanism or the extent of the functional defect.

Tpm binds Tmod primarily through its N-terminal region, which is exposed at the pointed end of the actin filament (Figure 5.1 C). To date, the precise nature of the interactions between the N-terminal region of Tpm2.2 and Tmod has not been determined. However, in low-molecular-weight non-muscle Tpms, residues 7–14 of the N-terminal region were identified as important for Tmod binding (Vera et al., 2000). More recent structural studies have shown that Tmod adopts a hairpin-like conformation that covers the first 19 residues of the non-

muscle Tpm N-terminus (Tolkatchev et al., 2021). Because the recently resolved model of Tmod1 bound to the pointed end of an actin filament decorated with skeletal Tpm resembles the binding mode observed for non-muscle Tpm (Carman et al., 2023), it is possible that the D20H substitution affects these interactions. In addition, an intact N-terminal coiled-coil structure is required for efficient Tmod binding and pointed-end capping (Fowler et al., 2003; A. S. Kostyukova & Hitchcock-DeGregori, 2004; Colpan et al., 2013). Therefore, both the D20H and E41K substitutions may exert allosteric effects by propagating mutation-induced conformational changes from their respective sites to the Tmod-binding region of Tpm.

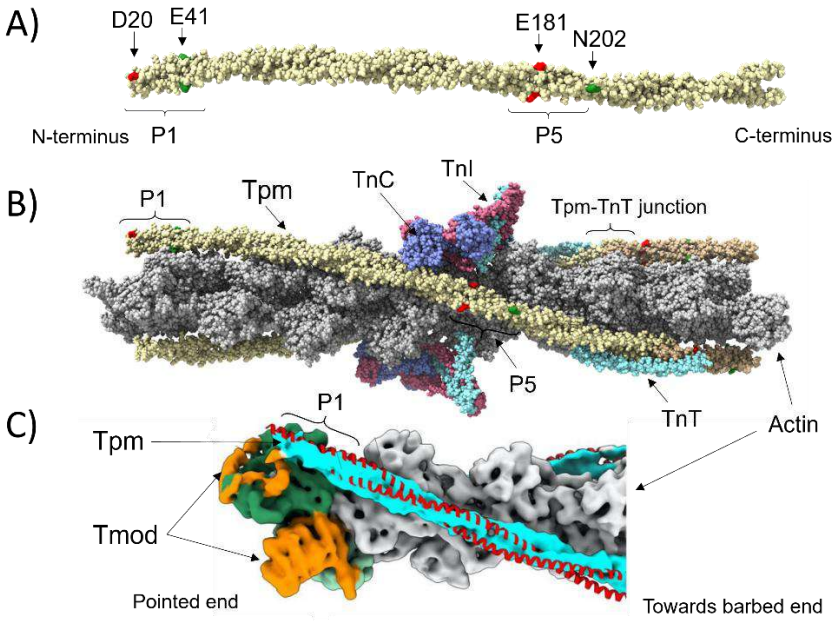

Figure 5.1 Localization of myopathy-associated mutations in actin-binding periods P1 and P5 of Tpm (A) in relation to Tn complex bound to actin filament (B). Because the atomic models of the thin filament containing Tpm2.2 is not available, the thin filament illustrating Tn core domain and the Tpm–TnT junction region was visualized using the cardiac thin filament containing Tpm1.1 and cardiac Tn complex *(*PDB: 7UTI*)*. Actin subunits are colored silver, Tpm chains yellow and gold, TnT turquoise, TnC light blue, and TnI violet. Structural models were generated and visualized using UCSF ChimeraX (Meng et al., 2023). (C) Tmod-capped pointed end of an F-actin filament decorated with Tpm. Actin subunits are shown in grey, light green, and dark green; Tpm chains are shown in red; and Tmod is shown in orange. from (Carman et al., 2023) with permission from *Science*.

In contrast, no comparably direct binding site in Tpm sequence has been defined for cofilin. Cofilin and Tpm bind to overlapping or mutually influencing regions on F-actin, such that Tpm decoration commonly reduces cofilin binding cooperativity and attenuates cofilin-mediated filament severing and depolymerization (P. Gunning et al., 2008; Robaszkiewicz et al., 2020). Therefore, structural perturbations in both P1 and P5 can potentially affect regulation of cofilin binding and activities.

5.2 Introduction of myopathy-linked mutations in *TPM2*

Because isolation of Tpm2.2 from human cells in quantities sufficient for biochemical studies is not possible, wild-type Tpm2.2 and its variants were produced using a bacterial expression system. Single-point mutations were introduced into a plasmid carrying cDNA encoding human Tpm2.2 (NM_003289.4), adapted for bacterial expression. The plasmid was prepared by dr Siatkowska (Śliwinska et al., 2021) and is available in the Department of Biochemistry and Cell Biology, Kazimierz Wielki University. Site-directed mutagenesis was performed as described in Methods section 4.2. To check whether introduction of the desired mutation was successful, the linear DNA obtained in the PCR reaction was amplified and circularized in XL1-Blue cells. Single colonies were selected for DNA isolation. First, the isolated plasmids were checked for serious deletions that might have occurred during the mutagenesis. Restriction analysis illustrated Figure 5.2 revealed that plasmid digestion with either *NdeI* or *BamHI* restriction enzymes produced linear DNA with the expected length of approximately 7 kbp. DNA digestion with both enzymes released a fragment of about 800-900 bp, which is close to the theoretical length of the protein-coding insert (861 bp).

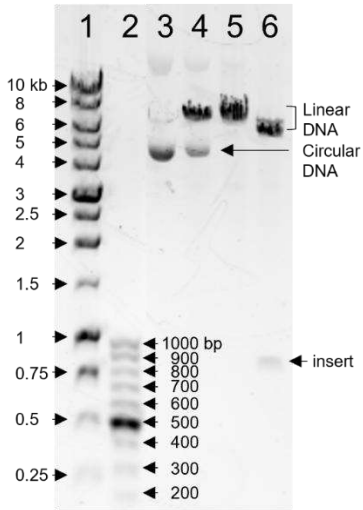

Figure 5.2 Agarose gel electrophoresis of pET11a-*TPM2* plasmid DNA digested with *NdeI* and *BamHI* restriction enzymes. Lanes: 1 & 2 – DNA ladders (10 kb – 250 bp and 1 kb –100 bp), 3 – whole (undigested) plasmid, 4 – DNA cut with *NdeI*, 5 – DNA cut with *BamHI*, 6 – DNA cut with both *NdeI* and *BamHI*, showing the released gene fragment. Arrow points to the DNA fragment (insert) corresponding the *TPM2* coding sequence.

Next, plasmids isolated form XL1-Blue cells were transformed into DH5α cells for amplification. Missense mutations were verified via automated sequencing (outsourced to Eurofins Genomics, Luxembourg) utilizing a T7 promoter primer. Aligning the sequencing tracks against the reference sequence of human Tpm2.2 (NM_003289.4) using Nucleotide BLAST (NCBI, Blast online tool) is shown in Table 5.1.

Table 5.1 Nucleotide Blast for *TPM2* variants. Changes in codons are highlighted in red.

Variants	Substituted part of *TPM2* nucleotide sequence
Tpm2.2-D20H (GAC->CAT)	Query 1 ATGGACGCTATCAAAAAGAAGATGCAGATGCTGAAACTGGACAAAGAAAACGCTATCGAC 60 Sbjct 63 ATGGACGCTATCAAAAAGAAGATGCAGATGCTGAAACTGGACAAAGAAAACGCTATCCAT 122
Tpm2.2-E41K (GAG->AAA)	Query 121 GAGGAACAGCAGGCACTGCaaaaaaaaCTGAAAGGTACCGAAGACGAAGTTGAAAAATAC 180 Sbjct 184 AAAGAACAGCAGGCACTGCAAAAAAAACTGAAAGGTACCGAAGACGAAGTTGAAAAATAC 243
Tpm2.2-E181K (GAA->AAA)	Query 540 GAACGTGCTGAAGTTGCTGAATCTAAATGCGGTGACCTTGAAGAAGAACTGAAAATCGTT 599 Sbjct 604 AAACGTGCTGAAGTTGCTGAATCTAAATGCGGTGACCTTGAAGAAGAACTGAAAATCGTT 663
Tpm2.2-N202K (CAA->AAA)	Query 601 ACCAACAACCTGAAATCTCTGGAAGCTCAGGCTGACAAATACTCTACCaaagaagacaaa 660 Sbjct 663 ACCAAAAACCTGAAATCTCTGGAAGCTCAGGCTGACAAATACTCTACCAAAGAAGACAAA 722

The alignments of the nucleotides for the *TPM2* variants indicate that the intended substitutions were successfully introduced in the *TPM2* sequence.

5.3 Bacterial expression and purification of Tpm2.2 variants carrying disease-causing amino acid substitutions

To express, isolate, and purify Tpm2.2 variants, standard protocols for recombinant Tpm2.2 were used as described in Methods (section 4.3). No further optimization of the protocol for mutant Tpm2.2 was needed.

E. coli strain BL21(DE3) cells transformed with pET11a vector carrying Tpm2.2 cDNA were induced for production of the protein. The recombinant protein was released from bacteria by cell lysis and purified. Subsequent purification steps are shown in Figure 5.3 A. Before induction with IPTG, only a weak band corresponding to the expected molecular weight of Tpm was visible, indicating low basal expression of the recombinant protein. After IPTG induction, this band became clearly stronger compared with the other bacterial protein bands in the same lane, confirming efficient expression of recombinant Tpm. Boiling was one of the main separation steps during purification. After heat treatment, most of the recombinant Tpms remained in the supernatant, whereas many bacterial protein impurities were denatured and collected in the pellet after centrifugation. The supernatant obtained after boiling was then subjected to ammonium sulfate precipitation. Increasing the ammonium sulfate concentration

to 70% promoted reversible precipitation of recombinant Tpm, allowing the protein to be collected by centrifugation. The precipitated Tpm was subsequently dissolved in the appropriate buffer. At the final stage, Tpm2.2 variants were subject to ion-exchange chromatography, which not only removed nucleic acids from the protein preparation, but also removed the low molecular weight protein impurities (Figure 5.3 B).

Fractions eluted from chromatography column, containing pure protein were pooled, and protein concentrations were determined as described in Methods (see section 4.3). In different preparations, from a total culture volume of 2.4 liters, 4-6 mL of purified Tpm2.2 was obtained at a concentration varying between 39 and 46 μM. Based on a molecular weight of 32.85 kDa (284 amino acids), the total protein yield was approximately 6.0 mg, corresponding to ≈ 2.5 mg of purified protein per liter of bacterial culture.

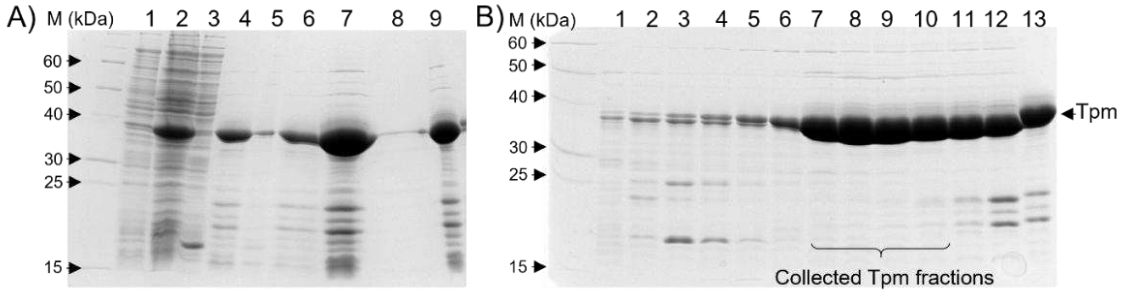

Figure 5.3. Steps of recombinant Tpm2.2 purification. (A) 1 – proteins expressed in bacterial cells before induction of recombinant protein expression with IPTG, 2 – proteins expressed in bacterial cells after induction of recombinant protein expression with IPTG, 3 – denatured proteins collected in pellet after boiling, 4 – proteins left in supernatant after boiling, 5 – pellet obtained at 35% saturation with $(NH_4)_2SO_4$, 6 – supernatant obtained at 35% saturation with 35% of $(NH_4)_2SO_4$, 7 – pellet obtained at 70% saturation with $(NH_4)_2SO_4$, 8 – supernatant obtained at 70% saturation with $(NH_4)_2SO_4$, 9 – protein solution before chromatography column (B) SDS–PAGE of Tpm fractions eluted from the DEAE column. Individual lanes (1 to 13) correspond to chromatography fractions containing Tpm. Molecular weight standards are shown in the marker lane on the left. Samples were resolved on a 12% polyacrylamide gel and stained with Coomassie Brilliant Blue G-250.

The amino acid substitutions introduced into Tpm2.2 altered not only protein mass, but also the charge of individual residues at pH 7.0, resulting in either charge reversal from negative to positive (E41K and E181K), a change from negative to neutral (D20H), or a change from neutral to positive (N202K). To determine whether these substitutions affected the electrophoretic mobility of the proteins, the purified Tpm2.2 variants were analyzed side-by-side by SDS–PAGE. As shown in Figure 5.4, all variants exhibited similar electrophoretic mobility, with the exception of Tpm2.2-E181K, which migrated slightly faster than the wild-type protein. This difference cannot be explained by the mass and charge change associated with the substitution, as the E41K variant carries the same charge reversal and a comparable

change in molecular mass but migrated similarly to the wild type. The basis for the altered mobility of Tpm2.2-E181K remains unclear. One possible explanation is that the E181K substitution affects the interaction of the denatured protein with SDS, resulting in altered electrophoretic mobility.

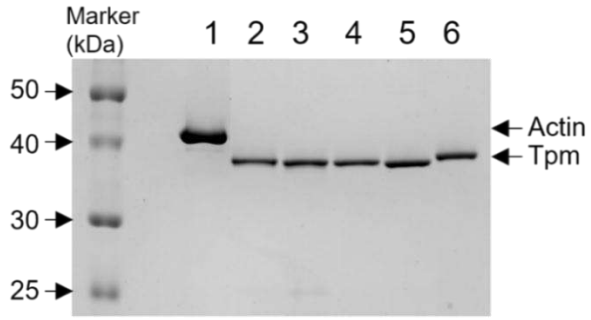

Figure 5.4 SDS–PAGE analysis of Tpm2.2 variants highlighting differences in electrophoretic mobility. Purified wild-type Tpm2.2 and its variants were separated on a 12% polyacrylamide gel and stained with Coomassie Brilliant Blue G-250. Lanes: 1 – Actin, 2 – Wild-type Tpm2.2, 3 – Tpm2.2-D20H, 4 – Tpm2.2-E41K, 5 – Tpm2.2-E181K, 6 – Tpm2.2-N202K.

In summary, the subsequent purification steps yielded all Tpm2.2 variants at near homogeneity and in amounts sufficient for biochemical assays.

5.4 Analysis of the effects of *TPM2* mutations on the affinity of Tpm to F-actin in the reconstituted thin filament

The point mutations were introduced into actin-binding periods P1 and P5. However, only the substitutions D20H and E181K were located in the N-terminal halves of Tpm2.2, which contain residues directly interacting with actin. To check whether the point mutations selected for this work affect actin binding of Tpm2.2 to F-actin, a co-sedimentation assay was used. To determine Tpm2.2 concentration required for saturation of the filaments, F-actin at constant concentration was incubated with increasing concentrations of Tpm2.2 variants. Filament-bound Tpm2.2 was separated from the unbound fraction via high-speed ultracentrifugation, and the resulting pellets were resolved on SDS-PAGE and visualized using Coomassie Brilliant Blue G-250 staining (Figure 5.5 A). Densitometric analysis of the protein bands present in pellets was performed, and the saturation was quantified by calculating the ratio of Tpm2.2 band intensity relative to the corresponding actin band.

Co-sedimentation analysis showed comparable amounts of wild-type and mutant Tpm2.2 in the pellet fraction. A molar ratio of 1:4 (0.75 μM Tpm2.2 to 3.0 μM F-actin) was

sufficient to achieve saturation of actin filaments. These results indicate that none of the amino acid substitutions significantly affected the binding of Tpm2.2 to F-actin (Figure 5.5 B).

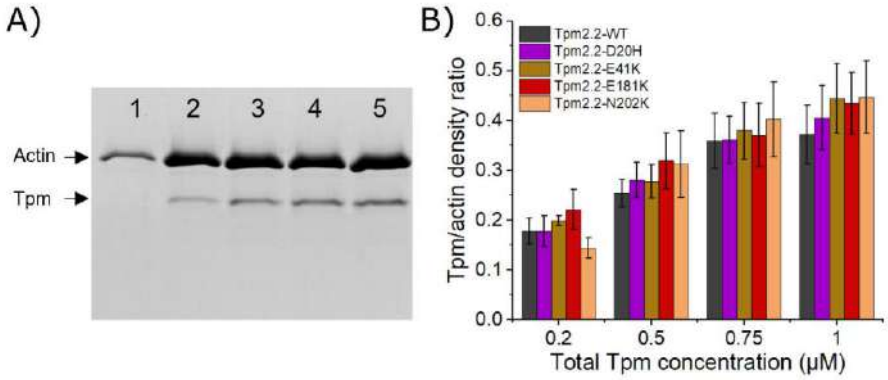

Figure 5.5 Binding of Tpm2.2 variants to F-actin. (A) SDS-gel showing protein composition in pellets. Lanes: 1 – Control of G-actin solution, 2 – F-actin + 0.2 μM Tpm, 3 – F-actin + 0.5 μM Tpm, 4 – F-actin + 0.75 μM Tpm, 5 – F-actin + 1 μM Tpm. (B) Densitometric ratios of Tpm/actin band intensities in pellets. Conditions: 3 μM F-actin, Tpm2.2 as indicated above, 30 mM NaCl, 2 mM $MgCl_2$, 5 mM imidazole, pH 7.0, and 0.5 mM DTT. Data represent the mean ± SEM of three independent experiments.

To further examine ternary complex formation, co-sedimentation assays were performed in which Tpm2.2-decorated F-actin was supplemented with increasing concentrations of Tn. Complex formation was determined in a concentration-dependent manner by densitometric analysis of proteins in the pellet fractions after SDS-PAGE separation. Consistent with the results described above, in the absence of Tn all Tpm2.2 mutants displayed F-actin binding properties comparable to wild-type Tpm2.2. Because on SDS-gels TnT band migrates very close to Tpm2.2 band (Figure 5.6 A), in densitometric analysis of actin saturation with Tpm both Tpm and TnT bands were included (Figure 5.6 B and C). Similar results were obtained in both the presence and absence of Ca^{2+}, indicating that the substitutions do not influence troponin-dependent association of Tpm2.2 with F-actin in different activation states.

In addition, TnI/actin densitometric ratios were analyzed in order to check whether Tpm2.2 mutations affect interaction of Tn complex with F-actin. The TnI/actin ratios (Figure 5.6 D and E) obtained at increasing Tn concentrations demonstrated that in the absence or presence of Ca^{2+}, binding of Tn complex to the filament was also not affected.

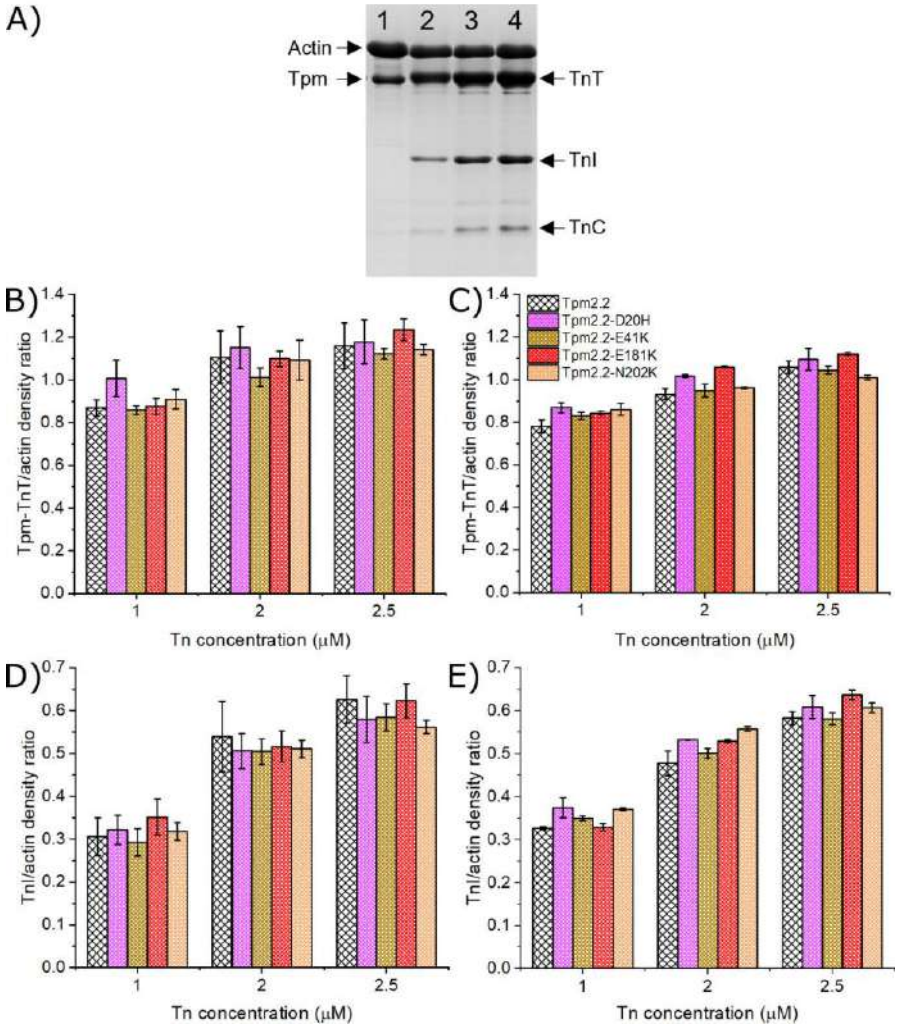

Figure 5.6 Formation of the F-actin-Tpm2.2-Tn ternary complex. (A) SDS-gel showing protein composition in pellets. Lanes: 1 – F-actin + Tpm, 2 – F-actin + Tpm + 1 μM Tn, 3 – F-actin + Tpm + 2 μM Tn, 4 – F-actin + Tpm + 2.5 μM Tn. Densitometric ratios of Tpm2.2-TnT to F-actin bands obtained from SDS–PAGE gels in the presence (B) or absence of 0.1 mM Ca^{2+} (C). Densitometric ratios of TnI to F-actin bands measured in the presence (C) or in the absence of Ca^{2+} (D). Wild-type Tpm2.2 is shown as black striped bars, Tpm2.2-D20H as violet bars, Tpm2.2-E41K as green bars, Tpm2.2-E181K as red bars, and Tpm2.2-N202K as blue bars. Conditions: 5 μM F-actin, 1.4 μM Tpm2.2 variants, 25 mM HEPES, pH 7.5, 6 mM NaCl, 5 mM $MgCl_2$, 1 mM DTT, and either 0.1 mM $CaCl_2$ or 0.2 mM EGTA. Data represent the mean ± SEM of three independent experiments. No statistically significant differences were detected using one-way ANOVA.

Together, the cosedimentation assays showed that despite localization in four different regions of Tpm2.2, the single amino acid substitutions did not influence Tpm2.2 affinity neither for actin alone nor actin and Tn.

5.5 The effects of mutations on Tpm2.2 orientation on actin filaments

Following the determination of Tpm saturation over actin, we next investigated whether the single amino acid substitutions alter the specific binding conformation of Tpm2.2 on the actin filament. To accomplish this, we performed FRET experiments to evaluate potential changes in orientation of Tpm2.2 chains on the filament, as described in Methods (Figure 4.4).

As shown in Figure 5.7 A, binding of pyrene-labeled Tpm2.2 caused a decrease in the actin donor fluorescence signal, indicating that the distance between the donor and acceptor fluorophores was within the range required for FRET to occur. The strong tryptophan emission peak at 330 nm observed for F-actin, dropped when pyrene-labeled Tpm2.2 was added. This energy transfer was also confirmed by a simultaneous increase in the pyrene excimer signal, which appeared as a peak around 490 nm.

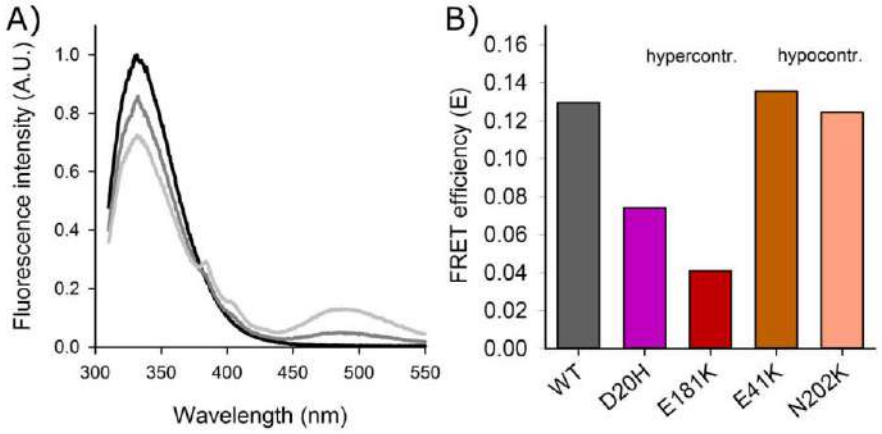

Figure 5.7 Energy transfer from actin Trp (donor) to pyrene-labeled Tpm2.2 (acceptor). (A) Trp emission spectrum of 2 μM F-actin alone (black line) and in the presence of either 0.26 μM Tpm2.2 (dark gray line) or 0.78 μM Tpm2.2 (light gray line), recorded using an excitation wavelength of 285 nm. (B) Calculated FRET efficiencies for wild-type and mutant Tpm2.2 variants. Error bars represent ± SEM derived from error propagation rules and are too small to be visually distinguished. Conditions: 2.0 μM F-actin, 0.2 μM of Tpm2.2 variants in 10 mM Hepes, pH 7.6, 30 mM NaCl, 2 mM $MgCl_2$.

The differences in FRET efficiencies measured after the donor fluorescence reached its lowest stable point (Figure 5.7 B) show that the hypercontractile (D20H and E181K) substitutions changed the position of Tpm2.2 on F-actin. The decrease in FRET efficiency indicates that the donor-acceptor distance was increased. In contrast, the hypocontractile mutations (E41K and N202K) had no measurable effect on how Tpm2.2 interacts with actin as compared to wild-type Tpm2.2.

In conclusion, although none of the examined disease-causing substitutions affected Tpm2.2 affinity for actin and Tn, the hypercontractile variants changed orientation of Tpm2.2 on the filaments shifting Tpm2.2 chains from actin SD1.

5.6 Analysis of the effect of *TPM2* mutations on the steady-state actomyosin ATPase

As shown by co-sedimentation and FRET analyses, the mutations caused phenotype-related differences in Tpm2.2 orientation on the filament without changing the overall affinity

of Tpm2.2 for actin. As the structural differences could underlie the regulatory performance of Tpm2.2, next the functional ATPase assay was used to determine whether hyper- and hypocontractile variants exhibited distinct effects in regulation of actomyosin cross-bridge cycle. To follow release of inorganic phosphate during the ATP hydrolysis on myosin heads, the steady-state ATPase measurements were employed.

Since inhibition of actin-myosin interactions is a well-known feature of Tpm (Lehrer & Morris, 1982), the activity of actomyosin ATPase was analyzed in function of Tpm2.2 concentration. As illustrated in Figure 5.8, at saturating concentrations the hypercontractile D20H and E181K variants of Tpm2.2 were less inhibitory than the hypocontractile E41K and N202K compared to wild type (Figure 5.8 A). The inhibitory potential of the Tpm2.2 variants, calculated for the highest concentration of Tpm2.2 used in this assay, is shown as the percentage of the ATPase observed in the absence of Tpm2.2 (Figure 5.8 B and Table 5.2). It indicates a substantial decrease in the ability of hypercontractile variants to inhibit actin-myosin interactions, while the hypocontractile variants tended to inhibit the ATPase even more efficiently than the wild-type, however the difference at the end point were not statistically significant.

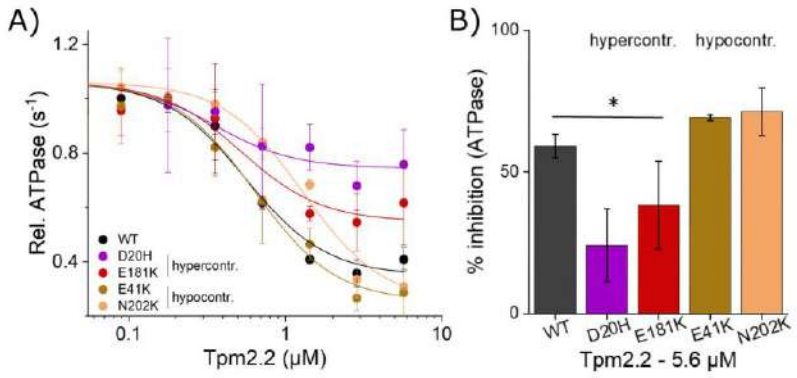

Figure 5.8 Effects of amino acid substitutions in Tpm2.2 on myosin steady-state ATPase activity. (A) Steady-state ATPase measurements. Data points represent S1 ATPase activity measured at 5 μM F-actin and increasing concentrations of Tpm2.2, expressed relative to S1 ATPase activity in the absence of Tpm2.2 (± SD). Solid lines represent fits to the Hill–Langmuir equation. (B) Inhibitory potential of Tpm2.2 variants on S1 ATPase activity. Bars show the overall inhibition of S1 ATPase at saturating Tpm2.2 concentrations (± SD). Statistical significance compared to wild-type Tpm2.2 was determined using Student's *t*-test: * $0.01<p<0.05$. Points represent the ATPase activity of 0.3 μM myosin S1, 5 μM F-actin, and 0 – 5.6 μM Tpm2.2. Conditions: 25 mM HEPES pH 7.3, 25 mM KCl, 5 mM $MgCl_2$ and 1 mM DTT, and 2 mM ATP at 23-25 °C.

The dependence of the ATPase inhibition on Tpm2.2 concentration was evaluated by calculating EC_{50}, the concentration required to reach 50% of maximal inhibition. The data collected in Table 5.2 show that most mutant Tpm2.2 did not significantly affect EC_{50} value, except for the Tpm2.2-N202K. Although this variant caused the strongest inhibition, it showed

the highest EC_{50} value, which indicates that the ATPase dependence on the Tpm2.2 concentration was strongly affected. Unlike other variants, Tpm2.2-N-202K was required at about 2-fold higher concentrations to reach half maximal inhibition than the wild type Tpm2.2.

The regulatory effects of Tpm2.2 variants on actomyosin ATPase activity were further investigated in the presence of the Tn complex, the ATPase activity measurements were performed in the presence and absence of Ca^{2+} (Figure 5.9**)**. In the presence of Ca^{2+}, wild-type Tpm2.2 enhanced actomyosin ATPase activity by more than 40%.

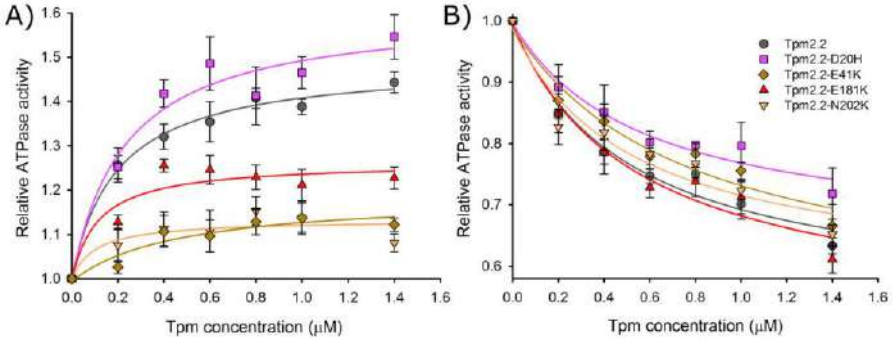

Figure 5.9 Regulation of actomyosin ATPase activity by Tpm2.2 variants and Tn. (A) Activation of actomyosin ATPase in the presence of Ca^{2+} (0.1 mM $CaCl_2$). Data points represent ATPase activity measured at fixed actin and S1 concentrations with increasing concentrations of Tpm2.2. Activities are normalized to actomyosin ATPase in the absence of Tpm2.2-Tn. Solid lines represent fits of the data to a hyperbolic equation. (B) Inhibition of actomyosin ATPase in the absence of Ca^{2+} (0.2 mM EGTA). Data were fitted using a hyperbolic decay equation. Points represent the ATPase activity of 1 μM myosin S1, 5 μM F-actin, and Tn at 2-molar excess over Tpm. Conditions: 30 mM NaCl, 2 mM $MgCl_2$, 5 mM imidazole, pH 7.0, 1 mM DTT, 3 mM ATP, and either 0.1 mM $CaCl_2$ or 0.2 mM EGTA, at 23-25 °C. The experimental points were averaged from three independent experiments and normalized to the S1 ATPase activity in the absence of Tpm2.2-Tn ± SEM.

In contrast, the Tpm2.2 variants exhibited either enhanced or reduced activation (Table 5.2). Consistent with the functional characteristics of hypocontractile phenotype, Tpm2.2-E41K and Tpm2.2-N202K displayed only weak activation of ATPase activity within the tested concentration range. As expected for hypercontractile phenotype, at saturating concentrations Tpm2.2-D20H increased ATPase activity above the maximum observed for wild-type Tpm2.2. In contrast, Tpm2.2-E181K showed only modest activation, remaining below the level observed for the wild-type Tpm2.2, which did not fully agree with the phenotype.

Under relaxing conditions (in the absence of Ca^{2+}) all examined Tpm2.2 variants suppressed actomyosin ATPase activity. Analysis of the data using a hyperbolic decay model estimated maximal inhibition values between 36% and 48% (Figure 5.9 B; Table 5.2). The Tpm2.2-D20H variant showed the smallest inhibition in ATP turnover, in agreement with its

hypercontractile characteristics. The remaining mutant proteins displayed inhibition levels that were largely comparable to those of the wild-type Tpm2.2.

Table 5.2. Mutation-dependent changes in the regulation of steady-state actomyosin ATPase activities.

		Hypercontractile		**Hypocontractile**	
	Tpm2.2	**Tpm2.2-D20H**	**Tpm2.2-E181K**	**Tpm2.2-E41K**	**Tpm2.2-N202K**
Steady-state ATPase with Tpm					
Inhibition (%)	59 ± 4	24 ± 13	38 ± 16	69 ± 1	71 ± 8
EC_{50} (μM)	0.62 ± 0.02	0.65 ± 0.95	0.89 ± 0.13	0.85 ± 0.12	1.58 ± 0.14
Steady-state ATPase with Tpm-Tn					
Maximum activation (%) in the presence of Ca^{2+}	48.6 ± 2.6	60.9 ± 7.6	26.5 ± 5.2*	19.2 ± 4.9**	13.3 ± 4.1***
Maximum inhibition (%) in the absence of Ca^{2+}	45.9 ± 4.5	35.9 ± 4.3	48.3 ± 5.9	46.3 ± 7.8	42.1 ± 6.8
EC_{50}^{act} (μM)	0.20 ± 0.04	0.23 ± 0.10	0.11 ± 0.10	0.45 ± 0.35	0.10 ± 0.14
EC_{50}^{inh} (μM)	0.51 ± 0.20	0.57 ± 0.26	0.54 ± 0.26	0.78 ± 0.44	0.54 ± 0.34
pCa_{50}	5.86 ± 0.10	6.28 ± 0.09*	6.25 ± 0.09*	5.15 ± 0.13*	5.20 ± 0.27
Temperature-dependent ATPase					
E_a (kJ/mol)	79.11 ± 2.69	86.57 ± 0.78	99.89 ± 1.42	82.21 ± 1.03	78.36 ± 2.30

The values of maximum activation and inhibition represent the mean percentage (± SD) obtained from three independent experimental replicates. The statistical significance as comparing to wild-type Tpm2.2: *** $p<0.001$, ** $0.001<p<0.01$, * $0.01<p<0.05$. EC_{50}^{act} – Tpm concentration required to achieve 50% activation of the ATPase in the presence of 0.1 mM Ca^{2+}; EC_{50}^{inh} – Tpm concentration required to achieve 50% inhibition of the ATPase in the absence of Ca^{2+}. E_a - activation energy of myosin S1 ATPase activity in the presence of Tpm2.2 variants.

The concentrations corresponding to half-maximal activation (EC_{50}^{act}) and half-maximal inhibition (EC_{50}^{inh}) were determined by fitting the data to hyperbolic curves. Although Tpm2.2-E41K showed a tendency toward a higher EC_{50}^{act} compared with the other variants, the observed difference was not statistically significant because of the experimental data variability. In contrast, EC_{50}^{inh} values were similar among all tested variants, with no differences within experimental error.

Since E181K was linked to hypercontractile phenotype, reduced activation of the actomyosin ATPase in the presence of Tpm2.2-E181K described above was counterintuitive. Because residue E181 is located in the region where Tpm2.2 interacts with Tn core domain, the result obtained *in vitro* could be a consequence of distortions in Tpm-Tn interactions. To check

whether higher concentrations of Tn further increased activation of the ATPase, the experiment was performed as in the presence of Ca^{2+} at a constant actin–Tpm and increasing Tn concentrations (Figure 5.10). The results showed trends similar to those observed in the previous experiment (Figure 5.9). Both hypocontractile variants, Tpm2.2-E41K and Tpm2.2-N202K, suppressed ATPase activity below the level observed for wild-type Tpm2.2 at the entire range of Tn concentrations.

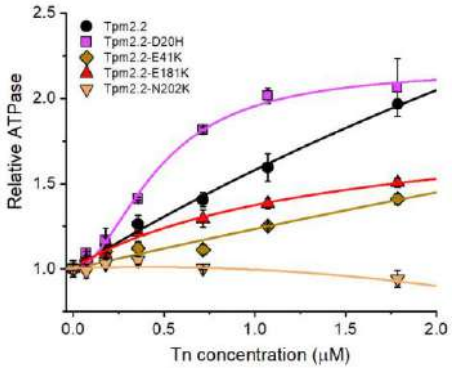

Figure 5.10 Effect of Tn concentration on myosin ATPase activity in the presence of Tpm2.2 variants. Myosin S1 ATPase activity was measured at a constant actin–Tpm ratio with increasing concentrations of troponin in the presence of 0.1 mM $CaCl_2$. Points represent the ATPase activity of 0.3 μM myosin S1, 5 μM F-actin, 0.75 μM Tpm2.2 and increasing Tn concentration. Conditions: 25 mM HEPES pH 7.3, 25 mM KCl, 5 mM $MgCl_2$ and 1 mM DTT, and 2 mM ATP, 0.1 mM $CaCl_2$, at 23-25 °C. The experimental points were averaged from three independent experiments and normalized to the S1 ATPase activity in the absence of Tn ± SEM.

The hypercontractile mutant Tpm2.2-D20H exhibited the highest ATPase rates across the tested Tn concentrations. In contrast, Tpm2.2-E181K activated ATPase activity to a lesser extent than wild-type Tpm2.2. Thus, the inability of higher Tn concentrations to restore ATPase hyperactivation indicates that the E181K substitution adversely affected the activation of actomyosin ATPase by the Tpm–Tn complex under these experimental conditions.

In summary, the disease-causing substitutions substantially altered the regulation of actomyosin ATPase activity. In the absence of Tn, the hypocontractile variants inhibited ATPase activity to the same extent as the wild type, whereas the hypercontractile variants exhibited reduced inhibitory activity, indicating impaired relaxation. In the presence of the reconstituted Tpm2.2–Tn complex, the hypocontractile variants failed to fully activate ATPase while retaining their inhibitory activity. Among the hypercontractile variants, only Tpm2.2-D20H fully displayed the expected phenotype, exhibiting both reduced inhibition and enhanced ATPase activation. Under the conditions used in the ATPase assay, Tpm2.2-E181K did not exhibit the regulatory properties characteristic of the hypercontractile phenotype.

5.7 Temperature dependence of the actomyosin ATPase activation by Tpm2.2 variants and the Tn complex in the presence Ca^{2+}

Because thin filaments in human muscle function at body temperature, which is higher than the temperatures typically used in *in vitro* experiments, we hypothesized that the reduced activation of the steady-state ATPase observed in the presence of the E181K mutation might result from an increased activation energy (E_a). To check this possibility, temperature-dependent ATPase assays were performed

The activation of the ATPase over the range of 22.8–40.0 °C (Figure 5.11 A) shows that independently on the temperature, in the presence of the hypocontractile variants the activity of the ATPase remained below the activity observed for the wild-type Tpm2.2, whereas in the presence of Tpm2.2-D20H it was always hyperactivated. In contrast, in the presence of Tpm2.2-E181K the temperature dependence plot shows that the ATPase was indeed temperature-dependent. As compared to wild type, Tpm2.2-E181K exhibited hyperactivation at temperatures above 32 °C. This suggests that at physiological temperatures the E181K mutation causes hypercontractile phenotype.

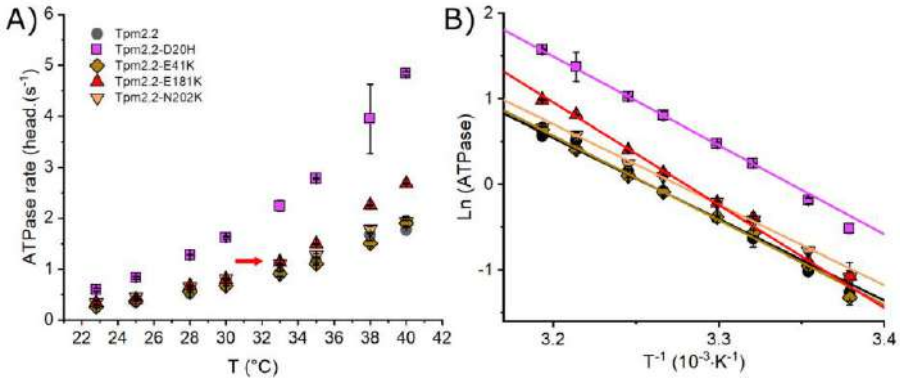

Figure 5.11 Temperature-dependent effects of Tpm2.2 variants on the ATPase activity of thin filament regulated with Tpm2.2 variants. (A) ATPase activity plotted as a function of temperature (°C). (B) Arrhenius plot showing the natural logarithm of ATPase activity as a function of reciprocal temperature (K^{-1}). The red arrow indicates the first experimental point where the activation of the ATPase in the presence of Tpm2.2-E181K exceeds the activation in the presence of wild-type Tpm2.2. Protein concentrations were 5 μM F-actin, 0.71 μM Tpm variants, and 1.07 μM troponin. Measurements were performed in 25 mM HEPES, pH 7.5, 25 mM KCl, 5 mM $MgCl_2$, 1 mM DTT, and 0.1 mM $CaCl_2$. Data represent the mean of three independent experiments, and lines represent linear regression fits (± SD).

To calculate the E_a values the Arrhenius equation (Equation 2) was used. Arrhenius linearization of the effects of all mutations on the activation energy is illustrated in Figure 5.11 B. It shows that unlike the other mutants, the line representing Tpm2.2-E181K is more tilted than for wild type, indicating higher E_a. It demonstrated that most Tpm2.2 variants exhibited activation energies comparable to that of the wild-type Tpm2.2 with exception of the E181K

mutant, which showed an approximately 20% increase relative to wild-type Tpm2.2 (Table 5.2).

The D20H variant displayed a marked upward shift in the Arrhenius plot, consistent with the elevated ATP turnover rates observed across the investigated temperature range. Despite this shift, its activation energy remained similar to that of the wild-type, suggesting that the mutation does not substantially alter the enthalpic properties to the reaction. To assess whether temperature-dependent changes in pH could influence the observed ATPase activity, additional control experiments were conducted under different pH conditions. These analyses showed no significant effect of temperature-related pH variation on enzymatic activity.

In conclusion, among the disease-associated Tpm2.2 substitutions examined, E181K uniquely exhibited temperature-dependent behavior, displaying a hypercontractile phenotype only at temperatures close to physiological.

5.8 Analysis of the effect of *TPM2* mutations on the sensitivity of actomyosin ATPase to varying concentrations of Ca^{2+} ions

To further investigate the functional consequences of the Tpm2.2 mutations, their effects on troponin-mediated Ca^{2+} regulation of actomyosin ATPase activity were examined. Because the impact of Tpm variants on thin-filament activation may vary across different Ca^{2+} concentrations, ATPase activity was assessed over a range of Ca^{2+} levels to determine potential alterations in Ca^{2+} sensitivity. In agreement with the findings shown in Figure 5.9, the Tpm2.2 variants caused distinct effects on both the inhibitory and activating phases of ATPase activity (Figure 5.12 A). All Tpmn2.2 variants exhibited substantial differences in the ATPase activity levels at both the inhibiting (pCa in the range 9-7) and activating (pCa between 3-4) Ca^{2+} concentrations.

To enable a more direct assessment of differences in Ca^{2+} sensitivity, the ATPase data were also normalized and plotted accordingly (Figure 5.12 B). Variations in Ca^{2+} sensitivity were reflected by shifts in the inflection points of the curves fitted to Hill equation relative to wild-type Tpm2.2. A shift toward higher pCa values indicated enhanced Ca^{2+} sensitivity, whereas shifts toward lower pCa values were indicative of reduced sensitivity. In line with their functional phenotypes, hypercontractile variants displayed increased responsiveness to Ca^{2+}, while hypocontractile mutants exhibited a diminished Ca^{2+} sensitivity of ATPase activity (Table 5.2). Statistical analysis using Student's *t*-test confirmed that all differences were statistically significant.

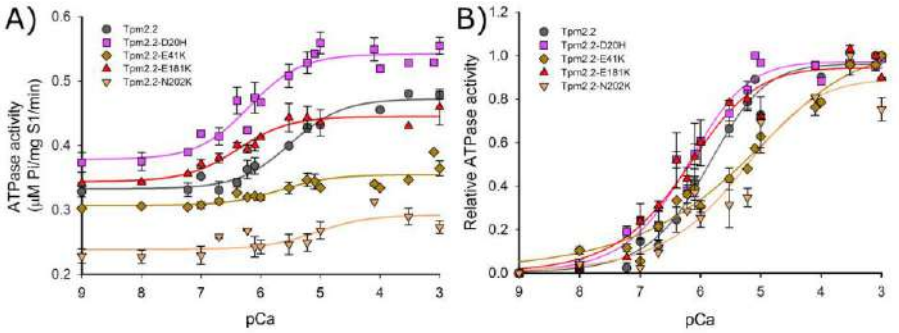

Figure 5.12 Regulation of ATPase activity in reconstituted thin filaments by Tpm2.2 variants in a Ca^{2+}-dependent manner. ATPase rates are displayed as absolute values (A) and as normalized activities relative to the maximal and minimal ATPase rates obtained for each protein variant (B). Symbols denote wild-type Tpm2.2 (black circles), D20H (violet squares), E41K (green diamonds), E181K (red triangles), and N202K (blue inverted triangles). Assays were conducted in the presence of 1 μM myosin S1, 5 μM F-actin, 1 μM Tpm, and 2 μM Tn. Data represent the mean ±SEM of three independent experiments. Statistical differences in pCa values between wild type and mutants were: Tpm2.2-D20H ($p = 0.03$), Tpm2.2-E41K ($p = 0.01$), and Tpm2.2-E181K ($p = 0.03$).

Taken together, the Ca^{2+}-sensitivity analyses indicate that the disease-causing single amino acid substitutions profoundly alter the function of the Tpm2.2–Tn complex, resulting in distinct effects on actomyosin ATPase activity at different Ca^{2+} concentrations.

5.9 Effects of the myopathy-causing mutations on nucleotide-dependent actomyosin interactions

To determine which steps of the cross-bridge cycle were affected by substitution-induced structural changes in Tpm2.2, more detailed analyses of actin–myosin interactions were performed. Single-turnover experiments were used to measure acto–myosin dissociation kinetics and individual ATP hydrolysis events under conditions in which each myosin head was allowed to hydrolyze only a single ATP molecule. To ensure the single-turnover conditions, in each type of experiment ATP concentration was kept below the concentration of myosin head. Stopped-flow instrument was used to mix pre-incubated proteins with labeled or unlabeled ATP within milliseconds by using double mixer and to follow fluorescence changes within millisecond time range (see section Method 4.13).

In the first type of experiments, the effects of Tpm2.2 mutants on the interaction of myosin S1 with actin during the ATP hydrolysis event were analyzed (Figure 5.13). Due to fluorescence quenching, pyrene–actin fluorescence is minimal when myosin heads are bound to actin and maximal when myosin heads are dissociated. Thus, the observed fluorescence change reflects ATP-induced dissociation of myosin S1 from actin followed by actomyosin reassociation after ATP hydrolysis.

All Tpm2.2 variants, including wild type, showed higher pyrene fluorescence intensity compared with undecorated actin filaments, indicating that a larger fraction of myosin heads dissociated from actin in the presence of Tpm2.2 (Figure 5.13 A).

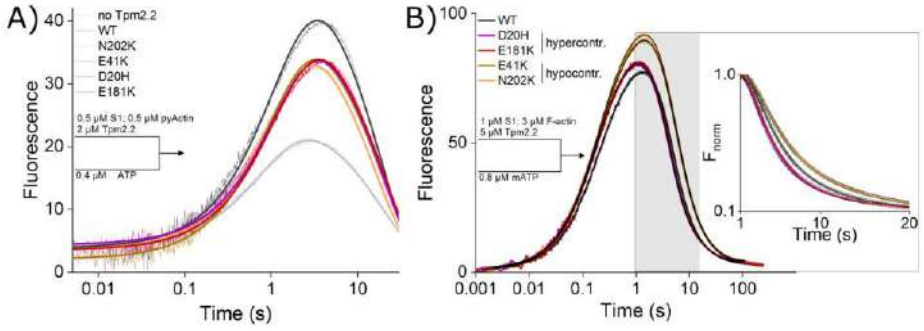

Figure 5.13 Effects of myopathy-causing mutations in Tpm2.2 on single ATP turnover kinetics of myosin S1. (A) Time courses of pyrene fluorescence recorded after rapid mixing of a solution containing 0.5 μM myosin S1, 0.5 μM pyrene-labeled actin, and 2 μM Tpm2.2 with 0.4 μM ATP. Solid lines represent fits of the fluorescence transients to biexponential functions. (B) Time courses of mant fluorescence following rapid mixing of a solution containing 1 μM myosin S1, 3 μM F-actin, and 5 μM Tpm2.2 with 0.8 μM mantATP. Transients represent the average of two to four independent experiments. Solid lines correspond to fits of the fluorescence profiles to the sum of four exponential functions.

The highest fraction of myosin dissociation (A_{max}) was observed with wild-type Tpm2.2 (Table 5.3). The ability of all mutant variants to limit myosin association with actin was significantly reduced compared to the wild type. However, analysis of the single-turnover fluorescence time courses revealed no significant differences in the kinetic rates of actomyosin dissociation (k_{diss}) or reassociation (k_{ass}) among the mutants (Table 5.3).

Table 5.3 Kinetic parameters for single ATP turnover in the presence of myosin and Tpm2.2 variants

			hypercontractile		**hypocontractile**	
Parameter	**no Tpm2.2**	**Tpm2.2**	**D20H**	**E181K**	**E41K**	**N202K**
	Actomyosin dissociation and association kinetics					
A_{max}	20.7 ± 0.2	47.6 ± 0.2	38.5 ± 0.2	39.8 ± 0.3	40.9 ± 0.2	38.8 ± 0.2
k_{diss} (s^{-1})	1.19 ± 0.02	0.83 ± 0.01	0.81 ± 0.01	0.79 ± 0.01	0.90 ± 0.01	0.92 ± 0.01
k_{ass} (s^{-1})	0.05 ± 0.01	0.05 ± 0.01	0.05 ± 0.01	0.05 ± 0.01	0.06 ± 0.01	0.06 ± 0.01
	ATP-binding (k_{on}) and ADP-release (k_{off}) kinetics					
k_{on} (s^{-1})	n.d.	1.10 ± 0.02	1.10 ± 0.03	1.20 ± 0.03	1.10 ± 0.02	1.04 ± 0.01
k_{off} (s^{-1})	n.d.	0.29 ± 0.01	0.39 ± 0.01	0.38 ± 0.01	0.24 ± 0.01	0.23 ± 0.01

Errors represent residual standard errors.

In the second type of the single-turnover experiment, pre-formed complexes of F-actin-Tpm2.2-S1 were rapidly mixed with sub-equimolar concentrations of mantATP, and the resulting changes in mant fluorescence were monitored over time. Under these single-turnover

conditions, the fluorescence signal showed triphasic behavior (Figure 5.13 B). The initial fluorescence increase reports mantATP binding to myosin S1 and the concomitant dissociation of myosin from the Tpm-decorated actin filament. This was followed by a plateau phase, representing the hydrolysis reaction, and a final fluorescence decrease corresponding to mantADP dissociation from myosin S1, which is rate-limited by P_i release (Figure 5.13 B, inset). All Tpm2.2 constructs, including the wild type, exhibited similar ATP binding kinetics (k_{on}). In contrast, significant differences were observed in mantADP dissociation rates (k_{off}). The hypocontractile variants showed reduced k_{off} values, whereas the hypercontractile mutants displayed increased dissociation rates compared with wild-type Tpm2.2 (Table 5.3).

These results indicate that the disease-causing mutations affect the kinetics of interactions between myosin heads and actin, thereby contributing mechanistically to the phenotype.

5.10 Switching the F-actin-Tpm2.2 complex to the open state by strongly bound myosin S1

One of the key factors required for thin filament activation is the strong binding of myosin, which shifts the blocked–open equilibrium toward the open state and is accompanied by a change in the position of Tpm on the actin filament (McKillop & Geeves, 1993; Doran et al., 2020). Alterations in the cooperative activation of the thin filament may further contribute to the hypercontractile or hypocontractile phenotypes associated with the mutations. An experimental parameter that can help evaluating how effectively Tpm chains cooperate with myosin is the stoichiometric ratio of myosin heads to actin monomers required to fully switch Tpm into the open-state orientation (Moraczewska, Nicholson-Flynn, et al., 1999).

To determine whether Tpm2.2 variants affect the transition to the open state, changes in the excimer fluorescence of pyrene-labeled Tpm2.2 in response to the rigor binding of myosin S1 were monitored as described in Methods (Figure 4.5).

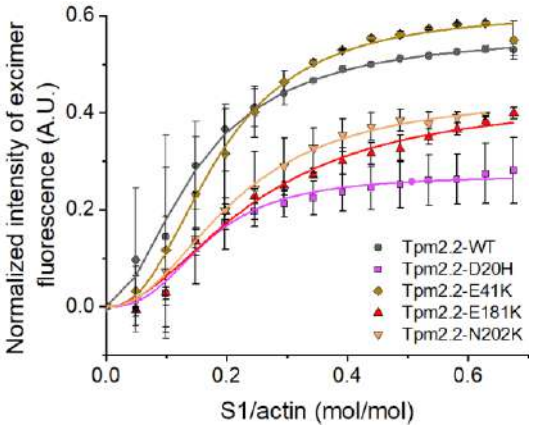

Figure 5.14 S1-induced changes in the excimer fluorescence of pyrene-labeled Tpm2.2 variants. Normalized excimer fluorescence intensity plotted as a function of the S1-to-actin molar ratio. Experimental conditions: 2 μM F-actin, 0.2 μM Tpm2.2 in 10 mM Hepes, pH 7.6, 30 mM NaCl, 2 mM $MgCl_2$. Myosin S1 concentration was titrated from 0 to 1.5 μM. Data represent the mean ± SEM of three to four independent experiments.

Titration of F-actin-Tpm2.2 complexes with myosin S1 induced a concentration-dependent increase in excimer fluorescence across all Tpm2.2 variants (Figure 5.14). Analysis of the titration curves using Hill fits revealed significant differences in both the maximal fluorescence change and the S1-to-actin ratio required for half-maximal activation. These parameters collectively report the efficacy of thin-filament activation by myosin (Table 5.4).

Table 5.4 Fitting parameters describing myosin S1-induced changes in excimer fluorescence of pyrene-labeled Tpm2.2 variants.

Tpm2.2 variant	Change in the excimer fluorescence	S1/actin (mol/mol) at 50% of maximal fluorescence
Tpm2.2	0.56 ± 0.015	0.15 ± 0.007
Tpm2.2-D20H	0.27 ± 0.010***	0.17 ± 0.010
Tpm2.2-E41K	0.61 ± 0.011	0.18 ± 0.005*
Tpm2.2-E181K	0.43 ± 0.003**	0.25 ± 0.026*
Tpm2.2-N202K	0.44 ± 0.010*	0.21 ± 0.006*

Note: Normalized data points, averaged from three to four independent experiments (Figure 5.14) were fitted to the Hill equation to derive the parameters. The low standard errors associated with the fitted parameters indicate that the normalized datasets were well described by a cooperative binding model (see Method 4.16). Statistical significance was determined using Student's *t*-test; *** $p<0.001$, ** $0.001<p<0.01$, * $0.01<p<0.05$ compared to wild-type Tpm2.2.

The results showed that the Tpm2.2-E41K variant displayed maximal excimer fluorescence intensity that was comparable to the wild-type Tpm2.2, indicating that this substitution does not substantially affect the orientation of Tpm2.2 on S1-decorated actin filaments. In contrast, the D20H, E181K, and N202K mutations resulted in reduced amplitudes of S1-induced fluorescence changes, suggesting alterations in the orientation of the Tpm2.2 open state relative to the wild-type configuration.

Notably, all mutations increased the myosin-to-actin ratio required to achieve half-maximal fluorescence changes (Table 5.4), indicating a reduced efficiency of myosin-mediated thin-filament activation. This effect was most pronounced for substitutions located within the actin-binding period P5. Although individual mutations affected specific parameters of thin-filament activation, no consistent association was detected between the molecular phenotype of a variant and its overall response to S1-induced activation.

In summary, the mutations affected the equilibrium between the closed and open states, indicating that the structural integrity of the Tpm2.2 chain is essential for proper thin filament regulation. However, based on the analysis of S1-induced changes in the excimer fluorescence of pyrene-labeled Tpm2.2, these alterations are unlikely to contribute substantially to the development of the hyper- and hypocontractile phenotypes.

5.11 Analysis of the effect of *TPM2* mutations on the motor functions of myosin heads

To explain the differential effects of the mutations on actomyosin ATPase activity relative to wild-type Tpm2.2, both in the absence and presence of Tn + Ca^{2+}, more direct analyses of myosin motor function using *in vitro* motility assays were performed. In this experimental system, surface-bound myosin heads molecules drive the movement of actin filaments (Figure 4.3), enabling quantification of actin sliding velocity as a measure of the functional performance of the actomyosin motor complex. In contrast to solution-based ATPase assays, the *in vitro* motility assay maintains a high local density of both myosin and actin within an ordered geometry. By providing a structured interface for protein interaction, this assay more closely mimics the physiological conditions of the sarcomere than bulk-phase biochemical measurements.

In vitro motility assays were performed using actin filaments decorated with Tpm2.2 variants, both in the absence and presence of the Tn +Ca^{2+}. Motility was initiated by the addition of ATP. Consistent with the clinical phenotypes and our previous ATPase data, the Tpm2.2 variants significantly modulated the actin translocation velocity (Figure 5.15 A).

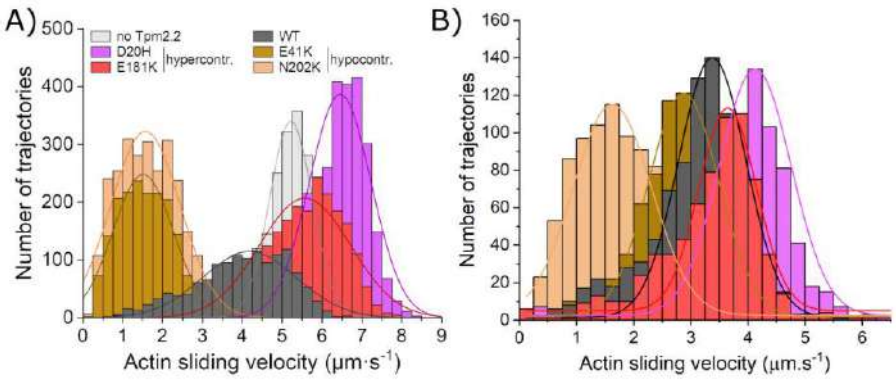

Figure 5.15 Impact of Tpm2.2 variants on actin sliding velocity distributions. (A) Sliding velocity distributions for bare and Tpm2.2-decorated Rhodamine-Phalloidin labeled actin filaments. Solid lines represent Gaussian fits to the data. Each distribution includes pooled events from three to five independent recordings. (B) Velocity distributions of F-actin regulated by Tpm2.2 variants and the Tn +Ca^{2+}. Experimental groups include: wild-type Tpm2.2 (black striped), D20H (violet striped), E41K (green striped), E181K (red striped), and N202K (blue striped). Assays were performed using 10 nM F-actin and 20 nM Tpm2.2-Tn complexes in a buffer containing 25 mM HEPES pH 7.3, 25 mM KCl, 5 mM $MgCl_2$, 0.1 mM $CaCl_2$, and 1 mM DTT at 23-25 °C. Solid lines indicate Gaussian fits. The total number of analyzed filaments and the number of recorded videos (in parentheses) are as follows: wild type (858, 3), D20H (903, 3), E41K (785, 3), E181K (688, 4), and N202K (840, 3).

The hypercontractile mutants, D20H and E181K, increased the average sliding velocity by more than 30% and 50%, respectively, relative to the wild-type Tpm2.2. Conversely, the hypocontractile mutants, E41K and N202K, led to a marked reduction in velocity, falling to approximately one-third of the wild type rate (Table 5.5). Beyond the reduction in mean velocity, a substantial fraction of actin filaments decorated with either the E41K or N202K variant remained immotile in the absence of Tn, further highlighting the severe inhibitory effect of these substitutions on actomyosin motility.

Table 5.5 Mutation-dependent changes in the regulation of the myosin motor function.

			Hypercontractile		**Hypocontractile**	
Parameter	**no Tpm2.2**	**Tpm2.2**	**D20H**	**E181K**	**E41K**	**N202K**
v (μm·s^{-1})	5.2 ± 0.1	4.2 ± 0.1	6.5 ± 0.1	5.6 ± 0.1	1.5 ± 0.1	1.6 ± 0.1
Immotile filaments (%)	1.7	5.2	4.7	8.1	27.4	36.4
+Tn +Ca^{2+}						
v (μm·s^{-1})	n.s	3.4 ± 0.1	4.1 ± 0.1	3.6 ± 0.1	2.9 ± 0.1	1.7 ± 0.1
Immotile filaments (%)	n.s	5.5	1.5	2.9	4.1	26.3

Errors of velocity are represented as residual standard errors arising from the Gaussian fitting.

Next, we investigated the influence of the Tn complex in the presence of Ca^{2+}. Under these conditions, the hypercontractile mutants increased the actin translocation velocity, whereas the hypocontractile mutants caused a marked decrease (Figure 5.15 B). These

observations align closely with the effects of mutations on the ATPase activity and correspond to clinical disease phenotypes demonstrating that the mutations' effects persist even in the presence of the full regulatory apparatus.

Interestingly, the addition of the regulatory complex exerted divergent effects on the two hypocontractile variants. For the E41K variant, the presence of Tn and Ca^{2+} reduced the proportion of stationary filaments to levels comparable to those observed for the wild type. In contrast, filaments decorated with Tpm2.2-N202K exhibited a high proportion of immotile filaments despite the presence of Tn and Ca^{2+} (Table 5.5). These findings suggest that the regulatory complex effectively stabilizes the active state of E41K-containing thin filaments, thereby promoting productive actomyosin interactions. In contrast, the Tpm2.2-N202K variant appears to impair formation or stabilization of the thin-filament "on" state, an effect that is not fully compensated by the presence of the Tn complex.

In summary, *in vitro* motility assays showed that the Tpm2.2 variants differentially regulated actin translocation in a manner consistent with their clinical phenotypes and effects on actomyosin ATPase activity. Hypercontractile variants increased sliding velocity, whereas hypocontractile variants markedly reduced motility. Notably, the Tn ($+Ca^{2+}$) complex largely restored motility of E41K-containing filaments but failed to rescue the severe impairment caused by N202K, indicating distinct mechanisms underlying the two hypocontractile phenotypes.

5.12 Analysis of the effect of *TPM2* mutations on the direct interactions between Tpm2.2 and Tn complex

To further investigate the molecular basis of the observed functional changes, we analyzed the direct interaction between the Tpm and Tn complexes. Specifically, an indirect ELISA (Figure 4.6) was employed to determine whether the investigated Tpm2.2 variants influence the binding affinity or cooperativity between Tpm2.2 and Tn in the absence of actin.

Microplates were coated with a constant amount of Tn, and titration experiments were performed by adding increasing concentrations of either wild-type or mutant Tpm2.2. In this experiment, the measure of Tpm-Tn affinity was the amount of Tpm2.2 required to achieve half maximal effect, which was absorbance at 655 nm indicating the level of Tn saturation with Tpm2.2. As demonstrated in Figure 5.16, the maximal effect was achieved at approximately 100 ng Tpm2.2 for all variants. Under pseudo-first-order conditions, the experimental data were fit to the Hill equation, revealing cooperative binding behavior for all Tpm2.2 variants.

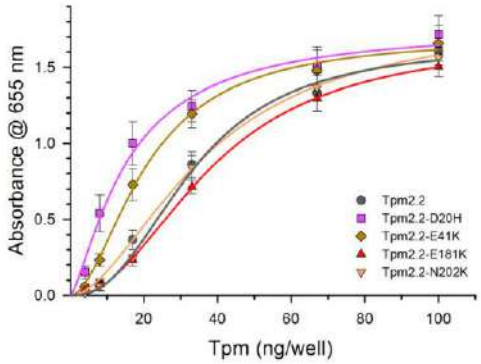

Figure 5.16 Equilibrium binding of Tpm2.2 variants to the Tn complex monitored by ELISA. Binding curves are shown for wild-type Tpm2.2 (black circles), D20H (violet squares), E41K (green diamonds), E181K (red triangles), and N202K (blue inverted triangles). Conditions: 25 mM MOPS, pH 7.4, 25 mM KCl, 5 mM $MgCl_2$, 1 mM EGTA, and 1 mM DTT, at 23-25 °C. Data represent the mean ± SEM of three independent experiments. Solid lines represent best fits to the Hill equation.

Interestingly, the binding profiles revealed a distinct position-dependent effect of the variants. Despite their opposing contractile phenotypes, the N-terminal mutants D20H and E41K located in P1 displayed a significant increase in binding strength, with ½ maximal binding approximately two-fold higher than that of the wild-type Tpm2.2 (Table 5.6). In contrast, the internal (P5) mutants E181K and N202K exhibited binding properties nearly identical to those of the wild-type. This suggests that mutations in the first actin-binding period might specifically modulate the stability of the Tpm-Tn interface.

Table 5.6 Mutation-dependent changes in Tpm2.2 binding to Tn.

	Tpm2.2 variant	**½ maximal binding (ng)**	***n***
	Tpm2.2	36.5 ± 3.2	1.8 ± 0.2
P1	Tpm2.2-D20H	15.6 ± 2.6*	1.4 ± 0.2
	Tpm2.2-E41K	20.7 ± 1.3*	1.8 ± 0.2
P5	Tpm2.2-E181K	38.5 ± 1.4	2.2 ± 0.1
	Tpm2.2-N202K	33.2 ± 1.2	2.4 ± 0.2

Note: ½ maximal binding (ng) = $[Tpm2.2]\left(\frac{1}{2}Abs_{max}^{655}\right)$; n is the Hill coefficient (Equation 3). Errors of ½ maximal binding and *n* were calculated from changes in the absorbance using error propagation. The numbers are averaged from three experiments. Statistical significance between wild-type Tpm2.2 and variants was determined using Student's *t*-test difference; *0.01 <p<0.05.

In summary, all Tpm2.2 variants bound Tn cooperatively, but only the P1 mutations (D20H and E41K) enhanced the direct Tpm2.2–Tn interaction. These findings indicate that the effects of disease-associated substitutions on Tpm–Tn binding are position-dependent rather than phenotype-dependent.

5.13 Analysis of the effect of *TPM2* mutations on the actin polymerization kinetics

Spontaneous polymerization of G-actin is inhibited by Tpm, primarily through the stabilization of short actin oligomers and a subsequent reduction in the number of elongation-competent filament ends available for rapid growth (Hitchcock-DeGregori et al., 1988). The resulting Tpm-covered filaments are more stable, which can affect their stability during interactions with myosin.

To determine if the myopathy-associated variants alter kinetics of the thin filament assembly, the polymerization rates of pyrene-labeled G-actin in the absence and presence of Tpm2.2 variants were analyzed. The addition of wild-type Tpm2.2 at concentrations that saturate the formed filaments delayed G-actin polymerization (Figure 5.17), increasing the time required to reach half-maximal fluorescence ($t_{1/2}$) by approximately 28% (Table 5.7). While the presence of Tpm2.2 slightly reduced the cooperativity of the process as indicated by a lower Hill coefficient (α^H), the overall sigmoidal nature of the curve was maintained.

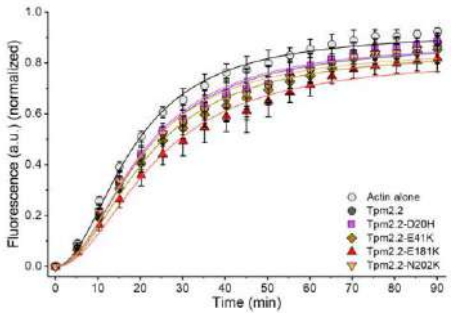

Figure 5.17 Influence of Tpm2.2 variants on the polymerization kinetics of pyrene-labeled G-actin. Polymerization time courses of 5 µM pyrene-G-actin in the absence (control) or presence of 2 µM Tpm2.2 variants. Experimental conditions: 20 mM Tris-HCl, pH 7.6, 100 mM KCl, 2 mM $MgCl_2$, 0.2 mM ATP, 0.1 mM Ca^{2+}, and 1 mM DTT. Data represent the mean ± SEM of four to five independent experiments. Solid lines represent fits to the Hill equation to determine the half-maximal polymerization time ($t_{1/2}$) and the cooperativity coefficient (α^H).

Compared to the wild-type Tpm2.2, most disease-causing substitutions exhibited no significant alterations in polymerization kinetics. A notable exception was the Tpm2.2-E181K variant, which further increased $t_{1/2}$ relative to the wild type, although the cooperativity of the assembly remained unaffected.

Table 5.7 Parameters of pyrene-actin polymerization in the presence of Tpm2.2 variants

	$t_{1/2}$	α^H
Actin alone	20.00 ± 0.46	1.62 ± 0.03
Tpm2.2	25.69 ± 1.07*	1.46 ± 0.04*
Tpm2.2-D20H	24.62 ± 0.94	1.49 ± 0.04
Tpm2.2-E41K	26.98 ± 0.87**	1.49 ± 0.02
Tpm2.2-E181K	31.45 ± 1.50$^{***\#}$	1.47 ± 0.03
Tpm2.2-N202K	25.32 ± 1.57*	1.45 ± 0.03*

The half-maximal polymerization time ($t_{1/2}$) and the Hill cooperativity coefficient (α^H) were derived from fits of polymerization time courses to Hill equation. Data represent mean values ± SEM from n=4–5 independent experiments. Statistical significance was determined using a One-Way ANOVA, Tukey post-hoc test; *** $p<0.001$, $^{**}0.001<p<0.01$, $^{*}0.01<p<0.05$ compared to polymerization of actin alone; $^{\#}0.01<p<0.05$ polymerization of 5 µM pyrene-labeled G-actin in the presence of Tpm2.2-E181K compared to Tpm2.2.

Thus, the delayed rate of G-actin polymerization characteristic of Tpm2.2 was largely preserved in the disease-associated variants. Among the mutations examined, only E181K further prolonged the polymerization process, suggesting that thin filament assembly may be selectively affected by specific mutations.

5.14 Analysis of the effect of *TPM2* mutations on the thin filament length

Since bulk polymerization assays do not provide data on individual filament length, a direct assay using fluorescence microscopy was employed to determine whether filaments assembled in the presence of wild-type or mutant Tpm2.2 exhibited differences in length. TRC-labeled F-actin, both unregulated and decorated with Tpm2.2 variants, was immobilized on lipid-coated coverslips for visualization. This immobilization strategy was chosen to minimize mechanical stress and fragmentation, which could otherwise distort the length distribution.

The length of unregulated actin filaments ranged from 5.3 to 6.4 µm, with an average of 5.95 ± 0.38 µm. While the average lengths of filaments decorated with wild-type or mutant Tpm2.2 showed minor variations compared to the unregulated control, these differences were not statistically significant (Figure 5.18 A). Consequently, these data indicate that while Tpm2.2 variants modulate the rate of actin polymerization, they do not influence the final steady-state filament length.

However, the presence of Tn + Ca^{2+} caused distinct, mutation-specific effects (Figure 5.18 B). Interestingly, the hypocontractile mutants tended to form longer filaments compared to the wild type. This effect was most pronounced in the N202K variant, which exhibited a statistically significant increase in average filament length. In contrast, the hypercontractile

variants resulted in the formation of shorter filaments. Specifically, the E181K variant showed a highly significant reduction in filament length compared to the wild-type.

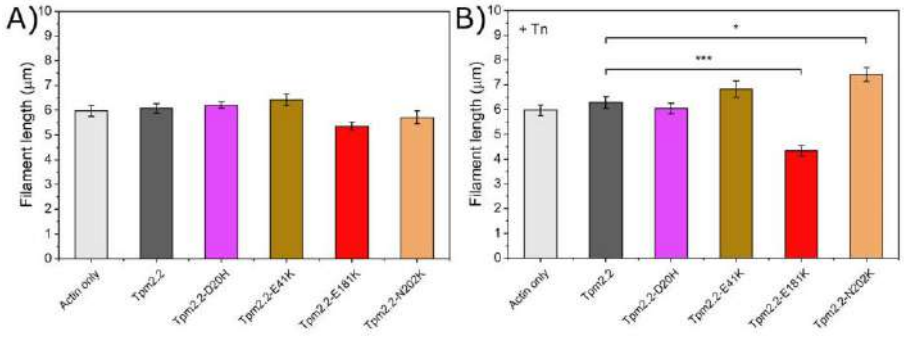

Figure 5.18 Length distribution of TRC-labeled F-actin. (A) The average filament lengths for actin decorated with Tpm2.2 variants and (B) in the presence of Tn +Ca^{2+}. Experimental conditions: 240 nM F-actin, 80 nM Tpm variants and 200 nM troponin + 0.1 mM $CaCl_2$ in 25 mM MOPS pH 7.4, 25 mM KCl, 4 mM $MgCl_2$, 1 mM EGTA, and 1 mM DTT. Data represent the mean ± SEM of four to five independent experiments. Statistical significance compared to wild-type Tpm2.2 was determined using Student's *t*-test: **0.001<p<0.01, *0.01 <p<0.05.

Despite their effects on actin polymerization kinetics, the Tpm2.2 variants did not alter steady-state filament length in the absence of Tn. However, in the presence of the Tn+Ca^{2+}, the mutations produced distinct, phenotype-dependent changes in filament length.

5.15 Effects of mutations in *TPM2* on the thin filament length regulation by Tpm2.2 and Tn under mechanical load

While measurements on lipid surfaces established the baseline steady-state lengths of the filaments, they did not account for the dynamic physiological environment of muscle. Therefore, the structural integrity of thin filaments under the mechanical load generated by myosin cross-bridge interactions was subsequently examined. To assess filament stability under load, the resistance of F-actin to shorten under stress imposed by both rigor binding and active cross-bridge cycling was evaluated using fluorescence microscopy. TRC-labeled filaments were attached to HMM-coated coverslips, and changes in filament length were measured as an indicator of filament stability.

Initially, filaments were bound to myosin heads in the absence of ATP, subjecting them to the high-force stress of the rigor state. A comparison of filament lengths on HMM (Figure 5.19) versus lipid surfaces (Figure 5.18) revealed that rigor binding had no significant impact on the length of unregulated or filaments coated with wild-type Tpm2.2.

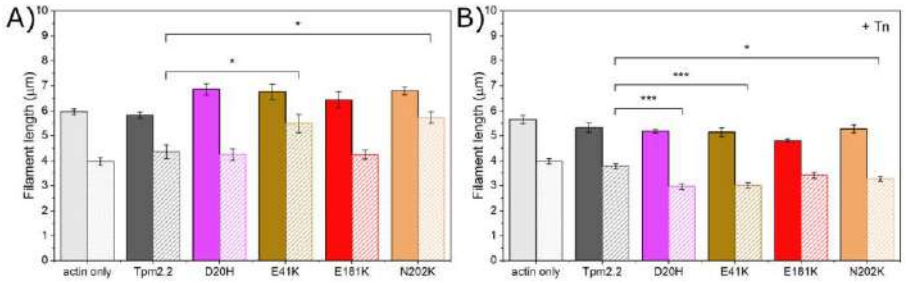

Figure 5.19 Influence of Tpm2.2 variants on thin filament length under HMM-induced mechanical load. Average lengths of TRC-labeled F-actin decorated with Tpm2.2 variants were measured before and after the addition of ATP in the (A) absence of regulatory proteins, (B) presence of the Tn+Ca^{2+}. Measurements were obtained in the rigor state (solid bars) and 30 s after the initiation of actomyosin sliding via ATP addition (striped bars). Conditions: Protein concentration: 0.1 mg/mL heavy meromyosin (HMM), 100 nM F-actin, 34 nM Tpm variants and 50 nM Tn in 25 mM MOPS pH 7.4, 25 mM KCl, 4 mM $MgCl_2$, 1 mM EGTA, and 1 mM DTT. Data represent the mean ± SEM of four to five independent experiments. Statistical significance compared to wild-type Tpm2.2 was determined using a Welch's ANOVA, Games-Howell Post-Hoc test; *** $p<0.001$, **$0.001<p<0.01$, *$0.01<p<0.05$.

Whereas filaments decorated with Tpm2.2 mutants appeared slightly longer, these differences were not statistically significant (Figure 5.19 A, solid bars). Similarly, as compared to the presence of Tpm2.2, incorporation of the Tn + Ca^{2+} did not alter thin filament lengths prior to the initiation of actomyosin interaction (Figure 5.19 B, solid bars).

The addition of ATP induced active cross-bridge cycling, subjecting the thin filaments to dynamic, myosin-generated longitudinal forces. Following ATP introduction, this mechanical strain induced a pronounced destabilization and subsequent shortening across nearly all filament populations. Notably, the hypocontractile variants showed resistance to this force-induced shortening and maintaining significantly longer filaments as compared to wild-type Tpm2.2.

Following the introduction of ATP in the presence of the Tpm2.2–Tn +Ca^{2+}, all filaments formed in the presence of Tpm2.2 mutants exhibited significantly shorter average lengths post-ATP compared to the wild-type Tpm2.2 control filaments. This pronounced filament shortening directly correlates with previously observed kinetics of actin-myosin interactions. Specifically, the hypercontractile Tpm2.2 variants, which show the most drastic reduction in filament length under load, demonstrated a significantly elevated actomyosin ATPase rate. **This indicates that an accelerated rate of cross-bridge cycling and the resulting high mechanical turnover directly compromise the structural stability of the regulated thin filament.**

5.16 Regulation of the thin filament length by Tmod1

Because Tmod1, the pointed-end capping protein, binds actin with high affinity only when stabilized by Tpm (Colpan et al., 2013), we next asked whether Tmod1-mediated capping could protect filaments from force-induced disassembly and whether the Tpm2.2 variants compromise this localized protective mechanism.

When Tmod1 was bound alongside the Tpm2.2 variants, filament lengths remained predominantly stable prior to ATP addition. The sole exception was the hypocontractile Tpm2.2-N202K variant, which produced significantly longer filaments compared to the wild-type Tpm2.2 control. Upon ATP-driven initiation of actin-myosin interactions, a general reduction in filament lengths was observed. The extent of filament shortening did not differ significantly between bare actin, wild-type Tpm2.2, or any of the investigated mutant variants (Figure 5.20 A).

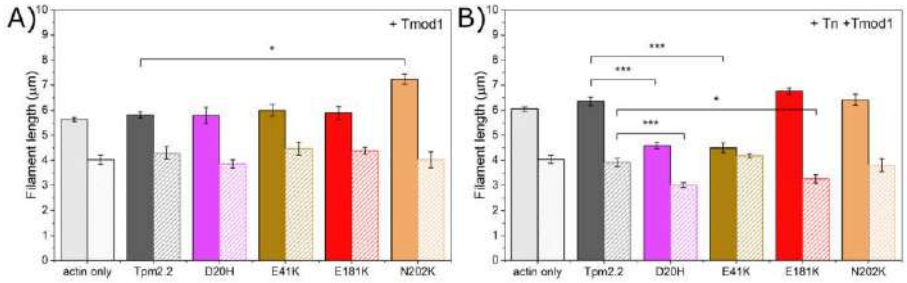

Figure 5.20 Influence of Tpm2.2 variants on the length of Tmod1-capped thin filaments under HMM-induced mechanical load. Average lengths of TRC-labeled F-actin decorated with Tpm2.2 variants were measured before and after the addition of ATP in (A) the presence of Tmod1, and (B) Tmod1 together with the Tn+Ca^2. Measurements were obtained in the rigor state (solid bars) and 30 s after the initiation of actomyosin sliding via ATP addition (striped bars). Conditions as in Figure 5.19 caption. Data represent the mean ± SEM of four to five independent experiments. Statistical significance compared to wild-type Tpm2.2 was determined using a Welch's ANOVA, Games-Howell Post-Hoc test; *** $p<0.001$, *$0.01 <p<0.05$.

The most striking phenotypic differences emerged when filaments were fully reconstituted with both the Tpm2.2–Tn regulatory complex and Tmod1. Before ATP introduction, mutations in the N-terminal actin-binding period P1 resulted in significantly shorter initial filaments, indicating a structural defect in filament stability. In contrast, mutations within the internal P5 region showed no difference, maintaining filament length that were similar to the wild-type Tpm2.2 (Figure 5.20 B, solid bars).

Following ATP-induced actomyosin activation, the hypercontractile mutant filaments showed significantly shorter average lengths, unlike the hypocontractile variants, which did not significantly differ from wild type (Figure 5.20 B, stripe bars).

Overall, these findings demonstrate that the Tn complex and Tmod1 act in synergy to modulate filament stability, and that myopathy-linked mutations in Tpm2.2 differentially disrupt this protective mechanism based on their spatial positioning along the actin filament.

5.17 Analysis of Tmod1 affinity to F-actin in the presence of Tpm2.2 variants

To understand the molecular mechanism behind the differences in the filament length in the presence of Tmod1 (Figure 5.20), direct effects of the mutations on Tmod1 binding to actin were investigated. Western blot analysis was utilized to monitor the steady-state Tmod1 interactions with F-actin in the presence of each Tpm2.2 variant with and without Tn, which allowed to correlate the filament stability with physical protein-protein interactions.

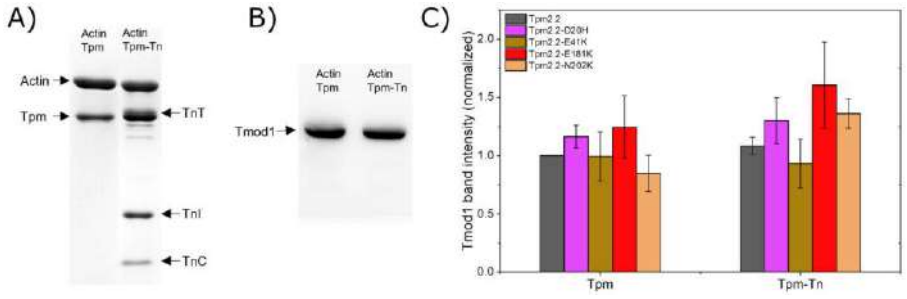

Figure 5.21 Analysis of Tmod1 protein levels bound to F-actin variants. (A) Coomassie stained SDS-PAGE of proteins collected in the pellet fraction. (B) Representative Western blot showing Tmod1 detected using a specific anti-Tmod1 primary antibody. (C) Quantification of Tmod1 band intensities obtained by densitometric analysis of the Western blot signals normalized to the Tmod1 intensity in the presence of wild-type Tpm2.2. Experimental conditions: 5 μM actin, 2 μM Tpm2.2 variants, a 2-fold molar excess of Tn relative to Tpm, and 10 nM Tmod1. The assay was performed in 20 mM Tris-HCl, pH 7.6, 100 mM KCl, 2 mM $MgCl_2$, 0.2 mM ATP, 0.5 mM DTT, and 0.1 mM $CaCl_2$. Data represent the mean ± SEM of three independent experiments.

As illustrated in Figure 5.21 B, Tmod1 bound efficiently to the thin filaments under the experimental conditions. Densitometric quantification of the Western blot membranes was performed by normalizing Tmod1 band intensities in the presence of Tpm2.2 mutants to the intensities in the presence of wild-type Tpm2.2 control (Figure 5.21 C). Across all experimental conditions, the individual Tpm2.2 variants exhibited only minor variations in Tmod1 binding. None of differences reached statistical significance.

Therefore, Tmod1 binding to the pointed end of the thin filament is unaffected by either the Tpm2.2 mutations or the presence of Tn and Ca^{2+}.

5.18 Analysis of the effect of *TPM2* mutations on the affinity of Cof2 to F-actin in the reconstituted thin filament

A comprehensive understanding of thin filament regulation requires evaluating the mechanisms governing filament disassembly. Since cofilin is an actin-depolymerizing protein responsible for filament length maintenance and turnover, effects of myopathy-linked Tpm2.2 variants on modulation of Cof2 activity was analyzed. First, Tpm2.2 and Tn-dependent changes in Cof2 affinity for actin were evaluated.

A cosedimentation assay was used to determine whether the myopathy-associated variants alter the Tpm2.2-mediated regulation of Cof2 binding. Following separation of the pellet and supernatant fractions on SDS-PAGE, the actin-bound proteins were quantified via densitometric analysis (Figure 5.22). The presence of wild-type Tpm2.2 slightly but significantly decreased the binding affinity of Cof2 for F-actin compared to unregulated filaments (Table 5.8)

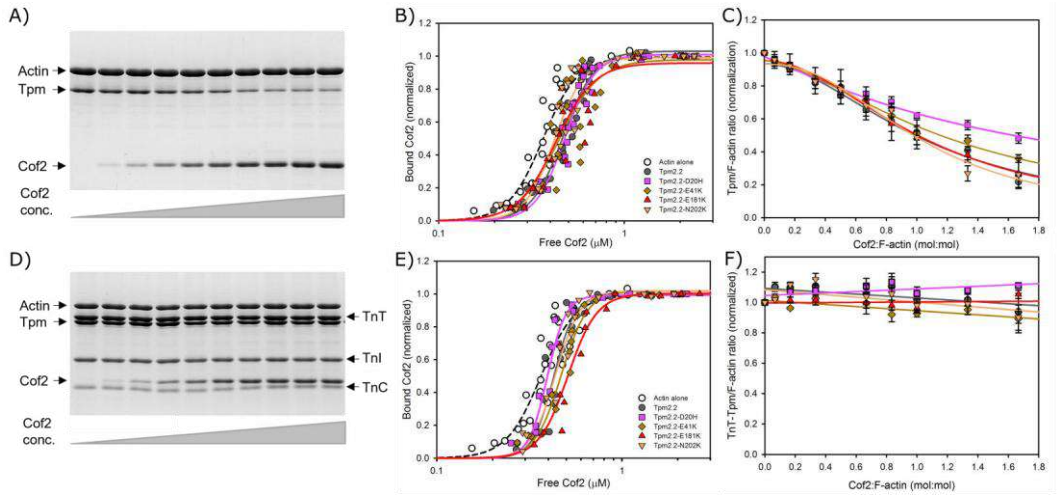

Figure 5.22 Impact of Tpm2.2 variants and Tn on Cof2 binding to F-actin. (A) SDS-PAGE of proteins collected in pellets after ultracentrifugation of F-actin-Tm2.2 complexes with increasing Cof2 concentrations. (B) Equilibrium binding of Cof2 to F-actin in the presence of Tpm2.2 variants. (C) Competitive displacement of Tpm2.2 variants from F-actin by increasing concentrations of Cof2. (D) SDS-PAGE of proteins collected in pellets after ultracentrifugation of F-actin-Tm2.2-Tn complexes with increasing Cof2 concentrations. (E) Binding of Cof2 to F-actin regulated by the Tpm2.2–Tn complex in the presence of Ca^{2+}. (F) Dissociation of the Tpm2.2–Tn regulatory complex from actin filaments by increased binding of Cof2 to actin. Conditions: 3 μM actin, 0.75 μM Tpms and increasing concentration of Cof2 in 5mM Tris-HCl pH 7.6, 100mM NaCl, 2 mM $MgCl_2$, 1 mM DTT. Data represent the mean ± SEM of three independent experiments.

When comparing the Tpm2.2 variants, the majority of the disease-causing substitutions did not significantly alter the binding of Cof2 to the filament except for the Tpm2.2-N202K variant, which exhibited the weakest inhibitory effect on Cof2 binding compared to those decorated with the wild-type Tpm2.2 (Table 5.8). Furthermore, the cooperativity of the binding process, as indicated by the Hill coefficient (α^H), remained the same across variants, suggesting

that while the mutations may alter local binding affinity, they do not fundamentally disrupt the cofilin-mediated remodeling of the actin filament.

To investigate the stability of the Tpm-actin interface, we analyzed the ability of Cof2 to competitively displace Tpm2.2 variants from the filament. Increasing the fractional occupancy of Cof2 resulted in the partial dissociation of all Tpm2.2 variants from F-actin (Figure 5.22 C). At saturating concentrations of Cof2, only 20–50% of the initial Tpm2.2 remained filament-associated, indicating a significant remodeling of the thin filament. Among the variants, Tpm2.2-D20H exhibited the highest resistance to Cof2-induced dissociation. At the maximal concentration tested (Cof2:F-actin molar ratio of 1.7:1), the filament occupancy of the D20H variant was significantly higher than wild-type Tpm2.2. This suggests that the D20H substitution stabilizes the Tpm2.2–actin interaction or sterically hinders the conformational changes in actin required for Cof2-mediated displacement.

Table 5.8 Binding parameters of Cof2 to F-actin regulated by Tpm2.2 variants and the Tn complex

	−Tn		**+Tn (+Ca^{2+})**	
	K_{app} [μM^{-1}]	**α^H**	**K_{app} [μM^{-1}]**	**α^H**
F-actin	2.74 ± 0.10	4.66 ± 0.83		
F-actin-Tpm2.2	2.13 ± 0.05$^{\#\#}$	5.08 ± 0.61	2.33 ± 0.06	7.67 ± 1.59
F-actin-Tpm2.2-D20H	2.09 ± 0.04	5.47 ± 0.69	2.53 ± 0.04*	8.66 ± 1.33
F-actin-Tpm2.2-E41K	2.25 ± 0.14	4.05 ± 1.08	2.12 ± 0.04*	6.15 ± 0.81
F-actin-Tpm2.2-E181K	2.34 ± 0.11	4.25 ± 0.93	1.96 ± 0.08**	5.54 ± 1.32
F-actin-Tpm2.2-N202K	2.37 ± 0.07*	5.46 ± 0.92	2.28 ± 0.06	6.52 ± 0.98

K_{app} and α^H values obtained from the parameters of the experimental fit to Hill equation ± SEM. Statistical significance was evaluated using a two-tailed t-test. Symbols indicate significance levels (** $0.001<p<0.01$, * $0.01<p<0.05$) either relative to the wild-type Tpm2.2 control or to unregulated F-actin ($^{\#\#}$ $p<0.01$). Experimental conditions were as described in Figure 5.22.

Next, the interaction between Cof2 and the fully regulated thin filament (Tpm2.2–Tn in the presence of Ca^{2+}) was analyzed (Figure 5.22 E). Under these conditions, Cof2 exhibited a binding affinity comparable to that observed in the absence of Tn; however, the binding process showed a marked increase in cooperativity (Table 5.8). The disease-causing variants exerted more variable effects in this regulatory system, resulting in minor but statistically significant shifts in Cof2 affinity for the actin filament (Table 5.8).

Notably, the Tn complex protected the Tpm2.2 variants from competitive displacement from the filament by Cof2 (Figure 5.22 F), in contrast to experiments performed in the absence of Tn (Figure 5.22 C). As evident from the SDS gels, in the absence of Tn, increasing Cof2

occupancy was accompanied by progressive loss of Tpm2.2 from the filament. When Tn was present, Cof2, Tpm2.2, and Tn remained simultaneously associated with actin. These findings suggest that incorporation of the Tn complex markedly stabilizes the Tpm2.2–actin interface.

Overall, disease-associated Tpm2.2 variants had only modest effects on Cof2 binding to actin, with N202K showing the weakest inhibition of Cof2 binding and D20H exhibiting the greatest resistance to Cof2-mediated displacement from the filament. In contrast, incorporation of the Tn complex markedly stabilized the Tpm2.2–actin interface, preventing Tpm2.2 dissociation even at high Cof2 occupancy. Thus, regulation of Cof2-mediated thin filament remodeling depends on the presence of the Tn complex rather than on the disease-associated Tpm2.2 substitutions.

5.19 Assessment of the effects of disease-linked mutations in *TPM2* on Cof2-mediated regulation of actin filament length, severing and depolymerization

Following the biochemical determination of protein binding profiles, next the direct impact of Tpm2.2 variants on the cofilin-mediated severing and disassembly of regulated and unregulated thin filaments was examined. Filament shortening was quantified by direct measurement of filament lengths using epifluorescence microscopy. TRC-labeled F-actin filaments, decorated with Tpm2.2 variants, in the absence and presence of Tn and Tmod1, were immobilized on lipid bilayer-coated coverslips. This method of surface attachment was specifically chosen to minimize longitudinal mechanical stress, ensuring that observed changes in filament length was primarily driven by Cof2-dependent remodeling rather than mechanical load.

Upon introduction of Cof2, filaments underwent rapid structural destabilization, resulting in fragmentation. Severing events were evidenced by the appearance of distinct gaps along the longitudinal axis of the filaments (Figure 5.23 A, indicated by yellow arrowheads). When wild-type Tpm2.2 alone was present on the actin, it did not protect the filaments from being severed by Cof2. Instead, the filaments behaved like bare actin, leaving the filaments at the same length (Figure 5.23 B). Surprisingly, the hypocontractile mutants showed protective capacity, keeping the filaments significantly longer than the wild type, and this protective effect grew stronger over time. The hypercontractile mutants, however, behaved just like the wild-type (Figure 5.23 B).

The presence of Tn $+Ca^{2+}$ protected the filaments from being severed and depolymerized over time, but the Tpm2.2 variants showed different regulatory abilities. The

hypercontractile Tpm2.2-E181K variant provided much weaker protection, meaning its filaments were easily severed by Cof2. On the other hand, the presence of the hypocontractile Tpm2.2-N202K variant maintained longer filaments compared to wild type. All the other mutations behaved similarly to wild type (Figure 5.23 C).

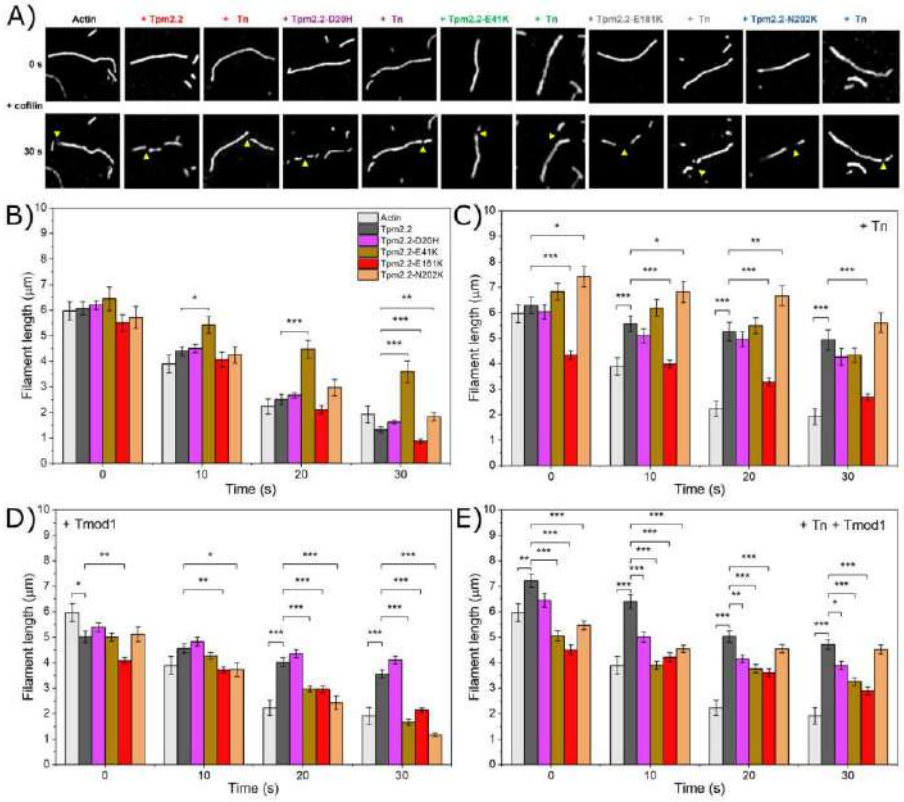

Figure 5.23 Regulation of Cof2-dependent severing and depolymerization by Tpm2.2 variants. (A) Fluorescence microscopy images of TRC-labeled F-actin before and 30 seconds after exposure to Cof2. Yellow arrowheads indicate representative severing sites. Cof2-dependent changes in filament length in the (B) absence of Tn, (C) presence of Tn, (D) presence of Tmod1 alone, and (E) simultaneous presence of both Tn and Tmod1. Severing/depolymerization was started by addition of 240 nM Cof2 to the flow cells. Experimental conditions consisted of 240 nM TRC-labeled thin filaments, 80 nM Tpm2.2 variants, 200 nM Tn, and 4 nM Tmod1 in assay buffer supplemented with 0.1 mM $CaCl_2$. Data represent the mean ± SEM of three independent experiments. Statistical significance compared to wild-type Tpm2.2 was determined using Welch's ANOVA followed by the Games–Howell post hoc test (*0.01 < p < 0.05, **0.001 < p < 0.01, ***p < 0.001).

When the filaments were capped with Tmod1, filaments decorated with wild-type Tpm2.2 were longer than bare actin. However, Tpm2.2 variants showed distinct differences under these conditions. While Tpm2.2-D20H mirrored the wild-type's protective effect, the other mutations completely lost this protection and after 30 seconds the result resembled bare actin (Figure 5.23 D). Interestingly, this outcome directly opposes the results from the Tpm-only assays, where the hypocontractile variants demonstrated a protective behavior. This suggests that the mutation-dependent structural changes in Tpm may differently affect activities of various actin-binding proteins.

The presence of both Tpm2.2-Tn and Tmod1 (Figure 5.23 E) exerted a protective effect that was similar to that observed in the absence of Tmod1 (Figure 5.22 C). Except for Tpm2.2-N202K, all mutants destabilized the filaments allowing Cof2 to produce shorter filaments.

Taken together, these results demonstrate that myopathy-associated mutations in Tpm2.2 disrupt the delicate structural equilibrium of the thin filament, leaving the filament lattice vulnerable to Cof2-driven severing and depolymerization of the thin filament.

5.20 Influence of Tmod1 on binding of Cof2 to actin-Tpm2.2

Thin-filament length analysis indicated that Tmod1 partially counteracted Cof2-mediated depolymerization, stabilizing the filaments in the presence of wild-type Tpm2.2 (Figure 5.23 D). This effect could be caused by a decrease in the affinity of Cof2 on Tpm2.2-decorated F-actin in the presence of Tmod1. To test this hypothesis, binding of Cof2 to F-actin-Tpm2.2 at different Tmod1 concentrations was analyzed by cosedimentation assay.

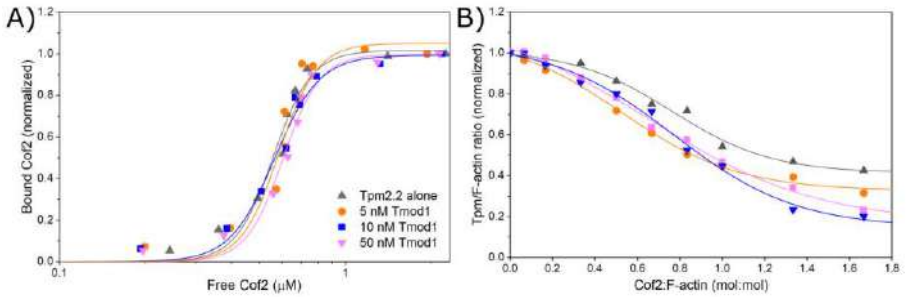

Figure 5.24 Tmod1-dependent regulation of Cof2 binding to F-actin and Tpm2.2 dissociation. (A) Binding of Cof2 to F-actin in the presence of Tpm2.2 at increasing concentrations of Tmod1. (B) Competitive displacement of Tpm2.2 from Tmod1-capped F-actin by increasing concentrations of Cof2. Conditions: 3 μM actin, 0.75 μM Tpm2.2, 5, 10, 50 nM of Tmod1 and increasing concentration of Cof2 in 5 mM Tris-HCl pH 7.6, 100 mM NaCl, 2 mM MgCl2, 1 mM DTT.

Following SDS-PAGE separation of the pellet and supernatant fractions, the actin-bound proteins were quantified via densitometric analysis, which showed that as compared to Tpm2.2 alone, the presence of Tmod1 at increasing concentrations did not change neither affinity nor cooperativity of Cof2 binding to actin (Figure 5.24 A). In addition, densitometric analysis of Tpm2.2/F-actin ratio in pellets revealed that in the presence of Tmod1, Cof2 displaced Tpm2.2 from the filament even more efficiently than without Tmod1 (Figure 5.24 B), showing that Tpm2.2-Tmod1 interactions at the pointed end did not stabilize Tpm2.2 chains along the filament.

Therefore, the decreased susceptibility of the filament to Cof2-mediated depolymerization in the presence of Tmod1 is more likely attributable to a steric mechanism, such as a Tmod1-induced shift in Tpm2.2 position on the filament, than to changes in Cof2 affinity caused by Tmod1.

6 Discussion

As a molecule coating actin along both sides of the filament, Tpm is in a position to control access of all actin-binding proteins to the filament. For this reason, it has been appropriately termed a "gatekeeper" of the actin filament (Dominguez, 2011). Tpm does not function merely as a rigid steric blocker but actively participates in the diverse range of cellular processes involving actin in both muscle and non-muscle cells (P. Gunning et al., 2008). In skeletal muscle, Tpm works closely with Tn to confer Ca^{2+} sensitivity on the regulatory system controlling actin–myosin interactions. However, it remains unclear which regions of the Tpm coiled-coil contribute to specific regulatory mechanisms. In addition, little is known about structural determinants in Tpm important for regulation of the thin filament length and dynamics in muscle.

The main goal of this dissertation was to elucidate the structure–function relationships within two actin-binding regions of Tpm2.2, periods P1 and P5. By executing five specific objectives, I demonstrated that structural changes in these regions caused by single amino acid substitutions can profoundly affect Ca^{2+}-dependent regulation of actin–myosin interactions and myosin motor function. My data strongly suggests that these alterations are the major molecular mechanism underlying the muscle dysfunction observed in patients with congenital myopathy and arthrogryposis. I also demonstrated that periods P1 and P5 contribute to the regulation of thin-filament length and the dynamic balance between actin polymerization and depolymerization, providing an additional mechanism that may contribute to the clinical phenotypes associated with these mutations. Overall, the findings of this dissertation advance our understanding of both the physiological mechanisms governing thin-filament function and the molecular basis of *TPM2*-related muscle diseases.

6.1 Role of P1 and P5 in Tpm2.2 actin binding

Tpm performs its canonical role on the thin filament by binding along actin through a series of periodic actin-binding repeats (McLachlan & Stewart, 1976; Phillips, 1986). Missense mutations located within these actin-binding regions often alter the affinity of Tpm for actin (Barua et al., 2011). Because Tpm–actin affinity influences the equilibrium between the blocked, closed, and open states of the thin filament, even small changes at the Tpm-actin interface can lead to either increased or decreased contractile activity (McKillop & Geeves, 1993; Vibert et al., 1997; Lehman et al., 2000).

As both hypercontractile substitutions, D20H and E181K reverse the local charge within the actin-binding consensus sites, they were predicted to disrupt the ionic contacts that wild-type Tpm2.2 normally forms with a cluster of basic actin residues, K326, K328, and R147 (X. (Edward) Li et al., 2011). Consistent with a partial loss of this interaction, the homologous substitution E181K introduced into the Tpm1.1 isoform was previously reported to modestly increase the dissociation constant for actin (Gupte et al., 2015); no equivalent data existed for D20H prior to this work. Computational predictions in which both D20 and E181 were included, showed that in Tpm1.1 D20 and E181side chains form strong, favorable interactions with actin, such that mutations at these positions would be expected to reduce the affinity of Tpm for actin (Orzechowski et al., 2014). However, in the bulk co-sedimentation assay performed here, neither Tpm2.2-D20H nor Tpm2.2-E181K exhibited a significant difference in overall actin binding in the absence or the presence of Tn, regardless of Ca^{2+}, compared with wild-type Tpm2.2. This may indicate that in Tpm2.2 actin interactions of these two residues may be different than in Tpm1.1.

The FRET measurements resolved this difference: the charge reversal at these positions shifted Tpm2.2-D20H and Tpm2.2-E181K to a greater distance from actin SD1 compared to wild-type Tpm2.2, without a corresponding change in binding affinity. Taken together, these results suggest that the two hypercontractile mutants occupy the filament with essentially wild-type affinity, but from an altered position, one that, as discussed below, is sufficient to change their regulatory relationship with the myosin motor even though the actin-binding step itself is preserved.

The hypocontractile substitutions exhibited a similar behavior, with neither Tpm2.2-E41K nor Tpm2.2-N202K producing a significant change in actin affinity relative to wild-type Tpm2.2, either in the absence or presence of Tn and irrespective of Ca^{2+} concentration. These findings are consistent with previous reports on the corresponding mutations (Marttila et al., 2012; Bershitsky et al., 2019). Unlike the hypercontractile mutants, neither E41K nor N202K produced a detectable change in the FRET-based distance between Tpm2.2 and the actin filament. Together, these observations indicate that E41 and N202 — both located in the second halves of actin-binding periods P1 and P5 — do not themselves form part of the Tpm2.2–actin binding interface, and that the hypocontractile phenotype associated with these substitutions must therefore originate downstream of, or independently from, the actin-binding step itself.

Alignment of the sequences encompassing three coiled-coil periods of the skeletal muscle Tpm paralogs Tpm1.1, Tpm2.2, and Tpm3.12, which contain the disease-causing

substitutions, reveals a high degree of amino acid conservation (Figure 6.1). The most highly conserved region is the first half of P1, containing D20, where Tpm2.2 differs from the other two paralogs by only a single conservative I→L substitution. The remaining three regions are more variable, particularly second half of P1 surrounding E41, which in Tpm1.1 and Tpm3.12 is replaced by D41. Moreover, in all three regions, the immediate amino acid environment contains additional non-conservative substitutions.

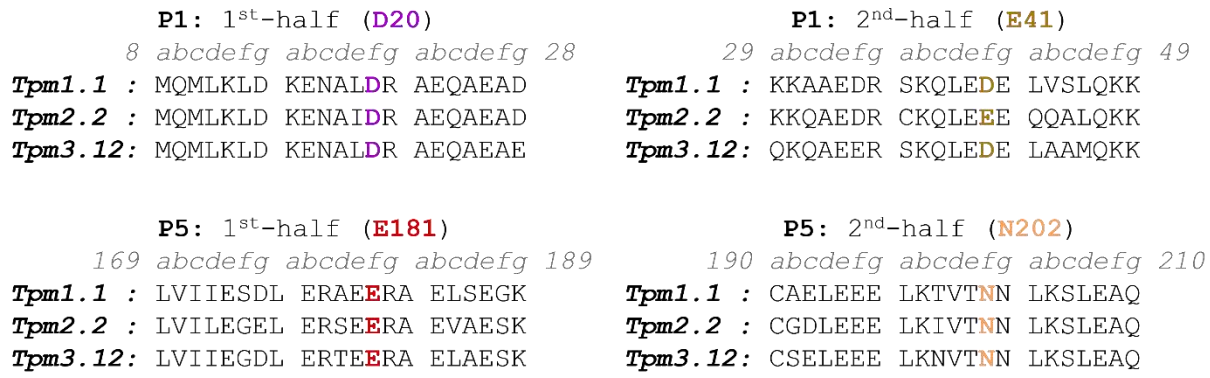

Figure 6.1 Multiple sequence alignment of Tpm regions surrounding *TPM2* myopathy-associated variant sites. Amino-acid sequences of human Tpm1.1 (NP_001018005.1), Tpm2.2 (NP_003280.2), and Tpm3.12 (NP_689476.2) were aligned using the Clustal Omega multiple sequence alignment tool (EMBL–EBI). Shown are 21-residue regions encompassing 12 residues N-terminal and 8 residues C-terminal to each Tpm2.2 variant position: D20, E41, E181, and N202. The corresponding residues in Tpm2.2 are shown in bold.

These sequence differences may modulate the Tpm–actin interface and contribute to the distinct modes by which individual Tpm paralogs interact with the actin filament. This hypothesis requires further verification, preferably through high-resolution structural analyses, to determine how these substitutions influence the conformation of Tpm2.2 and its intermolecular interactions.

Overall, the actin-binding analyses and the structural part of this study indicates that hypercontractile substitutions in the N-terminal halves of P1 and P5 perturb the positioning of Tpm2.2 on the filament without weakening bulk binding, whereas hypocontractile substitutions in the C-terminal halves leave both affinity and closed-state geometry essentially unchanged.

6.2 Myosin-induced Tpm movement and open-state perturbations

Conserved residues located in the C-terminal portions are essential for actomyosin regulation (Barua et al., 2012). Structural studies of the M-state (open state) of the thin filament have shown that residues in the N-terminal portions of the actin-binding periods can directly interact with myosin loop 4 (Behrmann et al., 2012; Doran et al., 2020; Z. Wang et al., 2021). Together, these findings provide a structural framework for interpreting the actin-binding

properties of the D20H, E181K, E41K, and N202K variants in the presence of myosin heads bound in rigor state.

Binding of myosin S1 to actin induces a positional shift of Tpm along the thin filament (Vibert et al., 1997; Behrmann et al., 2012; Doran et al., 2020). This movement is required for the cooperative transition of the thin filament from the closed to the open activation state (Vibert et al., 1997). Effects of the mutation on this activation step were analyzed by following S1-induced pyrene excimer fluorescence. Because the excimer arises from interactions between pyrenes at Cys36 and Cys190 positioned in P1 and P5, changes in excimer amplitude reported mutation-dependent alterations in Tpm2.2 orientation in the rigor/open state. All mutations, except of E41K, altered the amplitude of the S1-induced change in excimer fluorescence, indicating that both hyper- and hypocontractile variants (with the exception of E41K) modify Tpm2.2 orientation when myosin engages the filament.

The S1/actin ratio required to achieve the fully open state was generally increased for all mutants, with the highest ratio required for mutations in P5, consistent with prior evidence that P5 is particularly important for myosin–Tpm contacts and for stabilizing the open state (Hitchcock-DeGregori et al., 2002). These results suggest that even though the second halves of P1 and P5 minimally influence actin affinity in the closed state, they significantly contribute to the myosin-dependent transition to the open state, likely through subtle changes in the Tpm–myosin–actin interface that are not fully resolved in cryo-EM models (Behrmann et al., 2012; von der Ecken et al., 2015; Fujii & Namba, 2017; Doran et al., 2020). Notably, the lack of a clear correlation between the magnitude of excimer changes and clinical phenotype underscores that hyper- versus hypocontractility cannot be inferred from static structural perturbations alone, but must be interpreted in the context of the full kinetic cycle.

6.3 Regulation of cross-bridge kinetics and ATP turnover

The central regulatory function of Tpm is to restrict myosin access to actin and thereby modulate both actomyosin cross-bridge cycle and myosin ATPase activity (Gordon et al., 2000). Results of the steady-state ATPase measurements and single-turnover kinetics were consistently showing that the four *TPM2* mutations diverge into two functional classes not only in the muscle of affected patients, but also *in vitro* on the protein level. The hypocontractile substitutions, located in the second halves of P1 and P5, enhance the inhibitory effect of Tpm2.2–Tn on the actin-activated ATPase by slowing product (ADP/Pi) release, whereas the

hypercontractile substitutions in the first halves accelerate product release and increase ATP turnover relative to wild-type Tpm2.2.

Single-turnover experiments demonstrate that these mutation-specific changes in inhibitory potential map directly onto the kinetics of the product-release step, consistent with previous work indicating that Tpm-dependent regulation of thin filaments is realized mainly by tuning the rate of ADP and Pi release rather than by large changes in myosin binding equilibrium constants (Lionne et al., 1995; Heeley et al., 2002, 2006; Muthu et al., 2008). Because myosin heads interact with both actin and Tpm in the strongly bound rigor states, the altered product release kinetics likely arise from mutation-dependent changes in contacts between myosin loop 4 and Tpm along the filament (Behrmann et al., 2012; Doran et al., 2020). Thus, data from kinetic experiments support a model in which substitutions in either half of P1 and P5 can shift the balance between inhibited and activated states, but in opposite directions, depending on whether they stabilize the blocked/closed states (hypocontractile) or facilitate escape into the open state (hypercontractile).

Temperature-dependent ATPase measurements reveal an additional layer of mechanistic detail, particularly for the E181K hypercontractile variant. While D20H consistently activated the actomyosin ATPase across 20–30°C, E181K showed reduced activation within this range compared with wild-type Tpm2.2, despite hypercontractile phenotype observed in motility assay, which is further discussed below. Arrhenius analysis indicated that E181K raises the activation energy of the overall ATPase reaction by about 21 kJ/mol, suggesting that the mutation imposes a higher enthalpic barrier on the rate-limiting step of the cross-bridge cycle. As a consequence, the hypercontractile phenotype of E181K becomes fully manifested only at or above physiological temperature (≥33°C), where thermal energy is sufficient to drive the closed-to-open transition more readily despite the increased enthalpic barrier. These findings resonate with earlier studies showing that temperature can activate fast skeletal thin filaments by promoting dissociation or destabilization of the Tpm–Tn complex and thereby favoring the open state (Ishiwata, 1978; S. Ishii et al., 2023). In the case of E181K, the elevated enthalpic barrier appears to shift the temperature window at which the thin filament becomes fully responsive to Ca^{2+}, providing a plausible explanation for the discrepancy between ATPase data at sub-physiological temperatures and hypercontractile behavior observed in patient muscle fibers (Ochala et al., 2012). This highlights that the pathogenic impact of *TPM2* mutations cannot be fully evaluated without considering the physiological temperature range in which skeletal muscle operates.

Missense mutations in Tpm genes expressed in cardiac and skeletal muscle frequently alter Ca^{2+} sensitivity of thin-filament activation, thereby modifying the efficacy of cross-bridge recruitment at intermediate Ca^{2+} concentrations (Tajsharghi et al., 2012; Redwood & Robinson, 2013; Moraczewska, 2020). A general trend has emerged in which hypercontractile phenotypes correlate with increased Ca^{2+} sensitivity, whereas hypocontractile phenotypes correlate with decreased sensitivity, although exceptions exist (Bershitsky et al., 2019; Moraczewska, 2020). Some mutations in *TPM2* increase calcium sensitivity and produce a hypercontractile phenotype, meaning that the thin filament becomes activated at lower calcium concentrations than normal. Hypercontractile mutations may increase basal thin filament activation and contribute to congenital contractures, distal arthrogryposis, trismus, or other limitation of joint movement. Examples of hypercontractile or gain-of-function *TPM2* mutations include p.K7del, p.R91G, p.Lys49del, p.E139del, and p.E181K (Marston et al., 2013; Marttila et al., 2014). The ATPase measurements across Ca^{2+} titrations are consistent with those patterns: Tpm2.2-D20H and E181K variants shift the Ca^{2+} dependence toward higher sensitivity, while Tpm2.2-E41K and N202K variants reduce Ca^{2+} sensitivity relative to wild-type Tpm2.2. These observations are in agreement with previous studies on Tpm2.2-E41K and N202K, which also reported decreased Ca^{2+} sensitivity and reduced velocities for hypocontractile *TPM2* variants (Marttila et al., 2012; Bershitsky et al., 2019).

Together, the available data support a model in which conserved residues in the N- and C-terminal halves of P1 and P5 constitute critical determinants of the Ca^{2+}-dependent equilibrium between blocked, closed, and open states.

6.4 Regulation of filament motility propelled by myosin heads

In vitro motility assays provided a more physiological readout of myosin motor performance by constraining myosin heads in a high-density, surface-bound arrangement and tracking the sliding of actin filaments. In agreement with the ATPase data and clinical phenotypes of *TPM2*-related myopathies (Marttila et al., 2012; Tajsharghi et al., 2012; Bershitsky et al., 2019), hypercontractile variants (Tpm2.2-D20H and E181K) increased actin sliding velocities by approximately 30–50% relative to wild-type Tpm2.2, whereas hypocontractile variants (Tpm2.2-E41K and N202K) reduced velocities to about one-third of wild-type values and dramatically increased the fraction of immotile filaments. In the presence of Tn and activating Ca^{2+}, these trends persisted: hypercontractile variants further promoted sliding, while hypocontractile variants suppressed both velocity and the fraction of motile

filaments, indicating that the mutations' functional signatures are retained within the reconstituted regulatory environment.

Interestingly, Tn +Ca^{2+} exerted distinct rescuing effects on the two hypocontractile variants. For E41K, inclusion of Tn reduced the fraction of immotile filaments to near wild-type levels, suggesting that the regulatory complex can stabilize an activated state despite the mutation and partially restore productive cross-bridge cycling. In contrast, Tpm2.2-N202K filaments remained largely immotile even with Tn +Ca^{2+}, implying a more profound defect in formation or stabilization of the thin-filament "on" state that cannot be fully compensated by Tn. This mechanistic heterogeneity among *TPM2* variants is consistent with clinical observations showing that different *TPM2* mutations are associated with a broad spectrum of disease severity (Tajsharghi, Ohlsson, et al., 2007; Ohlsson et al., 2008).

Although the co-sedimentation assays showed that the *TPM2* mutations do not significantly affect formation of the F-actin–Tpm2.2–Tn ternary complex, ELISA experiments performed in the absence of actin revealed more subtle mutation-specific effects on the direct Tpm–Tn interaction. Mutations in P1 (Tpm2.2-D20H and E41K) strengthened Tpm–Tn binding, whereas mutations in P5 (Tpm2.2-E181K and N202K) had little or no detectable influence. These results underscore the pivotal role of the N-terminal P1 region in mediating Tn binding and in transmitting conformational signals from Tn to Tpm and onward to myosin, in line with earlier studies demonstrating that N-terminal segments of Tpm are particularly important for Tn-dependent regulation (Hitchcock-DeGregori et al., 2002; Barua et al., 2012). Importantly, the enhanced Tpm–Tn interaction seen for P1 mutants does not translate into a stronger inhibitory function at low Ca^{2+}. Instead, Tpm2.2-D20H promotes hyperactivation, whereas Tpm2.2-E41K is hypocontractile. This implies that the primary pathogenic effect of these mutations is not simply a change in Tn affinity, but a perturbation in the way Tn-induced structural changes in Tpm are communicated along the filament to modulate actomyosin kinetics. The fact that Tpm2.2-D20H mutant increases Ca^{2+} sensitivity and motor activity without weakening Tn binding suggests that it may shift Tpm equilibrium toward a more "open" position even when Tn is bound, effectively sensitizing the system to Ca^{2+} without compromising regulatory complex assembly.

As discussed above, substitutions in Tpm2.2 reshape the kinetics of the actomyosin cross-bridge cycle by altering product release, Ca^{2+} sensitivity, and myosin motor performance without major changes in the equilibrium binding affinities of Tpm2.2 variants for actin in both the absence and the presence of Tn complex ± Ca^{2+}. However, because Tpm extends along the

length of the filament, mutations can affect filament length, dynamics, and interactions with other actin-binding proteins. Maintaining the mechanical integrity of the thin filament during repeated cycles of contraction is essential for proper muscle contractile function. Disruption of thin-filament integrity by *TPM2* mutations may not only alter contractile function but also promote the formation of abnormal structures, such as nemaline bodies and rods, observed in histopathological analyses of muscle tissue from affected patients. Therefore, I asked a complementary set of questions: whether the same variants that alter cross-bridge kinetics also affect thin-filament assembly, their ability to withstand the mechanical load generated by active myosin cycling, their turnover by Cof2, and length regulation by Tmod1.

6.5 Tpm2.2 as a modulator of actin polymerization and length maintenance

Tpm contributes to actin filament stability by slowing spontaneous G-actin polymerization. This effect is thought to arise from stabilization of short actin oligomers and from a reduction in the number of filament ends available for rapid elongation (Hitchcock-DeGregori et al., 1988; Blanchoin et al., 2001). In the polymerization assay, wild-type Tpm2.2 produced only a modest delay in polymerization, increasing the half-time of the reaction by about 28%. This is considerably weaker than the strong, 70–80% inhibition reported for native skeletal and for recombinant Tpm1.1(Hitchcock-DeGregori et al., 1988; Robaszkiewicz et al., 2016; Janco et al., 2016). Because Tpm1.1 and Tpm2.2 bind F-actin with comparably high affinity (Janco et al., 2016; Robaszkiewicz et al., 2016; Śliwinska et al., 2021) the weaker inhibitory effect of Tpm2.2 cannot simply be explained by differences in binding strength. Instead, it is more likely that isoform-specific geometry of binding, rather than affinity, determines how effectively Tpm slows the addition of new actin monomers to a growing filament.

Among the four mutations tested, only E181K further prolonged the polymerization half-time relative to wild-type Tpm2.2, without changing the cooperativity of the reaction, as indicated by the shape of polymerization curve. Because E181K does not alter the affinity of Tpm2.2 for actin but instead shifts its position on the filament, this result supports the idea that subtle changes in binding geometry, not affinity, govern the inhibitory effect on polymerization. A chain of Tpm positioned slightly differently on nascent actin oligomers may reduce the probability that incoming monomers adopt a conformation that is compatible with productive elongation, thereby slowing filament growth without requiring any change in overall binding strength.

Independently of these differences in polymerization kinetics, none of the mutations, including E181K, altered the final steady-state defined as the equilibrium between a pool of actin monomers and subunits that were incorporated in the filaments, indicating that Tpm is involved in mechanisms setting the rate of filament growth. However, the following polymerization rate of pyrene-labelled actin does not allow to determine the final length of the filaments. To mitigate this weakness of the actin polymerization assay, effects of Tpm variants on the ultimate filament length were assessed by a direct fluorescence microscopy. It clearly demonstrated that averaged length of filaments assembled in the presence of wild-type and mutant Tpm2.2 was similar, which suggests that mechanisms which control early assembly steps and final filament length are functionally separable.

When the regulatory complex was formed with Tn and Ca^{2+}, mutation- and phenotype-specific effects on filament length became apparent. The hypocontractile mutants, especially N202K, produced significantly longer filaments than the wild type, whereas the hypercontractile mutant E181K produced significantly shorter filaments. This divergence shows that Tn adds a layer of regulation that is sensitive to the specific substitution and its associated phenotype, even though Tn binding to actin itself is not affected by these mutations.

6.6 Mechanical load reveals mutation-dependent filament stability

Measurements of filament length under myosin binding in rigor and under active, ATP-driven cross-bridge cycling provide a more physiologically relevant test of thin filament stability than measurements on lipid-covered surface that was used for the assessment of the filament length. Myosin binding in rigor state had little effect on filament length, regardless of whether filaments were bare, wild type-, or mutant-covered, indicating that static myosin attachment does not by itself compromise filament integrity. The situation changed markedly once ATP was added and active cycling began. Under these conditions, nearly all filament populations shortened, but the hypocontractile mutants resisted this shortening and remained significantly longer than wild type. When filaments were formed with the Tpm2.2–Tn complex, most of the variants were shorter than the wild-type Tpm2.2 after ATP addition.

These results align closely with the actomyosin ATPase kinetics established for the same mutations. The hypercontractile variants, which showed the highest actomyosin ATPase rates and fastest product release, also showed the greatest reduction in filament length under load. This points to a direct link between the rate of cross-bridge cycling and the degree of mechanical damage sustained by the filament: faster cycling increases the frequency and

possibly the magnitude of force transients experienced by individual actin subunits, and this repeated mechanical strain appears to compromise filament integrity over time. Conversely, the slower cycling associated with hypocontractile mutations appears to protect the filament from this type of force-induced shortening, consistent with a model in which contractile speed and structural durability of the actin filament are mechanistically coupled (Moraczewska, 2020; Śliwinska et al., 2021).

On the other hand, in the presence of Tn +Ca^{2+} and under mechanical load generated by cycling of active cross-bridges, both hypo- and hypercontractile variants produced shorter filaments than wild type, despite their opposite effects on ATPase activity. This suggests that Ca^{2+}-dependent activation of the thin filament introduces mechanical strain, likely through changes in filament twist and bending stiffness (Borovikov et al., 2025), that acts as a length-equalizing force independent of the specific kinetic defect caused by each mutation.

6.7 Maintenance of the actin filament by capping of the pointed end by Tmod1

Tmod is a protein that stabilizes the filaments by capping their pointed ends. It's binding to actin is highly enhanced by Tpm, which is also required for optimal Tmod1 targeting and function at the pointed end of the thin filament (Fowler et al., 2003; Moroz et al., 2013). Therefore, mutations in TPM genes can result in the filament destabilization by weakening actin interactions with Tmod (Moraczewska et al., 2019).

Filaments capped with Tmod1 and decorated with Tpm2.2 variants remained largely stable, except for N202K, which produced longer filaments than wild type even in the presence of the cap. After ATP was added, all Tpm2.2 variants were stable and showed similar length as compared to bare actin. This shows that pointed end capping with Tmod1 has no particular effect on adjustment of length of filament in the presence of Tpm2.2 and the disease-causing mutations do not change the way Tmod1 interacts with the pointed end of the filament.

A particularly interesting finding is that variants with substitutions in actin-binding period P1 produced shorter initial filaments specifically when both Tn and Tmod1 were present together, whereas P5 variants had no such effect. Because the P1 region is also implicated in Tpm–Tn interactions (as discussed in the preceding sections; ELISA data), this result raises the possibility that the same structural change responsible for enhanced Tn binding also disturbs the cooperative arrangement of Tpm2.2, Tn, and Tmod1 required for stable pointed-end capping. Once actomyosin interactions were initiated, the hypercontractile mutants, but not the hypocontractile ones, showed significantly shorter filaments compared to wild type. This

pattern parallels the increased mechanical vulnerability of hypercontractile filaments observed without Tmod1 and suggests that Tmod1 capping does not fully counteract the destabilizing effect of accelerated cross-bridge cycling associated with these mutations.

Western blot analysis showed that Tmod1 binding to actin itself was not significantly altered by any of the mutations, regardless of the presence of Tn. This result differs from findings obtained for mutations in the slow skeletal muscle isoform, the congenital-myopathy-associated Tpm3.12-R91C mutation, located in actin-binding period P3, reduced Tmod1 binding to the pointed end by approximately 10–15% and weakened the ability of Tmod1 to inhibit pointed-end actin polymerization. In contrast, the Tpm3.12-A4V mutation, positioned within the N-terminal Tmod-binding region, did not significantly affect Tmod1-mediated capping in that study. Both Tpm3.12 mutations also reduced Tpm affinity for F-actin by approximately 2.5-fold, providing a likely explanation for their effects on Tmod1 function (Moraczewska et al., 2019).

Overall, these results indicates that the observed differences in filament length are unlikely to reflect changes in the intrinsic affinity of Tmod1 for the actin filament. Rather, the data are more consistent with an allosteric or positional effect of the mutations on the Tpm2.2–Tn–Tmod1 assembly at the pointed end. In this view, Tmod1 acts not simply as a cap, but as part of a higher-order regulatory complex whose stabilizing effect depends on the structural state of the thin filament.

6.8 Regulation of Cof2 binding to actin by Tpm2.2 variants and Tn

Cosedimentation assays showed that wild-type Tpm2.2 slightly but significantly reduced Cof2's affinity to F-actin, consistent with partial competition between the two proteins for overlapping sites on the actin surface. This behavior does not appear to be unique to Tpm2.2. Previous studies showed that skeletal-muscle Tpm isoforms, including Tpm1.1 and Tpm3.12, also modify Cof2 binding to F-actin. In particular, Cof2 binding to Tpm1.1- or Tpm3.12-decorated filaments increased the apparent affinity of Cof2 for isolated actin-binding sites while markedly decreasing binding cooperativity. At the same time, Cof2 reduced the apparent affinity of both Tpm isoforms for actin, with a stronger inhibitory effect on Tpm1.1 than on Tpm3.12 (Robaszkiewicz et al., 2020). These findings are consistent with a model in which Cof2 binding alters actin filament twist (McGough et al., 1997; Palmer et al., 2026) and thereby generates a filament state that is unfavorable for Tpm association. Previous studies have proposed that ADF/cofilin-mediated dissociation of Tpm is driven not by direct competition for

an identical actin-binding site, but by the ability of the two proteins to stabilize different conformational states of F-actin (Ono & Ono, 2002). Cofilin alters filament twist, subunit tilt, and the actin D-loop at longitudinal intersubunit contacts, whereas skeletal-muscle Tpm binding is sensitive to the conformation of this actin region (Huehn et al., 2020). Thus, Cof2-induced remodeling of the actin filament provides a plausible explanation for the reduced occupancy of Tpm2.2 observed at high Cof2 concentrations, although direct structural evidence for this mechanism in Tpm2.2-decorated thin filaments remains to be obtained.

As Cof2 occupancy increases, Tpm is progressively displaced from the filament, supporting the idea that Cof2 and Tpm compete for structurally incompatible actin conformations (Robaszkiewicz et al., 2016, 2023). Most disease-associated substitutions did not significantly change Tpm inhibitory effect, with the exception of N202K, which showed the weakest inhibition of Cof2 binding among all variants tested. When Cof2 occupancy was increased further, it competitively displaced Tpm2.2 from the filament in a concentration-dependent manner, reducing Tpm2.2 occupancy to as little as 20–50% of its initial level at saturating Cof2 concentrations. D20H stood out among the variants by resisting this displacement more effectively than wild type, remaining bound to the filament at significantly higher levels even at the highest Cof2 concentration tested. This suggests that the D20H substitution either strengthens the local Tpm2.2–actin interaction or hinders the actin conformational change that Cof2 requires to displace Tpm, without producing a detectable change in bulk binding affinity under equilibrium conditions.

The behavior of the fully regulated filament, containing Tpm2.2, Tn, and Ca^{2+}, was markedly different. Cof2 bound with an affinity comparable to filaments without Tn, but the cooperativity of binding increased substantially, and the disease-associated variants produced only minor, though statistically detectable, shifts in Cof2 affinity. Critically, Tn prevented the progressive loss of Tpm2.2 from the filament that was otherwise observed with increasing Cof2 occupancy: Cof2, Tpm2.2, and Tn were able to remain simultaneously bound to actin. A similar effect has been reported for the slow-twitch muscle-specific isoform Tpm3.12, suggesting that this behavior is not unique to Tpm2.2 (Robaszkiewicz et al., 2023). Overall, these finding indicate that incorporation of the Tn complex substantially stabilizes the Tpm2.2–actin interface against cofilin-induced displacement, shifting the system from a competitive to a more cooperative mode of interaction between the regulatory and depolymerizing machinery.

6.9 The role of Tpm2.2 variants in severing and depolymerization of the actin filaments by Cof2

Direct visualization of Cof2-induced severing and depolymerization reinforced and extended the cosedimentation results. Wild-type Tpm2.2 alone did not protect actin filaments from Cof2-mediated severing; filaments behaved essentially like bare actin. This behavior contrasts with previous findings reported for other skeletal muscle Tpm isoforms. In particular, Tpm1.1 and Tpm3.12 increased the frequency of Cof2-induced severing relative to bare F-actin, but the resulting fragments showed slower pointed-end depolymerization and were therefore longer than unregulated filaments (Robaszkiewicz et al., 2020). Earlier work also showed that muscle Tpm1.1, the Tpm1.1–Tpm2.2 heterodimer, and cytoskeletal Tpm3.1 all inhibited Cof2-dependent depolymerization from the pointed end, although the muscle isoforms were more effective than Tpm3.1 (Robaszkiewicz et al., 2016).

The hypocontractile mutants provided increasing protection against severing over time while the hypercontractile mutants behaved like wild type. A comparable mutation-dependent stabilization of thin filaments has been reported for the slow skeletal-muscle isoform Tpm3.12. In that study, the hypocontractile myopathy-associated Tpm3.12-R91C variant inhibited Cof2-induced severing and depolymerization more effectively than wild-type Tpm3.12, resulting in longer and more persistent filament fragments (Robaszkiewicz et al., 2023). Although the affected residues differ—R91C in actin-binding period P3 of Tpm3.12 versus E41K and N202K in P1 and P5 of Tpm2.2—the functional outcome is similar: reduced thin-filament turnover and relative preservation of filament length. This may reflect mutation-dependent changes in Tpm positioning, local flexibility, or the conformational state of the underlying actin filament, which together reduce the ability of Cof2 to introduce destabilizing structural changes.

Consistent with Tn-mediated stabilization of Tpm2.2 on the filament, addition of Tn and Ca^{2+} enhanced protection against severing. However, the mutations again produced divergent effects: E181K showed markedly weaker protection, with filaments easily severed by Cof2, whereas N202K again maintained longer filaments than wild type. It is important to note that both substitutions are located in P5 of Tpm2.2. A pattern similar to N202K was observed for Tpm3.12-R91C. In the presence of Tn, Cof2-dependent severing and depolymerization of filaments decorated with either wild-type or mutant Tpm3.12 was reduced, but the R91C variant remained more protective than wild type (Robaszkiewicz et al., 2023).

Connection between filament length regulation and contractile phenotype gains additional significance in light of the known relationship between fiber type and thin filament

length: slow-twitch fibers contain longer thin filaments than fast-twitch fibers (Gokhin et al., 2012). The longer filaments produced by the hypocontractile N202K variant, and the shorter filaments produced by the hypercontractile E181K variant, are therefore consistent with the contractile phenotypes associated with each mutation. However, this interpretation should be regarded as a working hypothesis rather than a direct demonstration of a causal relationship. The differences in filament length were observed in simplified *in vitro* microscopy assays, which cannot fully reproduce the structural organization, protein composition, mechanical loading, or continuous turnover of thin filaments in muscle cells. To test this hypothesis, future studies should examine the effects of Tpm2.2-N202K and Tpm2.2-E181K in cellular and muscle-based systems.

6.10 Effects of Tmod1on the filament shortening by Cof2

In the presence of Tmod1, which caps the pointed ends of the filaments, Tpm2.2 exerted a protective effect against Cof2-mediated depolymerization. Since Cof2 depolymerizes actin predominantly from the pointed end (Kremneva et al., 2014; Wioland et al., 2017), this effect could be explained simply by Tmod1-mediated stabilization of the pointed end, making it less accessible to Cof2 and thereby reducing filament disassembly. Alternatively, Tmod1 could alter the affinity of Cof2 for F-actin–Tpm2.2. However, this possibility was excluded by co-sedimentation assays showing that Cof2 bound F-actin–Tpm2.2 with similar affinity in the presence of Tmod1. Thus, Tpm2.2 protects the filaments, but only in the presence of other actin-binding proteins, such as Tn and Tmod. To my knowledge, no other Tpm isoforms were tested for their abilities collaborate with Tmod1 in protecting the filaments against Cof2-dependent depolymerization. It is worth noting that under certain conditions Cof2-mediated disassembly can occur from both filament ends (Wioland et al., 2017). Therefore, the protective effect of Tmod1 may reflect not only pointed-end capping but also stabilization of the local Tpm2.2–actin architecture, thereby rendering the filaments more resistant to severing and depolymerization.

The pattern of thin-filament protection against Cof2-mediated depolymerization changed when Tpm2.2 mutants replaced the wild type. Whereas Tpm2.2-D20H retained the protective effect observed for wild-type Tpm2.2, the remaining mutants almost completely lost their ability to protect the filament from depolymerization. This diversity became even more pronounced when Tn was included. As in the absence of Tmod1, Tmod1-capped filaments

coated with the Tpm2.2–Tn complex were protected from Cof2-mediated depolymerization; however, substitutions in P1 and P5 reduced the protective capacity of this regulatory complex.

At this stage, the molecular basis of the effects discussed above is likely to involve multiple, interrelated mechanisms. As a "gatekeeper" of the actin filament, Tpm regulates interactions with a wide range of actin-binding proteins in a context-dependent manner. Consequently, substitutions in functionally important regions of Tpm2.2, such as P1 and P5, may have distinct effects on these interactions. Increasing complexity of the thin-filament protein composition may further contribute to the diversity of the observed phenotypes. Thus, no single, simple mechanism can account for the effects of the hypo- and hypercontractile mutations. Nevertheless, the findings demonstrate that disease-causing mutations disrupt the mechanisms responsible for maintaining thin-filament length required for proper contraction. Dysregulation of filament length is therefore likely to contribute to and modulate the final disease phenotype.

6.11 Strengths and weaknesses of the experimental design

In this study, the thin filament system was reconstituted using a heterologous combination of proteins, because of practical and experimental constraints associated with obtaining fully human-derived components. While an entirely homologous human system would be preferable, it remains technically challenging due to limited availability and difficulties in purification of certain proteins. Therefore, actin, myosin S1, HMM, and Tn complex were isolated from rabbit skeletal muscle, which is a well-established and functionally conserved model system. Human Tpm2.2 (wild-type and mutant variants) was recombinantly expressed in *E. coli* to directly assess the effects of human sequence variations (Śliwinska et al., 2021). In addition, Cof2 and Tmod1 were encoded by mouse genes and recombinantly expressed in *E. coli* (Robaszkiewicz et al., 2016; Schultz et al., 2023). Although this heterologous system introduces potential interspecies differences, the high degree of structural and functional conservation among these proteins supports its validity as a model for investigating thin filament regulation. Notably, alignment of human (P68133) and rabbit (P68135) skeletal muscle α-actin protein sequences showed that the sequences are 100% identical supporting the use of rabbit actin as a close model for the human skeletal-muscle filament. Rabbit skeletal-muscle proteins have also been used extensively in biochemical reconstitution experiments and provide a robust, reproducible system for investigating conserved mechanisms of thin-filament regulation.

The wild-type and mutant Tpm2.2 were obtained in pure form and could be compared under identical biochemical conditions. This would be very difficult using patient-derived skeletal muscle, where mutant and wild-type Tpm2.2 coexist with other Tpm isoforms and where the relative contribution of each Tpm population cannot be easily controlled (Lehrer et al., 2011; Janco et al., 2013; Gregorich et al., 2014; Jin et al., 2016). In addition, patient samples are not widely available and would contain variable proportions of fast and slow fibers, distinct Tpm heterodimers, differing levels of mutant protein expression, and secondary pathological changes (Geeves et al., 2015; Lambert & Gussoni, 2023). The reconstituted system therefore allowed the observed effects to be assigned directly to individual Tpm2.2 substitutions rather than to secondary cellular or tissue-level adaptations.

One of the limitations of this thesis, which need to be acknowledged, is that all functional assays were performed with homodimeric Tpm2.2, whereas *in vivo* Tpm2.2 predominantly forms heterodimers with Tpm1.1 in fast fibers and with Tpm3.12 in slow fibers (Cummins & Perry, 1973; Perry, 2001; Moraczewska, 2020). The functional properties of Tpm1.1–Tpm2.2 heterodimers differ from those of the respective homodimers, and mutations in a single Tpm2.2 chain can exert additive or dominant effects on heterodimer function (Janco et al., 2012; Bershitsky et al., 2019; Śliwinska et al., 2021). However, to obtain stable heterodimers for use in biochemical *in vitro* assays, the chains of Tpm paralogs must be cross-linked (Kalyva et al., 2012). Such cross-linking can constrain the flexibility of the Tpm coiled coil and potentially mask the effects of individual amino acid substitutions (Śliwinska et al., 2021). Therefore, the use of homodimers rather than heterodimers is justified for investigating the effects of disease-associated mutations. Notably, expression of the pathogenic *TPM2* E41K mutation leads to elevated Tpm2.2 levels and an increased proportion of Tpm2.2 homodimers in patient fibers, suggesting that homodimer-based assays may be particularly relevant for this Tpm isoform (Ochala et al., 2008). Thus, while heterodimeric systems are required for a complete understanding of *TPM2*-related disease, homodimeric Tpm2.2 provides an essential starting point for defining mutation-specific molecular mechanisms.

At the same time, recombinant expression in *E. coli* introduces limitations related to post-translational modifications. Native skeletal-muscle Tpm is normally N-terminally acetylated, whereas proteins expressed in *E. coli* generally lack this modification. N-terminal acetylation is important for head-to-tail Tpm polymerization, high-affinity actin binding, and normal regulatory function. To address this issue, recombinant muscle Tpm constructs are commonly produced with an N-terminal Ala–Ser extension, which functionally mimics native

N-terminal acetylation and restores actin affinity and regulatory behavior in many *in-vitro* assays (Monteiro et al., 1994). The Ala–Ser strategy is therefore a well-established solution that enables functional analysis of recombinant Tpm2.2. However, it should not be considered fully equivalent to native acetylation in every structural or regulatory context. In particular, recombinant proteins lack other potentially relevant modifications present in muscle, including phosphorylation, oxidation, or other modification states that may vary with fiber type, developmental stage, mechanical loading, and disease.

Overall, the reconstituted system used in this thesis offers a substantial strength: it combines highly purified proteins, defined stoichiometries, controlled Ca^{2+} conditions, and direct analysis of human disease-associated Tpm2.2 variants within a multi-protein thin-filament environment. Its limitations include the heterologous origin of several proteins, the absence of native post-translational modifications and sarcomeric architecture, and the use of homodimeric rather than heterodimeric Tpm2.2. Therefore, the findings should be interpreted as mechanistic evidence for direct effects of *TPM2* mutations on thin-filament regulation and stability, rather than as a complete reproduction of the cellular disease state. Future studies using recombinant human heterodimers, mammalian expression systems that preserve native Tpm modifications, patient-derived myotubes, engineered skeletal-muscle tissues, and muscle-fiber preparations will be needed to test how these mechanisms operate in the physiological environment of the sarcomere.

7 Conclusions

The four variants examined separated broadly into hypercontractile and hypocontractile classes that reflected their known clinical and functional phenotypes, yet the underlying biochemical defects were clearly not uniform. Instead, the data show that the consequences of mutations depend on a combination of factors: the actin-binding period in which the substitution occurs, its location within the 1st- or 2nd-half of that period, and the particular protein environment in which the mutant Tpm is operating.

Specifically, the results presented in this dissertation support the following general conclusions:

1) Actin-binding periods P1 and P5 are crucially involved in a wide-range of regulatory functions of Tpm2.2, such as regulation of cross-bridge cycle, control of filament integrity and length.

2) Disease-associated substitutions in Tpm2.2 perturb thin-filament regulation through mechanisms that extend well beyond simple changes in Tpm2.2 affinity for actin.

3) Pathogenic variation in Tpm2.2 alter the geometric and allosteric properties of the Tpm chain affecting interactions with Tn complex and regulation of the actomyosin crossbridge cycle.

4) Substitutions in periods P1 and P5 of Tpm2.2 alter the communication network linking actin, Tpm, Tn, myosin, Tmod1, and Cof2, thereby affecting the filament to preserve its length and structural integrity over time.

5) Regulation of contraction and maintenance of the filament integrity are mechanistically intertwined.

6) While defects in the regulation of actin–myosin interactions correlate with the hyper- and hypocontractile phenotypes observed in patients, the mutation-induced alterations in filament length and stability may contribute to the development of filament disarray and the formation of abnormal structures, such as actin caps and nemaline bodies, observed in patients' muscle cells.

Thus, the thesis extends the understanding of Tpm functions beyond the classical framework of Ca^{2+} sensitivity and cross-bridge kinetics. The thin filament is not merely activated or inhibited; it is assembled, maintained, mechanically stressed, and continuously remodeled. Mutations subtly alter the structure of Tpm that is used to communicate with its

binding partners. The substitutions can therefore produce consequences that accumulate over multiple spatial and temporal scales, from molecular kinetics to filament architecture and, ultimately, to muscle phenotype.

8 Publications

Most results presented in this dissertation were published in the following papers:

- Küçükdogru, Recep, et al. "Mechanochemical consequences of myopathy-linked mutations in Tpm2. 2 on striated muscle contractility." The FASEB Journal 38.1 (2024): e23400.
- Küçükdogru, Recep, et al. "Myopathy-linked mutations in TPM2 and their impact on troponin-mediated regulation of actomyosin contractility." The FEBS Journal 292.21 (2025): 5789-5801.
- Küçükdogru, Recep, et al. "Disease-associated mutations in TPM2 alter regulation of actin filament stability and cofilin-dependent dynamics." bioRxiv (2026): 2026-05. Note: This manuscript is currently undergoing its second round of peer review and is being considered for publication in The FEBS Journal.

The results were presented at the following international conferences:

- Poster: “Impact of *TPM2* Myopathy-Linked Mutations on Thin Filament Length Regulation“ – 52nd European Muscle Conference, September 20-24, 2025.
- Poster: “Impact of myopathy-linked *TPM2* mutations on troponin-mediated actomyosin regulations” – 49th FEBS Congress, July 5-9, 2025.
- Poster: “Effects of troponin and myopathy-related tropomyosin mutants on cofilin-2 binding and depolymerization of the thin filament” – 49th European Muscle Conference, September 23-26, 2022.
- Poster: “Mutations E41K and N202K in tropomyosin Tpm2.2 impair Ca^{2+}-dependent activation of acto-myosin interactions” – Virtual European Muscle Conference, Warsaw, September 20–22, 2021.

9 References

Aborode, A. T., Olamilekan Adesola, R., Idris, I., Adio, W. S., Scott, G. Y., Chakoma, M., Oluwaseun, A. A., Onifade, I. A., Adeoye, A. F., Aluko, B. A., & Abok, J. I. (2024). Troponin C gene mutations on cardiac muscle cell and skeletal Regulation: A comprehensive review. *Gene*, *927*, 148651. https://doi.org/10.1016/j.gene.2024.148651

Agrawal, P. B., Joshi, M., Savic, T., Chen, Z., & Beggs, A. H. (2012). Normal myofibrillar development followed by progressive sarcomeric disruption with actin accumulations in a mouse Cfl2 knockout demonstrates requirement of cofilin-2 for muscle maintenance. *Human Molecular Genetics*, *21*(10), 2341–2356. https://doi.org/10.1093/hmg/dds053

Andrianantoandro, E., & Pollard, T. D. (2006). Mechanism of actin filament turnover by severing and nucleation at different concentrations of ADF/cofilin. *Molecular Cell*, *24*(1), 13–23. https://doi.org/10.1016/j.molcel.2006.08.006

Atkinson, S. J., & Stewart, M. (1992). Molecular interactions in myosin assembly: Role of the 28-residue charge repeat in the rod. *Journal of Molecular Biology*, *226*(1), 7–13. https://doi.org/10.1016/0022-2836(92)90118-4

Bailey, K. (1946). Tropomyosin: A new asymmetric protein component of muscle. *Nature*, *157*, 368. https://doi.org/10.1038/157368b0

Bamburg, J. R. (1999). Proteins of the ADF/cofilin family: Essential regulators of actin dynamics. *Annual Review of Cell and Developmental Biology*, *15*, 185–230. https://doi.org/10.1146/annurev.cellbio.15.1.185

Barua, B. (2013). Periodicities designed in the tropomyosin sequence and structure define its functions. *Bioarchitecture*, *3*(3), 51–56. https://doi.org/10.4161/bioa.25616

Barua, B., Pamula, M. C., & Hitchcock-DeGregori, S. E. (2011). Evolutionarily conserved surface residues constitute actin binding sites of tropomyosin. *Proceedings of the National Academy of Sciences of the United States of America*, *108*(25), 10150–10155. https://doi.org/10.1073/pnas.1101221108

Barua, B., Winkelmann, D. A., White, H. D., & Hitchcock-DeGregori, S. E. (2012). Regulation of actin-myosin interaction by conserved periodic sites of tropomyosin. *Proceedings of the National Academy of Sciences of the United States of America*, *109*(45), 18425–18430. https://doi.org/10.1073/pnas.1212754109

Beck, A. E., McMillin, M. J., Gildersleeve, H. I. S., Kezele, P. R., Shively, K. M., Carey, J. C., Regnier, M., & Bamshad, M. J. (2013). Spectrum of mutations that cause distal arthrogryposis types 1 and 2B. *American Journal of Medical Genetics. Part A*, *161A*(3), 550–555. https://doi.org/10.1002/ajmg.a.35809

Behrmann, E., Müller, M., Penczek, P. A., Mannherz, H. G., Manstein, D. J., & Raunser, S. (2012). Structure of the rigor actin-tropomyosin-myosin complex. *Cell*, *150*(2), 327–338. https://doi.org/10.1016/j.cell.2012.05.037

Bers, D. M. (2002). Cardiac excitation–contraction coupling. *Nature*, *415*(6868), 198–205. https://doi.org/10.1038/415198a

Bershitsky, S. Y., Logvinova, D. S., Shchepkin, D. V., Kopylova, G. V., & Matyushenko, A. M. (2019). Myopathic mutations in the β-chain of tropomyosin differently affect the

structural and functional properties of ββ- and αβ-dimers. *The FASEB Journal*, *33*(2), 1963–1971. https://doi.org/10.1096/fj.201800755R

Bibeau, J. P., Gray, S., & De La Cruz, E. M. (2021). Clusters of a Few Bound Cofilins Sever Actin Filaments. *Journal of Molecular Biology*, *433*(7), 166833. https://doi.org/10.1016/j.jmb.2021.166833

Blanchoin, L., Pollard, T. D., & Hitchcock-DeGregori, S. E. (2001). Inhibition of the Arp2/3 complex-nucleated actin polymerization and branch formation by tropomyosin. *Current Biology: CB*, *11*(16), 1300–1304. https://doi.org/10.1016/s0960-9822(01)00395-5

Borovikov, Y. S., Tishkova, M. V., Avrova, S. V., Sirenko, V. V., & Karpicheva, O. E. (2025). The Twisting and Untwisting of Actin and Tropomyosin Filaments Are Involved in the Molecular Mechanisms of Muscle Contraction, and Their Disruption Can Result in Muscle Disorders. *International Journal of Molecular Sciences*, *26*(14), 6705. https://doi.org/10.3390/ijms26146705

Brown, J. H., Kim, K. H., Jun, G., Greenfield, N. J., Dominguez, R., Volkmann, N., Hitchcock-DeGregori, S. E., & Cohen, C. (2001). Deciphering the design of the tropomyosin molecule. *Proceedings of the National Academy of Sciences of the United States of America*, *98*(15), 8496–8501. https://doi.org/10.1073/pnas.131219198

Brown, J. H., Zhou, Z., Reshetnikova, L., Robinson, H., Yammani, R. D., Tobacman, L. S., & Cohen, C. (2005). Structure of the mid-region of tropomyosin: Bending and binding sites for actin. *Proceedings of the National Academy of Sciences of the United States of America*, *102*(52), 18878–18883. https://doi.org/10.1073/pnas.0509269102

Cachia, P. J., Van Eyk, J., McCubbin, W. D., Kay, C. M., & Hodges, R. S. (1985). Ion-exchange high-performance liquid chromatographic purification of bovine cardiac and rabbit skeletal muscle troponin subunits. *Journal of Chromatography*, *343*(2), 315–328. https://doi.org/10.1016/s0378-4347(00)84600-9

Carman, P. J., Barrie, K. R., Rebowski, G., & Dominguez, R. (2023). Structures of the free and capped ends of the actin filament. *Science*, *380*(6651), 1287–1292. https://doi.org/10.1126/science.adg6812

Cassandrini, D., Trovato, R., Rubegni, A., Lenzi, S., Fiorillo, C., Baldacci, J., Minetti, C., Astrea, G., Bruno, C., Santorelli, F. M., & Italian Network on Congenital Myopathies. (2017). Congenital myopathies: Clinical phenotypes and new diagnostic tools. *Italian Journal of Pediatrics*, *43*(1), 101. https://doi.org/10.1186/s13052-017-0419-z

Castillo, A., Nowak, R., Littlefield, K. P., Fowler, V. M., & Littlefield, R. S. (2009). A nebulin ruler does not dictate thin filament lengths. *Biophysical Journal*, *96*(5), 1856–1865. https://doi.org/10.1016/j.bpj.2008.10.053

Clarke, N. F. (2008). Skeletal muscle disease due to mutations in tropomyosin, troponin and cofilin. *Advances in Experimental Medicine and Biology*, *642*, 40–54. https://doi.org/10.1007/978-0-387-84847-1_4

Colpan, M., Moroz, N. A., Gray, K. T., Cooper, D. A., Diaz, C. A., & Kostyukova, A. S. (2016). Tropomyosin-Binding Properties Modulate Competition Between Tropomodulin Isoforms. *Archives of Biochemistry and Biophysics*, *600*, 23–32. https://doi.org/10.1016/j.abb.2016.04.006

Colpan, M., Moroz, N. A., & Kostyukova, A. S. (2013). Tropomodulins and tropomyosins: Working as a team. *Journal of Muscle Research and Cell Motility*, *34*(3–4), 247–260. https://doi.org/10.1007/s10974-013-9349-6

Coluccio, L. M. (1994). An end in sight: Tropomodulin. *The Journal of Cell Biology*, *127*(6 Pt 1), 1497–1499. https://doi.org/10.1083/jcb.127.6.1497

Corbett, M. A., Akkari, P. A., Domazetovska, A., Cooper, S. T., North, K. N., Laing, N. G., Gunning, P. W., & Hardeman, E. C. (2005). An alphaTropomyosin mutation alters dimer preference in nemaline myopathy. *Annals of Neurology*, *57*(1), 42–49. https://doi.org/10.1002/ana.20305

Craig, R., Dutta, D., Koubassova, N. A., Tsaturyan, A. K., & Padrón, R. (2026). Comparing cryo-EM structures of the vertebrate cardiac muscle thick filament. *Biophysical Reviews*. https://doi.org/10.1007/s12551-025-01393-9

Craig, R., & Woodhead, J. L. (2006). Structure and function of myosin filaments. *Current Opinion in Structural Biology*, *16*(2), 204–212. https://doi.org/10.1016/j.sbi.2006.03.006

Criddle, A. H., Geeves, M. A., & Jeffries, T. (1985). The use of actin labelled with N-(1-pyrenyl)iodoacetamide to study the interaction of actin with myosin subfragments and troponin/tropomyosin. *Biochemical Journal*, *232*(2), 343–349. https://doi.org/10.1042/bj2320343

Cummins, P., & Perry, S. V. (1973). The subunits and biological activity of polymorphic forms of tropomyosin. *Biochemical Journal*, *133*(4), 765–777. https://doi.org/10.1042/bj1330765

Dominguez, R. (2011). Tropomyosin: The gatekeeper's view of the actin filament revealed. *Biophysical Journal*, *100*(4), 797–798. https://doi.org/10.1016/j.bpj.2011.01.018

Dominguez, R. (2019). Nucleotide-dependent conformational changes in the actin filament: Subtler than expected. *Proceedings of the National Academy of Sciences of the United States of America*, *116*(10), 3959–3961. https://doi.org/10.1073/pnas.1900799116

Dominguez, R., & Holmes, K. C. (2011). Actin structure and function. *Annual Review of Biophysics*, *40*, 169–186. https://doi.org/10.1146/annurev-biophys-042910-155359

Doran, M. H., Pavadai, E., Rynkiewicz, M. J., Walklate, J., Bullitt, E., Moore, J. R., Regnier, M., Geeves, M. A., & Lehman, W. (2020). Cryo-EM and Molecular Docking Shows Myosin Loop 4 Contacts Actin and Tropomyosin on Thin Filaments. *Biophysical Journal*, *119*(4), 821–830. https://doi.org/10.1016/j.bpj.2020.07.006

Doran, M. H., Rynkiewicz, M. J., Pavadai, E., Bodt, S. M. L., Rasicci, D., Moore, J. R., Yengo, C. M., Bullitt, E., & Lehman, W. (2023). Myosin loop-4 is critical for optimal tropomyosin repositioning on actin during muscle activation and relaxation. *The Journal of General Physiology*, *155*(2), e202213274. https://doi.org/10.1085/jgp.202213274

Dowling, J. J., Weihl, C. C., & Spencer, M. J. (2021). Molecular and cellular basis of genetically inherited skeletal muscle disorders. *Nature Reviews. Molecular Cell Biology*, *22*(11), 713–732. https://doi.org/10.1038/s41580-021-00389-z

Ebashi, S., & Endo, M. (1968). Calcium ion and muscle contraction. *Progress in Biophysics and Molecular Biology*, *18*, 123–183. https://doi.org/10.1016/0079-6107(68)90023-0

Ebashi, S., & Kodama, A. (1965). A new protein factor promoting aggregation of tropomyosin. *Journal of Biochemistry*, *58*(1), 107–108. https://doi.org/10.1093/oxfordjournals.jbchem.a128157

Fass, J., Gehler, S., Sarmiere, P., Letourneau, P., & Bamburg, J. R. (2004). Regulating filopodial dynamics through actin-depolymerizing factor/cofilin. *Anatomical Science International*, *79*(4), 173–183. https://doi.org/10.1111/j.1447-073x.2004.00087.x

Feuer, G., & Molnar, F. (1948). Studies on the composition and polymerization of actin. *Hungarica Acta Physiologica*, *1*(4–5), 150–163.

Fowler, V. M., & Dominguez, R. (2017). Tropomodulins and Leiomodins: Actin Pointed End Caps and Nucleators in Muscles. *Biophysical Journal*, *112*(9), 1742–1760. https://doi.org/10.1016/j.bpj.2017.03.034

Fowler, V. M., Greenfield, N. J., & Moyer, J. (2003). Tropomodulin contains two actin filament pointed end-capping domains. *The Journal of Biological Chemistry*, *278*(41), 40000–40009. https://doi.org/10.1074/jbc.M306895200

Franz, P., Ewert, W., Preller, M., & Tsiavaliaris, G. (2021). Unraveling a Force-Generating Allosteric Pathway of Actomyosin Communication Associated with ADP and Pi Release. *International Journal of Molecular Sciences*, *22*(1), 104. https://doi.org/10.3390/ijms22010104

Fujii, T., Iwane, A. H., Yanagida, T., & Namba, K. (2010). Direct visualization of secondary structures of F-actin by electron cryomicroscopy. *Nature*, *467*(7316), 724–728. https://doi.org/10.1038/nature09372

Fujii, T., & Namba, K. (2017). Structure of actomyosin rigour complex at 5.2 Å resolution and insights into the ATPase cycle mechanism. *Nature Communications*, *8*(1), 13969. https://doi.org/10.1038/ncomms13969

Galler, S., Wang, B. G., & Kawai, M. (2005). Elementary steps of the cross-bridge cycle in fast-twitch fiber types from rabbit skeletal muscles. *Biophysical Journal*, *89*(5), 3248–3260. https://doi.org/10.1529/biophysj.104.056614

Geeves, M. A., Hitchcock-DeGregori, S. E., & Gunning, P. W. (2015). A systematic nomenclature for mammalian tropomyosin isoforms. *Journal of Muscle Research and Cell Motility*, *36*(2), 147–153. https://doi.org/10.1007/s10974-014-9389-6

Geeves, M. A., & Holmes, K. C. (1999). Structural mechanism of muscle contraction. *Annual Review of Biochemistry*, *68*, 687–728. https://doi.org/10.1146/annurev.biochem.68.1.687

Geeves, M. A., & Holmes, K. C. (2005). The molecular mechanism of muscle contraction. *Advances in Protein Chemistry*, *71*, 161–193. https://doi.org/10.1016/S0065-3233(04)71005-0

Gokhin, D. S., & Fowler, V. M. (2011). Tropomodulin Capping of Actin Filaments in Striated Muscle Development and Physiology. *Journal of Biomedicine and Biotechnology*, *2011*, 103069. https://doi.org/10.1155/2011/103069

Gokhin, D. S., Kim, N. E., Lewis, S. A., Hoenecke, H. R., D'Lima, D. D., & Fowler, V. M. (2012). Thin-filament length correlates with fiber type in human skeletal muscle. *American Journal of Physiology. Cell Physiology*, *302*(3), C555-565. https://doi.org/10.1152/ajpcell.00299.2011

Gokhin, D. S., Lewis, R. A., McKeown, C. R., Nowak, R. B., Kim, N. E., Littlefield, R. S., Lieber, R. L., & Fowler, V. M. (2010). Tropomodulin isoforms regulate thin filament pointed-end capping and skeletal muscle physiology. *The Journal of Cell Biology*, *189*(1), 95–109. https://doi.org/10.1083/jcb.201001125

Gordon, A. M., Homsher, E., & Regnier, M. (2000). Regulation of contraction in striated muscle. *Physiological Reviews*, *80*(2), 853–924. https://doi.org/10.1152/physrev.2000.80.2.853

Gotti, C., Sensini, A., Zucchelli, A., Carloni, R., & Focarete, M. L. (2020). Hierarchical fibrous structures for muscle-inspired soft-actuators: A review. *Applied Materials Today*, *20*, 100772. https://doi.org/10.1016/j.apmt.2020.100772

Granzier, H. L., Akster, H. A., & Ter Keurs, H. E. (1991). Effect of thin filament length on the force-sarcomere length relation of skeletal muscle. *The American Journal of Physiology*, *260*(5 Pt 1), C1060-1070. https://doi.org/10.1152/ajpcell.1991.260.5.C1060

Greenfield, N. J., Huang, Y. J., Swapna, G. V. T., Bhattacharya, A., Rapp, B., Singh, A., Montelione, G. T., & Hitchcock-DeGregori, S. E. (2006). Solution NMR structure of the junction between tropomyosin molecules: Implications for actin binding and regulation. *Journal of Molecular Biology*, *364*(1), 80–96. https://doi.org/10.1016/j.jmb.2006.08.033

Greenfield, N. J., Kotlyanskaya, L., & Hitchcock-DeGregori, S. E. (2009). Structure of the N Terminus of a Non-Muscle α-Tropomyosin in Complex with the C Terminus: Implications for Actin Binding. *Biochemistry*, *48*(6), 1272–1283. https://doi.org/10.1021/bi801861k

Gregorich, Z. R., Chang, Y.-H., & Ge, Y. (2014). Proteomics in Heart Failure: Top-down or Bottom-up? *Pflugers Archiv : European Journal of Physiology*, *466*(6), 1199–1209. https://doi.org/10.1007/s00424-014-1471-9

Gunning, P. (2008). Emerging issues for tropomyosin structure, regulation, function and pathology. *Advances in Experimental Medicine and Biology*, *644*, 293–298. https://doi.org/10.1007/978-0-387-85766-4_22

Gunning, P., O'Neill, G., & Hardeman, E. (2008). Tropomyosin-based regulation of the actin cytoskeleton in time and space. *Physiological Reviews*, *88*(1), 1–35. https://doi.org/10.1152/physrev.00001.2007

Gunning, P. W., Hardeman, E. C., Lappalainen, P., & Mulvihill, D. P. (2015). Tropomyosin – master regulator of actin filament function in the cytoskeleton. *Journal of Cell Science*, *128*(16), 2965–2974. https://doi.org/10.1242/jcs.172502

Gupte, T. M., Haque, F., Gangadharan, B., Sunitha, M. S., Mukherjee, S., Anandhan, S., Rani, D. S., Mukundan, N., Jambekar, A., Thangaraj, K., Sowdhamini, R., Sommese, R. F., Nag, S., Spudich, J. A., & Mercer, J. A. (2015). Mechanistic heterogeneity in contractile properties of α-tropomyosin (TPM1) mutants associated with inherited cardiomyopathies. *The Journal of Biological Chemistry*, *290*(11), 7003–7015. https://doi.org/10.1074/jbc.M114.596676

Hayden, S. M., Miller, P. S., Brauweiler, A., & Bamburg, J. R. (1993). Analysis of the interactions of actin depolymerizing factor with G- and F-actin. *Biochemistry*, *32*(38), 9994–10004. https://doi.org/10.1021/bi00089a015

Heeley, D. H., Belknap, B., & White, H. D. (2002). Mechanism of regulation of phosphate dissociation from actomyosin-ADP-Pi by thin filament proteins. *Proceedings of the National Academy of Sciences of the United States of America*, *99*(26), 16731–16736. https://doi.org/10.1073/pnas.252236399

Heeley, D. H., Belknap, B., & White, H. D. (2006). Maximal activation of skeletal muscle thin filaments requires both rigor myosin S1 and calcium. *The Journal of Biological Chemistry*, *281*(1), 668–676. https://doi.org/10.1074/jbc.M505549200

Hitchcock-DeGregori, S. E., & Barua, B. (2017). Tropomyosin Structure, Function, and Interactions: A Dynamic Regulator. *Sub-Cellular Biochemistry*, *82*, 253–284. https://doi.org/10.1007/978-3-319-49674-0_9

Hitchcock-DeGregori, S. E., Sampath, P., & Pollard, T. D. (1988). Tropomyosin inhibits the rate of actin polymerization by stabilizing actin filaments. *Biochemistry*, *27*(26), 9182–9185. https://doi.org/10.1021/bi00426a016

Hitchcock-DeGregori, S. E., Song, Y., & Greenfield, N. J. (2002). Functions of Tropomyosin's Periodic Repeats†. *Biochemistry*, *41*(50), 15036–15044. https://doi.org/10.1021/bi026519k

Holmes, K. C., Popp, D., Gebhard, W., & Kabsch, W. (1990). Atomic model of the actin filament. *Nature*, *347*(6288), 44–49. https://doi.org/10.1038/347044a0

Houdusse, A., & Sweeney, H. L. (2016). How myosin generates force on actin filaments. *Trends in Biochemical Sciences*, *41*(12), 989–997. https://doi.org/10.1016/j.tibs.2016.09.006

Huehn, A. R., Bibeau, J. P., Schramm, A. C., Cao, W., De La Cruz, E. M., & Sindelar, C. V. (2020). Structures of cofilin-induced structural changes reveal local and asymmetric perturbations of actin filaments. *Proceedings of the National Academy of Sciences of the United States of America*, *117*(3), 1478–1484. https://doi.org/10.1073/pnas.1915987117

Huxley, A. F. (1957). 6—Muscle Structure and Theories of Contraction. *Progress in Biophysics and Biophysical Chemistry*, *7*, 255–318. https://doi.org/10.1016/S0096-4174(18)30128-8

Huxley, H. E. (1969). The mechanism of muscular contraction. *Science*, *164*(3886), 1356–1365. https://doi.org/10.1126/science.164.3886.1356

Huxley, H. E., & Kress, M. (1985). Crossbridge behaviour during muscle contraction. *Journal of Muscle Research and Cell Motility*, *6*(2), 153–161. https://doi.org/10.1007/BF00713057

Ishii, S., Oyama, K., Kobirumaki-Shimozawa, F., Nakanishi, T., Nakahara, N., Suzuki, M., Ishiwata, S., & Fukuda, N. (2023). Myosin and tropomyosin-troponin complementarily regulate thermal activation of muscles. *The Journal of General Physiology*, *155*(12), e202313414. https://doi.org/10.1085/jgp.202313414

Ishii, Y., & Lehrer, S. S. (1990). Excimer fluorescence of pyrenyliodoacetamide-labeled tropomyosin: A probe of the state of tropomyosin in reconstituted muscle thin filaments. *Biochemistry*, *29*(5), 1160–1166. https://doi.org/10.1021/bi00457a010

Ishiwata, S. (1978). Studies on the F-actin.tropomyosin.troponin complex. III. Effects of troponin components and calcium ion on the binding affinity between tropomyosin and F-actin. *Biochimica Et Biophysica Acta*, *534*(2), 350–357. https://doi.org/10.1016/0005-2795(78)90018-1

Janco, M., Bonello, T. T., Byun, A., Coster, A. C. F., Lebhar, H., Dedova, I., Gunning, P. W., & Böcking, T. (2016). The impact of tropomyosins on actin filament assembly is isoform specific. *Bioarchitecture*, *6*(4), 61–75. https://doi.org/10.1080/19490992.2016.1201619

Janco, M., Kalyva, A., Scellini, B., Piroddi, N., Tesi, C., Poggesi, C., & Geeves, M. A. (2012). α-Tropomyosin with a D175N or E180G Mutation in Only One Chain Differs from Tropomyosin with Mutations in Both Chains. *Biochemistry*, *51*(49), 9880–9890. https://doi.org/10.1021/bi301323n

Janco, M., Suphamungmee, W., Li, X., Lehman, W., Lehrer, S. S., & Geeves, M. A. (2013). Polymorphism in tropomyosin structure and function. *Journal of Muscle Research and Cell Motility*, *34*(0), 177–187. https://doi.org/10.1007/s10974-013-9353-x

Jin, Y., Peng, Y., Lin, Z., Chen, Y.-C., Wei, L., Hacker, T. A., Larsson, L., & Ge, Y. (2016). Comprehensive Analysis of Tropomyosin Isoforms in Skeletal Muscles by Top-down Proteomics. *Journal of Muscle Research and Cell Motility*, *37*(1–2), 41–52. https://doi.org/10.1007/s10974-016-9443-7

Kabsch, W., Mannherz, H. G., Suck, D., Pai, E. F., & Holmes, K. C. (1990). Atomic structure of the actin:DNase I complex. *Nature*, *347*(6288), 37–44. https://doi.org/10.1038/347037a0

Kabsch, W., & Vandekerckhove, J. (1992). Structure and function of actin. *Annual Review of Biophysics and Biomolecular Structure*, *21*, 49–76. https://doi.org/10.1146/annurev.bb.21.060192.000405

Kalyva, A., Schmidtmann, A., & Geeves, M. A. (2012). In vitro formation and characterization of the skeletal muscle α·β tropomyosin heterodimers. *Biochemistry*, *51*(32), 6388–6399. https://doi.org/10.1021/bi300340r

Kirwan, J. P., & Hodges, R. S. (2010). Critical interactions in the stability control region of tropomyosin. *Journal of Structural Biology*, *170*(2), 294–306. https://doi.org/10.1016/j.jsb.2010.01.020

Knight, P., & Trinick, J. (1984). Structure of the myosin projections on native thick filaments from vertebrate skeletal muscle. *Journal of Molecular Biology*, *177*(3), 461–482. https://doi.org/10.1016/0022-2836(84)90295-x

Kopylova, G. V., Matyushenko, A. M., Koubassova, N. A., Shchepkin, D. V., Bershitsky, S. Y., Levitsky, D. I., & Tsaturyan, A. K. (2020). Functional outcomes of structural peculiarities of striated muscle tropomyosin. *Journal of Muscle Research and Cell Motility*, *41*(1), 55–70. https://doi.org/10.1007/s10974-019-09552-8

Kostyukova, A., Maeda, K., Yamauchi, E., Krieger, I., & Maéda, Y. (2000). Domain structure of tropomodulin: Distinct properties of the N-terminal and C-terminal halves. *European Journal of Biochemistry*, *267*(21), 6470–6475. https://doi.org/10.1046/j.1432-1327.2000.01738.x

Kostyukova, A. S., & Hitchcock-DeGregori, S. E. (2004). Effect of the structure of the N terminus of tropomyosin on tropomodulin function. *The Journal of Biological Chemistry*, *279*(7), 5066–5071. https://doi.org/10.1074/jbc.M311186200

Kouyama, T., & Mihashi, K. (1981). Fluorimetry study of N-(1-pyrenyl)iodoacetamide-labelled F-actin. Local structural change of actin protomer both on polymerization and on binding of heavy meromyosin. *European Journal of Biochemistry*, *114*(1), 33–38.

Kowalczyk, B., & Feluś, J. (2016). Arthrogryposis: An update on clinical aspects, etiology, and treatment strategies. *Archives of Medical Science: AMS*, *12*(1), 10–24. https://doi.org/10.5114/aoms.2016.57578

Kremneva, E., Makkonen, M. H., Skwarek-Maruszewska, A., Gateva, G., Michelot, A., Dominguez, R., & Lappalainen, P. (2014). Cofilin-2 controls actin filament length in muscle sarcomeres. *Developmental Cell*, *31*(2), 215–226. https://doi.org/10.1016/j.devcel.2014.09.002

Laemmli, U. K. (1970). Cleavage of structural proteins during the assembly of the head of bacteriophage T4. *Nature*, *227*(5259), 680–685. https://doi.org/10.1038/227680a0

Lambert, M. R., & Gussoni, E. (2023). Tropomyosin 3 (TPM3) function in skeletal muscle and in myopathy. *Skeletal Muscle*, *13*(1), 18. https://doi.org/10.1186/s13395-023-00327-x

Lappalainen, P., & Drubin, D. G. (1997). Cofilin promotes rapid actin filament turnover in vivo. *Nature*, *388*(6637), 78–82. https://doi.org/10.1038/40418

Laurent-Winter, C., Soussi-Yanicostas, N., & Butler-Browne, G. S. (1991). Biphasic expression of slow myosin light chains and slow tropomyosin isoforms during the development of the human quadriceps muscle. *FEBS Letters*, *280*(2), 292–296. https://doi.org/10.1016/0014-5793(91)80315-t

Lehman, W. (2017). Switching Muscles On and Off in Steps: The McKillop-Geeves Three-State Model of Muscle Regulation. *Biophysical Journal*, *112*(12), 2459–2466. https://doi.org/10.1016/j.bpj.2017.04.053

Lehman, W. (2026). The Structural Role of Tropomyosin in Regulating Thin Filament Activation of Actin-Myosin Interaction. *Sub-Cellular Biochemistry*, *113*, 59–80. https://doi.org/10.1007/978-3-032-05273-5_3

Lehman, W., Hatch, V., Korman, V., Rosol, M., Thomas, L., Maytum, R., Geeves, M. A., Van Eyk, J. E., Tobacman, L. S., & Craig, R. (2000). Tropomyosin and actin isoforms modulate the localization of tropomyosin strands on actin filaments1. *Journal of Molecular Biology*, *302*(3), 593–606. https://doi.org/10.1006/jmbi.2000.4080

Lehman, W., Rynkiewicz, M. J., & Moore, J. R. (2020). A New Twist on Tropomyosin Binding to Actin Filaments: Perspectives on Thin Filament Function, Assembly and Biomechanics. *Journal of Muscle Research and Cell Motility*, *41*(1), 23–38. https://doi.org/10.1007/s10974-019-09501-5

Lehrer, S. S., Ly, S., & Fuchs, F. (2011). Tropomyosin is in a reduced state in rat cardiac muscle. *Journal of Muscle Research and Cell Motility*, *32*(2), 63–64. https://doi.org/10.1007/s10974-011-9254-9

Lehrer, S. S., & Morris, E. P. (1982). Dual effects of tropomyosin and troponin-tropomyosin on actomyosin subfragment 1 ATPase. *Journal of Biological Chemistry*, *257*(14), 8073–8080. https://doi.org/10.1016/S0021-9258(18)34298-4

Li, P., Kelley, B., Li, Z., Proctor, B., Corrion, A., Xie, X., Sheick, R., Lu, Y., Nomoto, M., Wei, C., Tada, Y., He, S.-Y., Xiao, S., & Day, B. (2025). Actin Depolymerization Factor (ADF) Moonlighting: Nuclear Immune Regulation by Interacting with WRKY Transcription Factors and Shaping the Transcriptome. *bioRxiv*, 2025.04.29.651294. https://doi.org/10.1101/2025.04.29.651294

Li, X., Tobacman, L. S., Mun, J. Y., Craig, R., Fischer, S., & Lehman, W. (2011). Tropomyosin Position on F-Actin Revealed by EM Reconstruction and Computational

Chemistry. *Biophysical Journal*, *100*(4), 1005–1013. https://doi.org/10.1016/j.bpj.2010.12.3697

Lionne, C., Brune, M., Webb, M. R., Travers, F., & Barman, T. (1995). Time resolved measurements show that phosphate release is the rate limiting step on myofibrillar ATPases. *FEBS Letters*, *364*(1), 59–62. https://doi.org/10.1016/0014-5793(95)00356-e

Littlefield, R. S., & Fowler, V. M. (2008). Thin filament length regulation in striated muscle sarcomeres: Pointed-end dynamics go beyond a nebulin ruler. *Seminars in Cell & Developmental Biology*, *19*(6), 511–519. https://doi.org/10.1016/j.semcdb.2008.08.009

MacIntosh, B. R. (with Internet Archive). (2006). *Skeletal muscle: Form and function*. Champaign, IL : Human Kinetics. http://archive.org/details/skeletalmusclefo0000maci

Margossian, S. S., & Lowey, S. (1982). Preparation of myosin and its subfragments from rabbit skeletal muscle. *Methods in Enzymology*, *85 Pt B*, 55–71. https://doi.org/10.1016/0076-6879(82)85009-x

Marshall, W. F. (2004). Cellular length control systems. *Annual Review of Cell and Developmental Biology*, *20*, 677–693. https://doi.org/10.1146/annurev.cellbio.20.012103.094437

Marston, S., Memo, M., Messer, A., Papadaki, M., Nowak, K., McNamara, E., Ong, R., El-Mezgueldi, M., Li, X., & Lehman, W. (2013). Mutations in repeating structural motifs of tropomyosin cause gain of function in skeletal muscle myopathy patients. *Human Molecular Genetics*, *22*(24), 4978–4987. https://doi.org/10.1093/hmg/ddt345

Marttila, M., Lehtokari, V.-L., Marston, S., Nyman, T. A., Barnerias, C., Beggs, A. H., Bertini, E., Ceyhan-Birsoy, Ö., Cintas, P., Gerard, M., Gilbert-Dussardier, B., Hogue, J. S., Longman, C., Eymard, B., Frydman, M., Kang, P. B., Klinge, L., Kolski, H., Lochmüller, H., … Wallgren-Pettersson, C. (2014). Mutation Update and Genotype–Phenotype Correlations of Novel and Previously Described Mutations in TPM2 and TPM3 Causing Congenital Myopathies. *Human Mutation*, *35*(7), 779–790. https://doi.org/10.1002/humu.22554

Marttila, M., Lemola, E., Wallefeld, W., Memo, M., Donner, K., Laing, N. G., Marston, S., Grönholm, M., & Wallgren-Pettersson, C. (2012). Abnormal actin binding of aberrant β-tropomyosins is a molecular cause of muscle weakness in TPM2-related nemaline and cap myopathy. *Biochemical Journal*, *442*(1), 231–239.

Matyushenko, A. M., Kleymenov, S. Y., Susorov, D. S., & Levitsky, D. I. (2018). Thermal unfolding of homodimers and heterodimers of different skeletal-muscle isoforms of tropomyosin. *Biophysical Chemistry*, *243*, 1–7. https://doi.org/10.1016/j.bpc.2018.09.002

McAdow, J., Yang, S., Ou, T., Huang, G., Dobbs, M. B., Gurnett, C. A., Greenberg, M. J., & Johnson, A. N. (2022). A pathogenic mechanism associated with myopathies and structural birth defects involves TPM2-directed myogenesis. *JCI Insight*, *7*(12), e152466. https://doi.org/10.1172/jci.insight.152466

McCullough, B. R., Grintsevich, E. E., Chen, C. K., Kang, H., Hutchison, A. L., Henn, A., Cao, W., Suarez, C., Martiel, J.-L., Blanchoin, L., Reisler, E., & De La Cruz, E. M. (2011). Cofilin-linked changes in actin filament flexibility promote severing. *Biophysical Journal*, *101*(1), 151–159. https://doi.org/10.1016/j.bpj.2011.05.049

McGough, A., Pope, B., Chiu, W., & Weeds, A. (1997). Cofilin changes the twist of F-actin: Implications for actin filament dynamics and cellular function. *The Journal of Cell Biology*, *138*(4), 771–781. https://doi.org/10.1083/jcb.138.4.771

McKillop, D. F., & Geeves, M. A. (1993). Regulation of the interaction between actin and myosin subfragment 1: Evidence for three states of the thin filament. *Biophysical Journal*, *65*(2), 693–701. https://doi.org/10.1016/S0006-3495(93)81110-X

McLachlan, A. D., & Stewart, M. (1976). The 14-fold periodicity in alpha-tropomyosin and the interaction with actin. *Journal of Molecular Biology*, *103*(2), 271–298. https://doi.org/10.1016/0022-2836(76)90313-2

Meng, E. C., Goddard, T. D., Pettersen, E. F., Couch, G. S., Pearson, Z. J., Morris, J. H., & Ferrin, T. E. (2023). UCSF ChimeraX: Tools for structure building and analysis. *Protein Science*, *32*(11), e4792. https://doi.org/10.1002/pro.4792

Merino, F., Pospich, S., Funk, J., Wagner, T., Küllmer, F., Arndt, H.-D., Bieling, P., & Raunser, S. (2018). Structural transitions of F-actin upon ATP hydrolysis at near-atomic resolution revealed by cryo-EM. *Nature Structural & Molecular Biology*, *25*(6), 528–537. https://doi.org/10.1038/s41594-018-0074-0

Merino, F., Pospich, S., & Raunser, S. (2020). Towards a structural understanding of the remodeling of the actin cytoskeleton. *Seminars in Cell & Developmental Biology*, *102*, 51–64. https://doi.org/10.1016/j.semcdb.2019.11.018

Michele, D. E., & Metzger, J. M. (2000). Physiological consequences of tropomyosin mutations associated with cardiac and skeletal myopathies. *Journal of Molecular Medicine*, *78*(10), 543–553. https://doi.org/10.1007/s001090000161

Millane, R. P., & Luther, P. K. (2023). The vertebrate muscle superlattice: Discovery, consequences, and link to geometric frustration. *Journal of Muscle Research and Cell Motility*, *44*(3), 153–163. https://doi.org/10.1007/s10974-023-09642-8

Monteiro, P. B., Lataro, R. C., Ferro, J. A., & Reinach, F. de C. (1994). Functional alpha-tropomyosin produced in Escherichia coli. A dipeptide extension can substitute the amino-terminal acetyl group. *The Journal of Biological Chemistry*, *269*(14), 10461–10466.

Moore, J. R., Campbell, S. G., & Lehman, W. (2016). Structural determinants of muscle thin filament cooperativity. *Archives of Biochemistry and Biophysics*, *594*, 8–17. https://doi.org/10.1016/j.abb.2016.02.016

Moraczewska, J. (2002). Structural determinants of cooperativity in acto-myosin interactions. *Acta Biochimica Polonica*, *49*(4), 805–812.

Moraczewska, J. (2020). Thin filament dysfunctions caused by mutations in tropomyosin Tpm3.12 and Tpm1.1. *Journal of Muscle Research and Cell Motility*, *41*(1), 39–53. https://doi.org/10.1007/s10974-019-09532-y

Moraczewska, J., Gruszczynska-Biegala, J., Redowicz, M. J., Khaitlina, S. Y., & Strzelecka-Golaszewska, H. (2004). The DNase-I binding loop of actin may play a role in the regulation of actin-myosin interaction by tropomyosin/troponin. *The Journal of Biological Chemistry*, *279*(30), 31197–31204. https://doi.org/10.1074/jbc.M400794200

Moraczewska, J., Nicholson-Flynn, K., & Hitchcock-DeGregori, S. E. (1999). The ends of tropomyosin are major determinants of actin affinity and myosin subfragment 1-

induced binding to F-actin in the open state. *Biochemistry*, *38*(48), 15885–15892. https://doi.org/10.1021/bi991816j

Moraczewska, J., Robaszkiewicz, K., Śliwinska, M., Czajkowska, M., Ly, T., Kostyukova, A., Wen, H., & Zheng, W. (2019). Congenital myopathy-related mutations in tropomyosin disrupt regulatory function through altered actin affinity and tropomodulin binding. *The FEBS Journal*, *286*(10), 1877–1893. https://doi.org/10.1111/febs.14787

Moraczewska, J., Sliwińska, M., & Redowicz, M. J. (2012). [Calcium ions in the regulation of acto-myosin interactions]. *Postepy Biochemii*, *58*(4), 437–451.

Moraczewska, J., Wawro, B., Seguro, K., & Strzelecka-Golaszewska, H. (1999). Divalent cation-, nucleotide-, and polymerization-dependent changes in the conformation of subdomain 2 of actin. *Biophysical Journal*, *77*(1), 373–385. https://doi.org/10.1016/S0006-3495(99)76896-7

Moroz, N. A., Novak, S. M., Azevedo, R., Colpan, M., Uversky, V. N., Gregorio, C. C., & Kostyukova, A. S. (2013). Alteration of tropomyosin-binding properties of tropomodulin-1 affects its capping ability and localization in skeletal myocytes. *The Journal of Biological Chemistry*, *288*(7), 4899–4907. https://doi.org/10.1074/jbc.M112.434522

Murakami, K., Yasunaga, T., Noguchi, T. Q. P., Gomibuchi, Y., Ngo, K. X., Uyeda, T. Q. P., & Wakabayashi, T. (2010). Structural Basis for Actin Assembly, Activation of ATP Hydrolysis, and Delayed Phosphate Release. *Cell*, *143*(2), 275–287. https://doi.org/10.1016/j.cell.2010.09.034

Muscle Types | SEER Training. (n.d.). Retrieved August 4, 2026, from https://training.seer.cancer.gov/anatomy/muscular/types.html

Muthu, P., Talent, J. M., Gryczynski, I., & Borejdo, J. (2008). Cross-bridge duty cycle in isometric contraction of skeletal myofibrils. *Biochemistry*, *47*(20), 5657–5667. https://doi.org/10.1021/bi7023223

Ngo, K. X., Umeki, N., Kijima, S. T., Kodera, N., Ueno, H., Furutani-Umezu, N., Nakajima, J., Noguchi, T. Q. P., Nagasaki, A., Tokuraku, K., & Uyeda, T. Q. P. (2016). Allosteric regulation by cooperative conformational changes of actin filaments drives mutually exclusive binding with cofilin and myosin. *Scientific Reports*, *6*(1), 35449. https://doi.org/10.1038/srep35449

Ochala, J., Gokhin, D. S., Pénisson-Besnier, I., Quijano-Roy, S., Monnier, N., Lunardi, J., Romero, N. B., & Fowler, V. M. (2012). Congenital myopathy-causing tropomyosin mutations induce thin filament dysfunction via distinct physiological mechanisms. *Human Molecular Genetics*, *21*(20), 4473–4485. https://doi.org/10.1093/hmg/dds289

Ochala, J., Li, M., Ohlsson, M., Oldfors, A., & Larsson, L. (2008). Defective regulation of contractile function in muscle fibres carrying an E41K beta-tropomyosin mutation. *The Journal of Physiology*, *586*(12), 2993–3004. https://doi.org/10.1113/jphysiol.2008.153650

Oda, T., Iwasa, M., Aihara, T., Maéda, Y., & Narita, A. (2009). The nature of the globular- to fibrous-actin transition. *Nature*, *457*(7228), 441–445. https://doi.org/10.1038/nature07685

Offer, G., & Knight, P. (1996). The structure of the head-tail junction of the myosin molecule. *Journal of Molecular Biology*, *256*(3), 407–416. https://doi.org/10.1006/jmbi.1996.0096

Ohlsson, M., Quijano-Roy, S., Darin, N., Brochier, G., Lacène, E., Avila-Smirnow, D., Fardeau, M., Oldfors, A., & Tajsharghi, H. (2008). New morphologic and genetic findings in cap disease associated with beta-tropomyosin (TPM2) mutations. *Neurology*, *71*(23), 1896–1901. https://doi.org/10.1212/01.wnl.0000336654.44814.b8

Ono, S. (2010). Dynamic regulation of sarcomeric actin filaments in striated muscle. *Cytoskeleton*, *67*(11), 677–692. https://doi.org/10.1002/cm.20476

Ono, S., & Ono, K. (2002). Tropomyosin inhibits ADF/cofilin-dependent actin filament dynamics. *The Journal of Cell Biology*, *156*(6), 1065–1076. https://doi.org/10.1083/jcb.200110013

Oosterheert, W., Boiero Sanders, M., Hofnagel, O., Bieling, P., & Raunser, S. (2025). Choreography of rapid actin filament disassembly by coronin, cofilin, and AIP1. *Cell*, *188*(24), 6845-6860.e27. https://doi.org/10.1016/j.cell.2025.09.016

Orzechowski, M., Fischer, S., Moore, J. R., Lehman, W., & Farman, G. P. (2014). Energy landscapes reveal the myopathic effects of tropomyosin mutations. *Archives of Biochemistry and Biophysics*, *564*, 89–99. https://doi.org/10.1016/j.abb.2014.09.007

Palmer, N. J., Boczkowska, M., Rebowski, G., & Dominguez, R. (2026). Mechanisms of disassembly at the actin filament pointed and barbed ends. *Science Advances*, *12*(14), eaee5882. https://doi.org/10.1126/sciadv.aee5882

Papadimas, G. K., Xirou, S., Kararizou, E., & Papadopoulos, C. (2020). Update on Congenital Myopathies in Adulthood. *International Journal of Molecular Sciences*, *21*(10), 3694. https://doi.org/10.3390/ijms21103694

Pardee, J. D., & Spudich, J. A. (1982). Purification of muscle actin. *Methods in Enzymology*, *85 Pt B*, 164–181. https://doi.org/10.1016/0076-6879(82)85020-9

Park, Y. H., Song, G. S., & Jung, H. S. (2024). Research reviews on myosin head interactions with F-actin. *Applied Microscopy*, *54*(1), 6. https://doi.org/10.1186/s42649-024-00099-8

Parry, D. A. D., & Squire, J. M. (Eds.). (2017). *Fibrous Proteins: Structures and Mechanisms* (Vol. 82). Springer International Publishing. https://doi.org/10.1007/978-3-319-49674-0

Paxton, S., Peckham, M., & Knibbs, A. (2003). *The Leeds Histology Guide*. https://www.histology.leeds.ac.uk/tissue_types/muscle/Three_muscle_types.php

Perry, S. V. (2001). Vertebrate tropomyosin: Distribution, properties and function. *Journal of Muscle Research and Cell Motility*, *22*(1), 5–49. https://doi.org/10.1023/a:1010303732441

Phillips, G. N. (1986). Construction of an atomic model for tropomyosin and implications for interactions with actin. *Journal of Molecular Biology*, *192*(1), 128–131. https://doi.org/10.1016/0022-2836(86)90469-9

Pieples, K., & Wieczorek, D. F. (2000). Tropomyosin 3 Increases Striated Muscle Isoform Diversity. *Biochemistry*, *39*(28), 8291–8297. https://doi.org/10.1021/bi000047x

Pollard, T. D. (2016). Actin and Actin-Binding Proteins. *Cold Spring Harbor Perspectives in Biology*, *8*(8), a018226. https://doi.org/10.1101/cshperspect.a018226

Potter, J. D. (1982). Preparation of troponin and its subunits. *Methods in Enzymology, 85 Pt B*, 241–263. https://doi.org/10.1016/0076-6879(82)85024-6

Quijano-Roy, S., Avila-Smirnow, D., Carlier, R. Y., & WB-MRI muscle study group. (2012). Whole body muscle MRI protocol: Pattern recognition in early onset NM disorders. *Neuromuscular Disorders: NMD, 22 Suppl 2*, S68-84. https://doi.org/10.1016/j.nmd.2012.08.003

Rao, J. N., Madasu, Y., & Dominguez, R. (2014). Mechanism of actin filament pointed-end capping by tropomodulin. *Science, 345*(6195), 463–467. https://doi.org/10.1126/science.1256159

Rassier, D. E., & Månsson, A. (2025). Mechanisms of myosin II force generation: Insights from novel experimental techniques and approaches. *Physiological Reviews*, *105*(1), 1–93. https://doi.org/10.1152/physrev.00014.2023

Ravenscroft, G., Bryson-Richardson, R. J., Nowak, K. J., & Laing, N. G. (2018). Recent advances in understanding congenital myopathies. *F1000Research, 7*, F1000 Faculty Rev-1921. https://doi.org/10.12688/f1000research.16422.1

Ravenscroft, G., Laing, N. G., & Bönnemann, C. G. (2015). Pathophysiological concepts in the congenital myopathies: Blurring the boundaries, sharpening the focus. *Brain: A Journal of Neurology, 138*(Pt 2), 246–268. https://doi.org/10.1093/brain/awu368

Rayment, I., Rypniewski, W. R., Schmidt-Bäse, K., Smith, R., Tomchick, D. R., Benning, M. M., Winkelmann, D. A., Wesenberg, G., & Holden, H. M. (1993). Three-dimensional structure of myosin subfragment-1: A molecular motor. *Science, 261*(5117), 50–58. https://doi.org/10.1126/science.8316857

Redwood, C., & Robinson, P. (2013). Alpha-tropomyosin mutations in inherited cardiomyopathies. *Journal of Muscle Research and Cell Motility, 34*(3–4), 285–294. https://doi.org/10.1007/s10974-013-9358-5

Risi, C. M., Landim-Vieira, M., Belknap, B., Chase, P. B., Pinto, J. R., & Galkin, V. E. (2025). The role of the troponin T interactions with actin in regulation of cardiac thin filament revealed by the troponin T pathogenic variant Ile79Asn. *Journal of Molecular and Cellular Cardiology*, *204*, 55–67. https://doi.org/10.1016/j.yjmcc.2025.05.005

Risi, C. M., Pepper, I., Belknap, B., Landim-Vieira, M., White, H. D., Dryden, K., Pinto, J. R., Chase, P. B., & Galkin, V. E. (2021). The structure of the native cardiac thin filament at systolic Ca2+ levels. *Proceedings of the National Academy of Sciences, 118*(13), e2024288118. https://doi.org/10.1073/pnas.2024288118

Robaszkiewicz, K., Ostrowska, Z., Cyranka-Czaja, A., & Moraczewska, J. (2015). Impaired tropomyosin-troponin interactions reduce activation of the actin thin filament. *Biochimica Et Biophysica Acta*, *1854*(5), 381–390. https://doi.org/10.1016/j.bbapap.2015.01.004

Robaszkiewicz, K., Ostrowska, Z., Marchlewicz, K., & Moraczewska, J. (2016). Tropomyosin isoforms differentially modulate the regulation of actin filament polymerization and depolymerization by cofilins. *The FEBS Journal*, *283*(4), 723–737. https://doi.org/10.1111/febs.13626

Robaszkiewicz, K., Śliwinska, M., & Moraczewska, J. (2020). Regulation of Actin Filament Length by Muscle Isoforms of Tropomyosin and Cofilin. *International Journal of Molecular Sciences, 21*(12), 4285. https://doi.org/10.3390/ijms21124285

Robaszkiewicz, K., Wróbel, J., & Moraczewska, J. (2023). Troponin and a Myopathy-Linked Mutation in TPM3 Inhibit Cofilin-2-Induced Thin Filament Depolymerization. *International Journal of Molecular Sciences*, *24*(22), 16457. https://doi.org/10.3390/ijms242216457

Robinson, P., Lipscomb, S., Preston, L. C., Altin, E., Watkins, H., Ashley, C. C., & Redwood, C. S. (2007). Mutations in fast skeletal troponin I, troponin T, and beta-tropomyosin that cause distal arthrogryposis all increase contractile function. *FASEB Journal: Official Publication of the Federation of American Societies for Experimental Biology*, *21*(3), 896–905. https://doi.org/10.1096/fj.06-6899com

Rynkiewicz, M. J., Childers, M. C., Karpicheva, O. E., Regnier, M., Geeves, M. A., & Lehman, W. (2024). Myosin's powerstroke transitions define atomic scale movement of cardiac thin filament tropomyosin. *The Journal of General Physiology*, *156*(5), e202413538. https://doi.org/10.1085/jgp.202413538

Rynkiewicz, M. J., Pavadai, E., & Lehman, W. (2022). Modeling Human Cardiac Thin Filament Structures. *Frontiers in Physiology*, *13*. https://doi.org/10.3389/fphys.2022.932333

Schafer, D. A., Hug, C., & Cooper, J. A. (1995). Inhibition of CapZ during myofibrillogenesis alters assembly of actin filaments. *The Journal of Cell Biology*, *128*(1–2), 61–70. https://doi.org/10.1083/jcb.128.1.61

Schafer, D. A., Waddle, J. A., & Cooper, J. A. (1993). Localization of CapZ during myofibrillogenesis in cultured chicken muscle. *Cell Motility and the Cytoskeleton*, *25*(4), 317–335. https://doi.org/10.1002/cm.970250403

Schultz, L. E., Colpan, M., Smith, G. E., Mayfield, R. M., Larrinaga, T. M., Kostyukova, A. S., & Gregorio, C. C. (n.d.). A nemaline myopathy–linked mutation inhibits the actin-regulatory functions of tropomodulin and leiomodin. *Proceedings of the National Academy of Sciences of the United States of America*, *120*(47), e2315820120. https://doi.org/10.1073/pnas.2315820120

Sewry, C. A., Laitila, J. M., & Wallgren-Pettersson, C. (2019). Nemaline myopathies: A current view. *Journal of Muscle Research and Cell Motility*, *40*(2), 111–126. https://doi.org/10.1007/s10974-019-09519-9

Shekhar, S., Chung, J., Kondev, J., Gelles, J., & Goode, B. L. (2019). Synergy between Cyclase-associated protein and Cofilin accelerates actin filament depolymerization by two orders of magnitude. *Nature Communications*, *10*(1), 5319. https://doi.org/10.1038/s41467-019-13268-1

Sheterline, P., & Sparrow, J. C. (1994). Actin. *Protein Profile*, *1*(1), 1–121.

Śliwinska, M., Robaszkiewicz, K., Wasąg, P., & Moraczewska, J. (2021). Mutations Q93H and E97K in TPM2 Disrupt Ca-Dependent Regulation of Actin Filaments. *International Journal of Molecular Sciences*, *22*(8), 4036. https://doi.org/10.3390/ijms22084036

Spudich, J. A. (2001). The myosin swinging cross-bridge model. *Nature Reviews. Molecular Cell Biology*, *2*(5), 387–392. https://doi.org/10.1038/35073086

Spudich, J. A., & Watt, S. (1971). The regulation of rabbit skeletal muscle contraction. I. Biochemical studies of the interaction of the tropomyosin-troponin complex with actin and the proteolytic fragments of myosin. *The Journal of Biological Chemistry*, *246*(15), 4866–4871.

Stenson, P. D., Mort, M., Ball, E. V., Evans, K., Hayden, M., Heywood, S., Hussain, M., Phillips, A. D., & Cooper, D. N. (2017). The Human Gene Mutation Database: Towards a comprehensive repository of inherited mutation data for medical research, genetic diagnosis and next-generation sequencing studies. *Human Genetics*, *136*(6), 665–677. https://doi.org/10.1007/s00439-017-1779-6

Stewart, M. (2001). Structural basis for bending tropomyosin around actin in muscle thin filaments. *Proceedings of the National Academy of Sciences of the United States of America*, *98*(15), 8165–8166. https://doi.org/10.1073/pnas.151265198

Szikora, S., Görög, P., & Mihály, J. (2022). The Mechanisms of Thin Filament Assembly and Length Regulation in Muscles. *International Journal of Molecular Sciences*, *23*(10), 5306. https://doi.org/10.3390/ijms23105306

Tajsharghi, H., Kimber, E., Holmgren, D., Tulinius, M., & Oldfors, A. (2007). Distal arthrogryposis and muscle weakness associated with a beta-tropomyosin mutation. *Neurology*, *68*(10), 772–775. https://doi.org/10.1212/01.wnl.0000256339.40667.fb

Tajsharghi, H., Ohlsson, M., Lindberg, C., & Oldfors, A. (2007). Congenital myopathy with nemaline rods and cap structures caused by a mutation in the beta-tropomyosin gene (TPM2). *Archives of Neurology*, *64*(9), 1334–1338. https://doi.org/10.1001/archneur.64.9.1334

Tajsharghi, H., Ohlsson, M., Palm, L., & Oldfors, A. (2012). Myopathies associated with β-tropomyosin mutations. *Neuromuscular Disorders*, *22*(11), 923–933. https://doi.org/10.1016/j.nmd.2012.05.018

Tobacman, L. S. (2021). Troponin Revealed: Uncovering the Structure of the Thin Filament On-Off Switch in Striated Muscle. *Biophysical Journal*, *120*(1), 1–9. https://doi.org/10.1016/j.bpj.2020.11.014

Tolkatchev, D., Kuruba, B., Smith, G. E., Swain, K. D., Smith, K. A., Moroz, N., Williams, T. J., & Kostyukova, A. S. (2021). Structural insights into the tropomodulin assembly at the pointed ends of actin filaments. *Protein Science : A Publication of the Protein Society*, *30*(2), 423–437. https://doi.org/10.1002/pro.4000

Trinick, J. (1994). Titin and nebulin: Protein rulers in muscle? *Trends in Biochemical Sciences*, *19*(10), 405–409. https://doi.org/10.1016/0968-0004(94)90088-4

Trivedi, D. V., Adhikari, A. S., Sarkar, S. S., Ruppel, K. M., & Spudich, J. A. (2018). Hypertrophic cardiomyopathy and the myosin mesa: Viewing an old disease in a new light. *Biophysical Reviews*, *10*(1), 27–48. https://doi.org/10.1007/s12551-017-0274-6

Vallotton, P., van Oijen, A. M., Whitchurch, C. B., Gelfand, V., Yeo, L., Tsiavaliaris, G., Heinrich, S., Dultz, E., Weis, K., & Grünwald, D. (2017). Diatrack particle tracking software: Review of applications and performance evaluation. *Traffic*, *18*(12), 840–852. https://doi.org/10.1111/tra.12530

Vera, C., Sood, A., Gao, K.-M., Yee, L. J., Lin, J. J.-C., & Sung, L. A. (2000). Tropomodulin-Binding Site Mapped to Residues 7–14 at the N-Terminal Heptad Repeats of Tropomyosin Isoform 5. *Archives of Biochemistry and Biophysics*, *378*(1), 16–24. https://doi.org/10.1006/abbi.2000.1802

Vibert, P., Craig, R., & Lehman, W. (1997). Steric-model for activation of muscle thin filaments. *Journal of Molecular Biology*, *266*(1), 8–14. https://doi.org/10.1006/jmbi.1996.0800

Vinogradova, M. V., Stone, D. B., Malanina, G. G., Karatzaferi, C., Cooke, R., Mendelson, R. A., & Fletterick, R. J. (2005). Ca(2+)-regulated structural changes in troponin. *Proceedings of the National Academy of Sciences of the United States of America*, *102*(14), 5038–5043. https://doi.org/10.1073/pnas.0408882102

Vogt, J., Al-Saedi, A., Willis, T., Male, A., McKie, A., Kiely, N., & Maher, E. R. (2020). A recurrent pathogenic variant in TPM2 reveals further phenotypic and genetic heterogeneity in multiple pterygium syndrome-related disorders. *Clinical Genetics*, *97*(6), 908–914. https://doi.org/10.1111/cge.13728

von der Ecken, J., Müller, M., Lehman, W., Manstein, D. J., Penczek, P. A., & Raunser, S. (2015). Structure of the F-actin-tropomyosin complex. *Nature*, *519*(7541), 114–117. https://doi.org/10.1038/nature14033

Wang, K., & Wright, J. (1988). Architecture of the sarcomere matrix of skeletal muscle: Immunoelectron microscopic evidence that suggests a set of parallel inextensible nebulin filaments anchored at the Z line. *The Journal of Cell Biology*, *107*(6 Pt 1), 2199–2212. https://doi.org/10.1083/jcb.107.6.2199

Wang, Z., Grange, M., Wagner, T., Kho, A. L., Gautel, M., & Raunser, S. (2021). The molecular basis for sarcomere organization in vertebrate skeletal muscle. *Cell*, *184*(8), 2135-2150.e13. https://doi.org/10.1016/j.cell.2021.02.047

Wang, Z., & Raunser, S. (2023). Structural Biochemistry of Muscle Contraction. *Annual Review of Biochemistry*, *92*(Volume 92, 2023), 411–433. https://doi.org/10.1146/annurev-biochem-052521-042909

Warrick, H. M., & Spudich, J. A. (1987). Myosin structure and function in cell motility. *Annual Review of Cell Biology*, *3*, 379–421. https://doi.org/10.1146/annurev.cb.03.110187.002115

Weber, A., Pennise, C. R., Babcock, G. G., & Fowler, V. M. (1994). Tropomodulin caps the pointed ends of actin filaments. *The Journal of Cell Biology*, *127*(6 Pt 1), 1627–1635. https://doi.org/10.1083/jcb.127.6.1627

Whittle, J., Johnson, A., Dobbs, M. B., & Gurnett, C. A. (2021). Models of Distal Arthrogryposis and Lethal Congenital Contracture Syndrome. *Genes*, *12*(6), 943. https://doi.org/10.3390/genes12060943

Wioland, H., Guichard, B., Senju, Y., Myram, S., Lappalainen, P., Jégou, A., & Romet-Lemonne, G. (2017). ADF/Cofilin Accelerates Actin Dynamics by Severing Filaments and Promoting Their Depolymerization at Both Ends. *Current Biology: CB*, *27*(13), 1956-1967.e7. https://doi.org/10.1016/j.cub.2017.05.048

Yamada, Y., Namba, K., & Fujii, T. (2020). Cardiac muscle thin filament structures reveal calcium regulatory mechanism. *Nature Communications*, *11*(1), 153. https://doi.org/10.1038/s41467-019-14008-1

Yamashiro, S., Gokhin, D. S., Sui, Z., Bergeron, S. E., Rubenstein, P. A., & Fowler, V. M. (2014). Differential Actin-regulatory Activities of Tropomodulin1 and Tropomodulin3 with Diverse Tropomyosin and Actin Isoforms *. *Journal of Biological Chemistry*, *289*(17), 11616–11629. https://doi.org/10.1074/jbc.M114.555128

Yamashita, A., Maeda, K., & Maéda, Y. (2003). Crystal structure of CapZ: Structural basis for actin filament barbed end capping. *The EMBO Journal*, *22*(7), 1529–1538. https://doi.org/10.1093/emboj/cdg167

Yang, S., Barbu-Tudoran, L., Orzechowski, M., Craig, R., Trinick, J., White, H., & Lehman, W. (2014). Three-dimensional organization of troponin on cardiac muscle thin filaments in the relaxed state. *Biophysical Journal*, *106*(4), 855–864. https://doi.org/10.1016/j.bpj.2014.01.007

Zeng, W., Conibear, P. B., Dickens, J. L., Cowie, R. A., Wakelin, S., Málnási-Csizmadia, A., & Bagshaw, C. R. (2004). Dynamics of actomyosin interactions in relation to the cross-bridge cycle. *Philosophical Transactions of the Royal Society of London. Series B, Biological Sciences*, *359*(1452), 1843–1855. https://doi.org/10.1098/rstb.2004.1527

Zhang, H., Chang, M., Chen, D., Yang, J., Zhang, Y., Sun, J., Yao, X., Sun, H., Gu, X., Li, M., Shen, Y., & Dai, B. (2024). Congenital myopathies: Pathophysiological mechanisms and promising therapies. *Journal of Translational Medicine*, *22*(1), 815. https://doi.org/10.1186/s12967-024-05626-5

Zhao, J., Du, X., Fang, W., Zhu, H., & Yue, B. (2025). Architecture and molecular machinery of skeletal myofibers: A systematic review of the structure–function relationships. *Frontiers in Cell and Developmental Biology*, *13*. https://doi.org/10.3389/fcell.2025.1602607

Zhu, C., Chen, Z., & Guo, W. (2017). Pre-mRNA mis-splicing of sarcomeric genes in heart failure. *Biochimica Et Biophysica Acta. Molecular Basis of Disease*, *1863*(8), 2056–2063. https://doi.org/10.1016/j.bbadis.2016.11.008

List of Figures

List of Tables